ENGINYERIA ELECTRÒNICA ELÈCTRICA I AUTOMÀTICA

UNIVERSITAT ROVIRA I VIRGILI

Graduate Students Meeting on Electronics Engineering

Tarragona, June 27th and 28th, 2024

BOOK OF ABSTRACTS

Index 3

Program. 7

Keynote Presentations Abstracts 9

Students Proceedings 11

Students Talks

Deepanshu Verma
Porous alumina-based biosensing platforms for early-stage infection diagnosis 13

Camilla Guerrrini
Advanced formula-oriented suspect screening workflow to unravel the early-life chemical exposome in silicone wristbands 15

Students Contributions

Mohamed Ayoub Alouani
The effect of the substrate on the sensing properties of graphene and MnO_2 loaded graphene 19

Alejandro Santos-Betancourt
IoT and ANN Integration for Air Pollution Monitoring 23

Anisleidy Broche
Study of the Transport Mechanism in MoS_2 FETs, Using Modeling and Simulation of a Fabricated Device 25

José Carlos Santos-Ceballos
Electrochemical Polyaniline Deposition on Laser-Induced Graphene Sensor for Ammonia Detection at Room Temperature 27

Alexandra Blanch-Fortuna
Discrete-Time Control of a Bidirectional AC-DC Buck-Boost Converter with Input Filter 29

Zohre Hamzei
PANI and Au-PANI dip coated films for electro-optical gas sensors 31

Amer Zaibi
Improved Physics-Based Model for Organic Thin Film Transistors: Accurate Modelling and Parameter Extraction Method 33

Dante Ángel Gómez Nápoles
Algorithm for the Automatization of the Parameter Extraction Method by Mathematical Optimization 37

Tabish Aftab
Enhanced Pseudocapacitive Behaviour of Porous Anodic Alumina Templated Ni-Nanorod Electrodes 39

Jyayasi Sharma
UV-light assisted hybrid InSe-Graphene gas sensor for the detection of NO_2 41

Laia Marín Moncusí
Synthesis and study of a sulphur by selenium substitution in a high voltage photosensitizer for Dye-Sensitized Solar Cells 43

Joan Marc Bondia Pedra
Enhancing electrocatalytic CO_2 reduction through maximization of electroactive sites in a Cobalt phthalocyanine-based polymer 45

Ermias T. Teka
TCAD modeling of Organic Electrochemical Transistors 49

Miguel Antonio Pisani Orta
Review of state of charge estimation methods for battery cells in electric vehicles 51

Josep Maria Cantons
Reflectometric interferometry biosensor based on nanoporous anodic alumina for hGH detection 53

Beatriu Domingo Tafalla
Carbon dots as photoactive platforms for the photocatalytic reduction of CO_2 55

Georgios Papathanidis
Perovskite Nanocrystals for the Fabrication of Light Emitting Diodes 57

Ubaid Ahmad
Two-Phase LLC Converter with Common LC Branch for Inherent Current-Sharing and Phase-Shedding Ability 59

Aladine Fdhila
Synthesis of SnS_2 nanosheets via CVD methods for ppb-level NO_2 detection 61

Nadine Dersch
Simulation of Bimodally Distributed Stochastic Weight in Pulse-Programmed Memristive Crossbar Arrays 63

El Nouha Mammeri
Modeling and Control of a Three-Phase Interleaved Buck Converter as a Battery Charger 65

Jordi Rofes
Exploring multi-omics interactions: microbiota, metabolites, and host responses in a lifestyle intervention model 69

Josep Maria Badia
Spectral Annotation Robustness in Metabolomics: Addressing Variations in Acquisition Conditions 71

ENGINYERIA ELECTRÒNICA ELÈCTRICA I AUTOMÀTICA

UNIVERSITAT ROVIRA I VIRGILI

Graduate Students Meeting on Electronics Engineering

Tarragona June 27th and 28th, 2024

Program

Thursday, June 27th:

Sala de Graus ETSE

15.15 - Opening

15.30 – Keynote: **Anais González Iglesias** (AWS Health, Barcelona)

"Decoding Healthcare with AWS: A Data Science Odyssey"

16.30 – Keynote: **Merlyne de Souza** (Sheffield University, UK)

"Reservoir Computing based on a Solid Electrolyte ZnO TFT: An attractive platform for flexible edge computing"

17.30 - Refreshment and Poster Session

Friday, June 28th:

Sala de Graus ETSE

9.30 - Keynote: **Anton Ficai** (University POLYTECHNIKA Bucharest, Romania)

"Silica, a versatile material for current and emerging applications"

10.30 – Coffee Break and Poster Session

11:00 - MDPI Open Access – An Author Training Program

- **Rocksy Zhang**: Introduction to MDPI

- **Vesna Marinkovic**: Open Access and Publication Ethics

12:30 - Student Talks

Camilla Guerrini

"Advanced formula-oriented suspect screening workflow to unravel the early-life chemical exposome in silicone wristbands"

Trisha Arora

"A Comparison of Machine Learning-Based Collision Cross-Section Prediction Models for Small Molecules"

Deepanshu Verma

"Porous alumina-based biosensing platforms for early-stage infection diagnosis"

13.15 – Closing and Lunch

Invited Contributions
Keynote Speakers

Anais González Iglesias

AWS Health, Barcelona, Spain

Decoding Healthcare with AWS: A Data Science Odyssey

Unlock the frontiers of healthcare data science by embarking on an odyssey powered by AWS. As aspiring researchers and future leaders, you'll explore how cloud computing catalyzes genomic analysis, electronic health record mining, and real-world evidence studies. Discover the cutting-edge applications of AWS in precision medicine, drug development, and personalized care. This odyssey equips you with the tools to harness the vast potential of data, empowering you to drive innovation and transform healthcare through advanced analytics and data-driven insights.

ENGINYERIA ELECTRÒNICA ELÈCTRICA I AUTOMÀTICA

UNIVERSITAT ROVIRA I VIRGILI

Graduate Students Meeting on Electronics Engineering

Students Proceedings

Porous alumina-based biosensing platforms for early-stage infection diagnosis

Deepanshu Verma[1], Hedieh Haji-Hashemi[1], Beatriz Prieto-Simón*[1,2]

1 Institute of Chemical Research in Catalonia (ICIQ), Av. Països Catalans 16, 43007, Tarragona, Spain.

2 ICREA, Pg. Lluís Companys 23, 08010, Barcelona, Spain.

** Correspondence: bprieto@iciq.es*

To overcome the limitations of traditional diagnostic methods like PCR and ELISA, which require expensive and complex equipment[1], we developed innovative biosensing platforms using porous anodic alumina (pAAO) on carbon screen-printed electrodes (CSPEs). These platforms are tailored for the sensitive, specific, and cost-effective detection of exosomes and miRNAs, crucial for early-stage disease diagnosis.

Our first platform is designed to detect exosomes in serum with a theoretical limit of detection (LOD) as low as 100 exosomes per ml. It utilizes pAAO on CSPEs, capitalizing on the high surface area and customizable pore structures of pAAO [2] for effective exosome capture. The second platform focuses on miRNA detection in milk, boasting a theoretical LOD of 0.01 pM. This capability is achieved through structural and various target-specific optimizations of pAAO membraneson CSPEs for enhanced electrochemical sensing[3].

These platforms not only enhance diagnostic sensitivity and specificity but also allow for comprehensive analysis of biomarkers in complex biological fluids. Preliminary studies have demonstrated the feasibility of using pAAO for efficient capture and sensitive detection of both exosomes and miRNAs. Designed to be portable and suitable for point-of-care testing, our biosensing platforms offer substantial social, economic, and environmental benefits. They provide a cost-effective solution that is expected to reduce healthcare costs and minimize environmental impact by lowering the need for chemical reagents.

In conclusion, our advanced nanostructured biosensing platforms represent a transformative advancement in early disease diagnosis. With the capability to detect minute quantities of biomarkers in diverse samples, these platforms promise to improve diagnostic accuracy and patient outcomes worldwide.

Keywords: Exosomes, miRNAs, Early Disease Diagnosis, Porous Anodic Alumina, Biosensing Platforms, Point-of-Care Testing.

References

[1] C. O. Mărginean, L. E. Meliț, and M. O. Săsăran, "Traditional and Modern Diagnostic Approaches in Diagnosing Pediatric Helicobacter pylori Infection.," *Child. (Basel, Switzerland)*, vol. 9, no. 7, Jul. 2022, doi: 10.3390/children9070994.

[2] G. Rajeev, B. Prieto Simon, L. F. Marsal, and N. H. Voelcker, "Advances in Nanoporous Anodic Alumina-Based Biosensors to Detect Biomarkers of Clinical Significance: A Review," *Adv. Healthc. Mater.*, vol. 7, no. 5, p. 1700904, Mar. 2018, doi: https://doi.org/10.1002/adhm.201700904.

[3] G. Rajeev, E. Melville, A. J. Cowin, B. Prieto-Simon, and N. H. Voelcker, "Porous Alumina Membrane-Based Electrochemical Biosensor for Protein Biomarker Detection in Chronic Wounds," *Front. Chem.*, vol. 8, no. March, pp. 1–11, 2020, doi: 10.3389/fchem.2020.00155.

Advanced formula-oriented suspect screening workflow to unravel the early-life chemical exposome in silicone wristbands

Camilla Guerrini[1,2], M. Naghavi Sheikholeslami[1], R. Giné[2], J. M. Badia[2], M. Vinaixa[2,3], N. Ramírez[1,2,3]

[1] Institut d'Investigació Sanitària Pere Virgili (IISPV), Tarragona, Spain
[2] Universitat Rovira i Virgili, Department of Electronic Engineering, Tarragona, Spain
[3] CIBERDEM, Instituto de Salud Carlos III, Madrid, Spain

E-mail contact: **camilla.guerrini@estudiants.urv.cat**

Abstract

Early-life exposure to environmental chemicals represents a significant threat to later-life chronic disease development, potentially inducing epigenetic and metabolic changes. Despite the impact of early-life chemical exposures, few studies have comprehensively linked such exposures to child health outcomes. Target approaches overlook the potential health effects of dynamic environmental chemical exposures, focusing narrowly on specific compound classes. Therefore, using wide-scope strategies is crucial for assessing personal exposure and understanding the effects on health. Silicone wristbands have emerged as effective, low-cost, and child-friendly tools for capturing volatile and semi-volatile organic compounds. This study proposes characterizing the chemical exposome in wristbands worn by 218 children (8-11 years old) living in the area of Tarragona (Spain) using a wide-scope suspect screening workflow based on HERMES. HERMES, a molecular formula-oriented method, enhances MS spectral quality by generating sample-specific inclusion lists. 634 indoor and outdoor pollutants were detected. Preliminary results demonstrate that optimized MS/MS acquisition improved identification rates, advancing early-life exposome characterization.

1. Introduction

Exposure to environmental chemicals poses a significant global health threat, particularly to children. Increasing evidence suggests that such exposure can potentially induce epigenetic and metabolic changes, leading to chronic and non-communicable diseases that may go clinically undetected until later-in-life [1,2]. Given the underestimated long-term effects of children's exposure, comprehensively characterising the personal chemical exposome is crucial for understanding the link between early-life exposures and health outcomes. Traditional target approaches focus on determining specific classes of compounds, often overlooking the combined effects of multiple exposures. In environmental biomonitoring, a major challenge is developing a wide-scope screening approach to achieve a broader characterization of the chemical exposome and environment-health associations due to the low concentrations of chemicals and physicochemical properties [3]. Silicone wristbands (WBs) have recently emerged as low-cost, easy-to-use, child-friendly and non-invasive personal passive sampling devices for volatile and semi-volatile organic compounds [4]. An advanced wide-scope suspect screening workflow is presented to characterize the early-life chemical exposome. The workflow employed liquid chromatography/high-resolution mass spectrometry and a suspect screening analysis based on HERMES, an open-source R package [5]. HERMES is a molecular formula-oriented and peak detection-free optimization method to generate sample-specific and non-redundant inclusion lists (ILs) for MS/MS analysis.

2. Materials and Methods

***2.1**. Study population and sample collection*

This study is part of the ECHOES project and involved 218 children (8-11 years old) living in urban, suburban and rural areas around Tarragona (Spain), home of the largest petrochemical complex of Mediterranean area. Each participant wore a silicone wristband for 7 days between June 2022 to March 2023. The parents or legal guardians completed a questionnaire on household aspects, habits, passive tobacco smoke exposure, and socio-demographic data.

***2.2**. Wristband (WB) treatment*

Silicone wristbands, conditioned in a vacuum oven at 200ºC for 24 hours, were worn for 7 days, wrapped in aluminum foil, and stored at -20ºC until extraction. Each wristband was cleaned with MilliQ water and isopropanol, then cut into 1 cm pieces.

Around 2 g of WBs were spiked with deuterated internal standards (20 ng/mL d_3-nicotine and d_3-cotinine; 0.3 ng/mL d_9-nicotelline, d_4-NNN, d_4-NNK and d_3-NNAL). QuEChERS extraction involved 1 mL of MilliQ water, followed by 2 mL of ACN and 0.5 g of

the European Committee for Standardization (CEN) salts. After centrifugation at 4000 rpm for 5 min at 4 ºC, the organic layer (supernatant) was stored at -80 ºC until chromatographic analysis.

***2.3** Liquid Chromatographic and Mass Spectrometry Settings*

Analysis was carried out using an Orbitrap ID-X Tribrid mass spectrometer (Thermo Fisher Scientific, Massachusetts, USA) coupled with a Thermo Ultimate 3000 UHPLC system. 2 µL of WBs' extracts were injected into an Acquity UPLC BEH HILIC column at 25°C (Waters, Milford, MA, USA). ACN and ammonium acetate 50 mM in H_2O were used for gradient elution. MS detection operated in positive electrospray ionization mode (ESI+) with full scan mode covering the 50-900 m/z range. MS/MS acquisition was performed with a stepped collision energy at 10, 20, 30 and 40 V.

Quality control (QC) samples consisting of equal volumes of all extracts were injected at the beginning until the signal stabilisation and periodically every 8 samples.

***2.4.** Wide-scope Suspect Screening Strategy and Data Processing*

Thermo.raw data files were converted to mzML format using MSConvert software [6]. Then, MS1 data underwent processing with HERMES R package (version 0.99.0) to generate sample-specific inclusion lists for MS/MS analysis using 38147 unique molecular formulas from the NORMAN SusDat [7] and in-house thirdhand smoke database [8]. The XCMS R package (version 3.20.0) was used to quantify the feature.

***2.6**. Statistical analysis*

Principal components analysis (PCA) and heatmaps were performed through MetaboAnalyst 5.0 (www.metaboanalyst.ca) using quantified and annotated features after sample-specific normalization (WB weight), log transformation and autoscaling. Statistical results were then adjusted using the false discovery rate (FDR) p-value correction method. The correlations have a correlation coefficient exceeding 0.70 and a p-value lower than 0.05.

Figure 1- Analytical workflow for wide-scope suspect screening analysis based on HERMES.

3. Result and Discussion

Combining HERMES and XCMS results, 634 features have been comprehensively annotated with Schymanski identification level 4 [9] (exact mass with an error less than 5 ppm and theoretical isotopic pattern) using HERMES and MS2ID packages. An in-house database containing MS/MS spectra from MassBankEU, MoNA, HMBD, Riken, and NIST14 databases facilitated annotation. Spectral matches with similarity scores >0.8 underwent manual verification using the MS2IDgui interface for confirmation.

Indoor and outdoor chemicals include tobacco smoke pollutants, pharmaceuticals, personal care products, insect repellents, and plastic additives.

Among them, 29 were confirmed by matching with database MS/MS spectra (level 2), while nicotine, cotinine and nicotelline were identified by retention time. Focusing on tobacco-related compounds, Figure 2 illustrates that while PC1 (representing 84.3% variability) reflects pervasive and underestimated tobacco smoke exposure. Despite reports indicating 36% direct home exposure among children, our study found nicotine, cotinine, nicotelline, and myosmine (a specific tobacco alkaloid) in 80% of participants. This underscores the need for future policy and regulatory decisions.

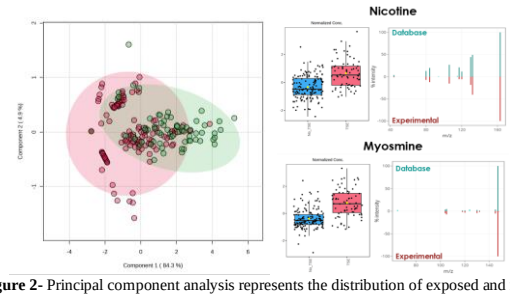

Figure 2- Principal component analysis represents the distribution of exposed and non-exposed children at home using tobacco-related compounds as variables (on the left). Box plots of the distribution of the two influential features between exposed and non-exposed children to tobacco smoke (TSE) and their mass spectrum (on the right).

7. Conclusions

The preliminary results show how the use of silicon wristbands in combination with our suspect screening workflow based on HERMES enhances the characterisation of the personal chemical exposome (634 annotated compounds). Hermes is a relevant tool for MS/MS annotation. Indeed, focusing on sample-specific and environmentally relevant compounds it improves MS/MS coverages, mass spectral similarity, and identification rates. Additionally, the results confirm the ubiquity of tobacco smoke exposure and the necessity of future political decisions and regulatory perspectives.

References

[1] Gluckman PD et al. Effect of in utero and early-life conditions on adult health and disease. New England Journal of Medicine DOI: 10.1056/NEJMra0708473

[2] WHO Air pollution and Child Helth. Prescribing clean air, 2018

[3] Schymanski El et al. Empowering large chemical knowledge bases for exposomics: PubChemLite meets MetFrag. DOI: 10.1186/s13321-021-00489-0.

[4] Anderson K. et al., Preparation and Performance Features of Wristband Samplers and Considerations for Chemical Exposure Assessment. J Expo Sci Environ Epidemiol 2017, 27 (6), DOI: 551–559. https://doi.org/10.1038/jes.2017.9.

[5] Giné Ret al. HERMES: a molecular formula-oriented method to target the metabolome. 2021:2021.03.08.434466. DOI: 10.1101/2021.03.08.434466.

[6] Holman, J.D, et al., Employing ProteoWizard to convert raw mass spectrometry data. DOI:10.1002/0471250953.bi1324s46.

[7] NORMAN SusDat , DOI: 10.5281/zenodo.2664077

[8] Thirdhand smoke database, DOI: 10.5281/zenodo.5395357 and 10.5281/zenodo.2669467

[9]Schymanski E. et al., Identifying Small Molecules via High Resolution Mass Spectrometry: Communicating Confidence, Environ. Sci. Technol. 2014, 48, 4, 2097–2098, DOI: https://doi.org/10.1021/es5002

The effect of the substrate on the sensing properties of graphene and MnO_2 loaded graphene.

Mohamed Ayoub Alouani, Juan Casanova Chafer, Xavier Vilanova

Universitat Rovira I Virgili
mohamedayoub.alouani@urv.cat, juan.casanova@urv.cat, xavier.vilanova@urv.cat

Abstract

This work studies the behavior of the different prepared pristine graphene and graphene loaded with manganese oxide (MnO_2) sensors when it comes to detecting nitrogen dioxide (NO_2) deposited on a variety of substrates consisted of ceramic, silicon and Kapton. the decorated nanolayers were characterized using several techniques such as X-Ray Diffraction and Field Emission Scanning Electron Microscopy. The sensors exhibited different behaviors, decorated layers deposited on silicone showed the best responses, better than the pristine graphene on the same substrate and also the other sensors deposited on Kapton and ceramic substrates.

1. Introduction

Gas sensors play an increasingly important role in our modern society, particularly for industrial gas emisión control and public health security. Among many different gases, the rapid detection of dangerous gases such as nitrogen dioxide (NO_2) is technologically essential as these gases are causing atmospheric contamination (green house effect) and can be dangerous for human health. Chemioresistive sensors have been presented as one of the promising sensors for detecting these type of gases due to their high sensitivity, low cost, reproducibility and simplicity. Thanks to its extraordinary high Carrier density and mobility, Graphene was seen as the ideal candidate to make these chemioresistive gas sensors and to improve these characteristics, manganese oxide was used as an enhancing agent to be loaded in the Graphene since they have exceptional properties such as low toxicity, low cost, high stability, ease of fabrication.

2. Materials and Methods

2.1 Substrates fabrication:

Gold electrodes were deposited on top of the Kapton substrates using the Sputtering technique. To obtain the desired shape of the interdigitated electrodes, a shadow mask with the shape of the electrodes was fixed on top of the Kapton substrate and later gold was deposited with a thickness of 9nm. Moreover, to obtain the silicon substrate, a similar process took place except this time the shape of the electrodes was designed using laser on the surface of the substrate and the next step consisted of sputtering a layer of titanium first with a thickness of 10nm and on top of that gold was deposited with a thickness of 100nm. Ceramic substrates were obtained from Romania (commercial ceramic substrates).

2.2 Sensors preparation:

Pristine graphene and MnO_2 loaded graphene were obtained from GNANOMAT company in powder forms, these powders were dissolved in ethanol and later deposited on the previously fabricated substrates via the spray coating method while heating up to 55°C.

2.3 Material characterization:

The obtained sensors were characterized using different techniques such as Field Emission Scanning Electron Microscope (FESEM) using a Carl Zeiss AG-Ultra 55 (Germany) to study the surface morphology and X-Ray diffraction (XRD) to confirm the phase of the graphene and the presence of the MnO_2 nanomaterial.

2.4 Gas sensing measurements:

The resistance changes under NO_2 gas and experimental conditions were monitored using an Agilent HP 34972A multimeter connected to the gas sensing chamber.

3. Results

3.1 Material Characterization:

Figure 1.a shows the XRD graph of pristine graphene with a major slightly sharp peak appearing at $2\Theta = 26.5$ meaning the material have a good crystallinity, another specific peak appears at $2\Theta = 44$. Meanwhile in Figure 1.b, we have the same graphene specific peaks at the same steps alongside with new peaks belonging to MnO_2 nanomaterial, one at $2\Theta = 12.5$ and the other at $2\Theta = 37$.

Figures 2.a 2.b and 2.c shows the FESEM images of the surface of the sensing layers deposited on different substrates presents a very homogeneous layers with some bright spots appearing when using a back-

scattered electron detector (BSE) corresponding to MnO_2.

3.2 Gas sensing results

Nitrogen Dioxide (NO2) detection was performed by applying repeated exposure and recovery cycles to increasing concentrations of the gas at room temperature under dry conditions. Figure 3 shows the calibration curves obtained for 200-400-600-800-1000 ppb of NO_2 in which pristine graphene and graphene loaded with MnO_2 deposited on the silicon substrate present the highest responses of 9.4% and 9% at 800 ppb respectively and also no matter the concentration of the analyte they are still showing the best results, it is observed also that the loading of the graphene enhanced its gas sensing performance since it has higher response than the pristine one. Meanwhile, its quite the opposite when it comes to the other sensing layers deposited on Ceramic and Kapton, since the pristine materials show higher responses towards NO_2 than their graphene loaded with MnO_2 counterparts. Pristine graphene deposited on Ceramic has a response of 7.8% at 1000pb which higher than graphene loaded with MnO_2 (response of 3.4% at the same NO_2 concentration). Regarding the sensing materials deposited on Kapton, the MnO_2 loaded graphene shows the worst response out of all the other sensors deposited on the different substrates which is 2.7% at 1000 ppb and still almost 2 fold worse than pristine graphene deposited on the same substrate (4.6% at 1000 ppb of NO_2)

4. Conclusion:

In conclusion, Kapton and silicon substrates were fabricated using a very easy process and cheap techniques, graphene and graphene loaded with MnO2 were successfully deposited on the different substrates via the spray coating technique which is also easy and cheap and a study of the behaviour of these sensors was conducted by exposing them to different concentrations of NO_2. The responses of these sensors were different from on type of substrate to another, the sensors deposited on silicon showed the highest responses out of all the other types of substrates and the MnO_2 loaded graphene on Silicon is the best fabricated sensor showing a response of 9.4% at 800 ppb, the worst sensor was the MnO_2 loaded graphene deposited on Kapton with a response of 2.7% at 1000ppb. Moreover, the pristine graphenes deposited on Kapton and ceramic substrates exhibited higher responses than their loaded counterparts, this could be attributed to the adhesion of the sensing layers ontop of the different substrates.

5. Graphs

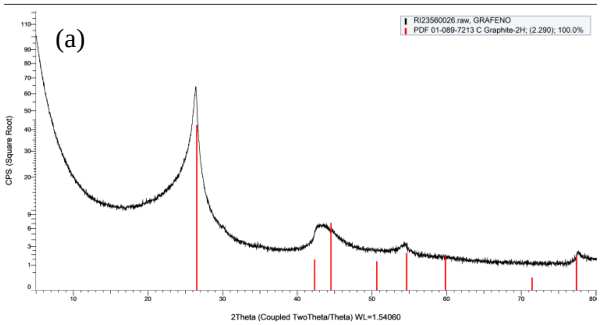

Fig.1.a X-Ray diffraction of pristine graphene powder.

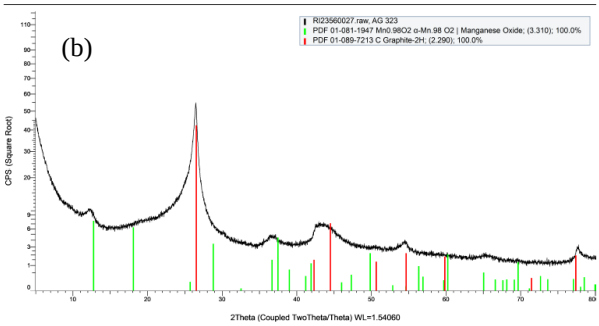

Fig.1.b X-Ray diffraction of graphene loaded with MnO_2 powder.

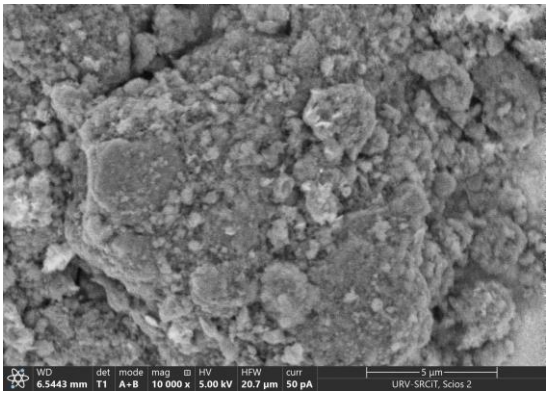

Fig.2.a FESEM image recorded with Back-Scattered Electron (BSE) detector of Graphene loaded with MnO_2 on Ceramic substrate.

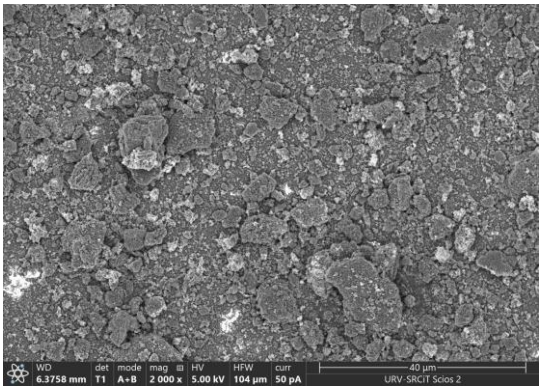

Fig.2.b FESEM image recorded with Back-Scattered Electron (BSE) detector of Graphene loaded with MnO_2 on Kapton substrate.

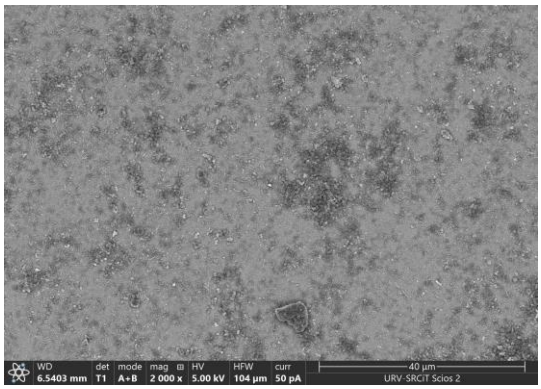

Fig.2.c FESEM image recorded with Back-Scattered Electron (BSE) detector of Graphene loaded with MnO_2 on Silicon substrate.

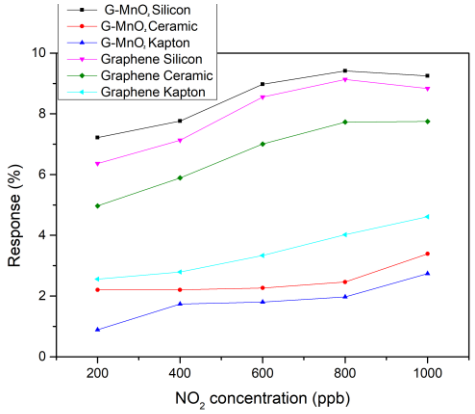

Fig.3 Calibration curves obtained for pristine graphene deposited on Silicon, Ceramic and Kapton substrates and MnO_2 loaded graphene deposited on the same substrates.

IoT and ANN Integration for Air Pollution Monitoring

Alejandro Santos-Betancourt, José Carlos Santos-Ceballos, Foad Salehnia, Mohamed Ayoub Alouani, Alfonso Romero, José Luis Ramírez, and Xavier Vilanova

MINOS Research Group, Department of Electronic, Electric and Automatic Engineering, School of Engineering, Universitat Rovira i Virgili, 43007 Tarragona, Spain.
e-mail: alejandro.santos@urv.cat, josecarlos.santos@urv.cat, foad.salehnia@urv.cat, mohamedayoub.alouani@urv.cat, alfonsojose.romero@urv.cat, joseluis.ramirez@urv.cat, xavier.vilanova@urv.cat

Abstract

This work presents the design and setup of an IoT platform at level four of the technology readiness level (TRL-4), to monitor pollutant gases. The IoT platform consists of several gas sensor nodes (GSNs) with Wi-Fi capability to send data to a server and its user interface (UI). Each GSN interfaces one sensor array (up to four chemoresistor gas sensors and one temperature and humidity sensor). The user interface was designed in two stages. First (training stage), sensor data was received, stored, and employed to train different multilayer perceptron (MLP) artificial neural networks (ANNs). Second (recognition stage), obtained models were implemented in the UI to classify and quantify the presence of pollutants. The platform was tested in laboratory conditions under exposure to NO_2 and NH_3 at different % RH. As a result, the platform improves the classification and quantification times compared with the single-sensor approach. Additionally, the system was evaluated using a gas mixture of both gases, demonstrating a classification accuracy exceeding 99 %. Likewise, the training and recognition stages can be repeated to use new chemoresistor gas sensors in the node, add new nodes to the platform with new sensors, and deploy the nodes in different scenarios.

1. Introduction

Gas sensors and their read-out instrumentation systems are essential components in various industry applications, due to their crucial role in ensuring safety, enhancing efficiency, and maintaining environmental standards [1]. Nowadays, active research is directed at discovering new materials, to increase the response and the selectivity of new gas sensors. Among them, chemoresistor gas sensors usually show high sensitivity to gases and fast response and recovery times. However, some drawbacks are still challenging, like the lack of selectivity to specific target gases, temperature and humidity interferences, long-term drift, and high working temperatures [2]. A promising area of research to partially solve these issues is using chemoresistor sensors like MOX-based sensors doped or decorated with other materials like graphene or conductive polymers [3]. Combining this approach with the use of arrays of sensors [4], and multivariate analysis allows the compensation of the interferences that a single sensor might have [5]. This work presents a reconfigurable design of an IoT platform at TRL-4, to monitor pollutant gases, which integrate these characteristics.

2. IoT platform and GSN

The platform has three main parts (Fig. 1.a): a server running an MQTT broker, a UI, and the GSNs interfacing with an array of sensors. The array of sensors is formed by a BME680 sensor (to acquire the humidity and temperature), and four chemoresistor gas sensors: two based on WO_3 (AACVD), and two based on graphene, (airbrushing, Graphene@ZnO and laser induced LIG@Ppy). The fabrication process and characterization of these sensors were previously reported by our research group [6], [7], [8].

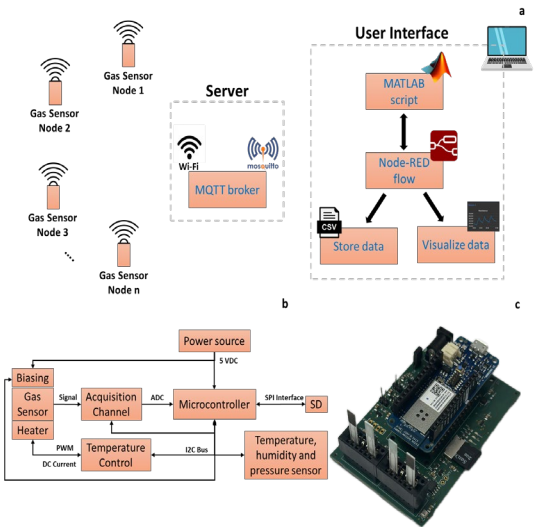

Fig. 1. (a) IoT platform (b). Block diagram, GSN. (c) Fabricated GSN

Key components on the GSN board (Fig. 1.b, 2.c) are the sensors, the microcontroller, the analog acquisition channel, the temperature control circuit, and the power source. The microcontroller is based on Arm® Cortex®-M0 32-bit SAMD21 microcontroller (Arduino MKR 1000 Wi-Fi). The GSN can dynamically adjust

the chemoresistor gas sensors' bias, the saturation voltage in the ADC input, the working temperature of each gas sensor separately, and change the save-data mode between wireless or µSD.

3. Gas sensing and Training Stage

One GSN was exposed to different concentrations from 100 ppb to 500 ppb incremented by 100 ppb of NO_2. Also, was exposed to NH_3, from 10 ppm to 50 ppm incremented by 10 ppm. The gas exposure time was 45 min, and the recovery dry airtime was 180 min for each pulse. The cycle of pulses was repeated 3 times, within 3 hours of recovery time between cycles. The experiment was performed 2 times at 65 % RH and at 25 % RH. Afterward, both gases were injected into the chamber at the same time, getting the exposure of the system to a mixture of gases (Fig. 2.).

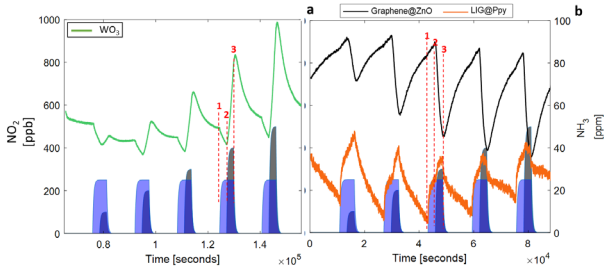

Fig. 2. Temporary response under a mixture of NO_2 and NH_3. (a) pristine WO_3 (b) Graphene-based.

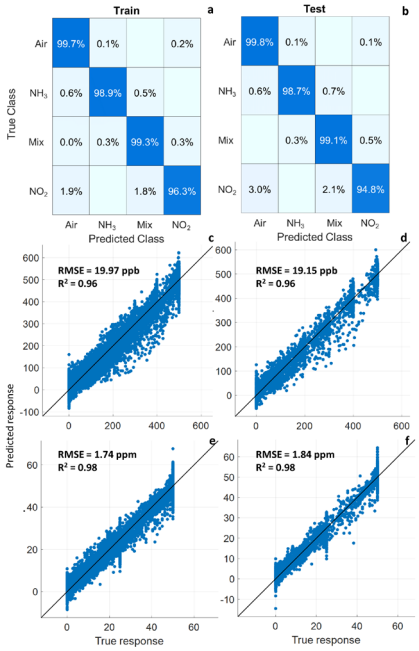

Fig. 3. Train and test MLPs under a mixture. (a, b) Classification: 1 HL, 100 NL, Sigmoid. (c, d) Quantification NO_2: 1 HL, 100 NL, ReLU. (e, f) Quantification NH_3: 1 HL, 100 NL, Sigmoid.

All sensors were used as input features (input layer) for the training process. After a data pretreatment (filtering and normalization), 80 % of observation were selected for training the MLPs and 20 % for testing (randomly selected). A 5-fold cross-validation scheme was used to avoid overfitting. The architecture of the MLP was tuned by varying the number of hidden layers (HL: 1, 2, 3) and neurons per layer (NL: 10, 25, 100). Also, the activation function was varied (AF: ReLU, Sigmoid, and Tanh) to determine the best option (Fig. 4.).

4. Recognition stage

Fig. 4.a shows a qualitative comparison between the platform and single-sensor approaches. For nitrogen dioxide $t_{\_resp}$ sensor is bigger than $t_{\_prediciton\text{-}up}$. Also, $t_{\_recov}$ sensor is bigger than $t_{\_prediciton\text{-}down}$. A similar result is found when analyzing Fig. 5.b, this time under ammonia exposure. In both cases, the comparison was performed using the selective sensor of each gas, and it was noticed that using the platform reduces the quantification and classification time by around 40 %.

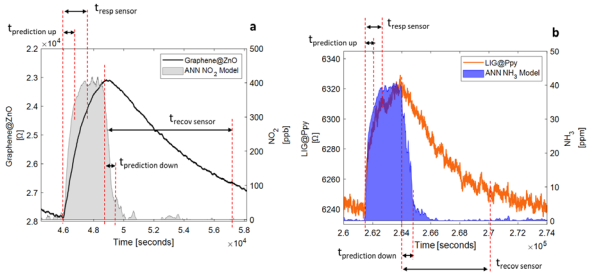

Fig. 4. MLP output vs single sensor. (a) NO_2 (b) NH_3.

5. Conclusions

The platform has been successfully tested in laboratory conditions. Is ready to be deployed in real-application scenarios. Replacing the sensors is quickly achievable by repeating the training and recognition stages described during this work. Software and hardware were designed in layers; therefore, physical communication layer can be replaced to adapt the platform to the final application. Since communication protocol is based on the MQTT, adding new nodes is as easy as configuring new topics on the new nodes to be added. Therefore, deploying this IoT platform in a real application will be a suitable next step to continue this study.

References

[1] P. Amoatey, H. Omidvarborna, M. S. Baawain, and A. Al-Mamun, "Emissions and exposure assessments of SO_X, NO_X, $PM_{10/2.5}$ and trace metals from oil industries: A review study (2000–2018)," Process Safety and Env. Protection, vol. 123, pp. 215–228, Mar. 2019.

[2] D. Sales-Lérida, A. J. Bello, A. Sánchez-Alzola, and P. M. Martínez-Jiménez, "An Approximation for Metal-Oxide Sensor Calibration for Air Quality Monitoring Using Multivariable Statistical Analysis," Sensors, vol. 21, no. 14, p. 4781, Jul. 2021.

[3] X. Tang, M. Debliquy, D. Lahem, Y. Yan, and J.-P. Raskin, "A Review on Functionalized Graphene Sensors for Detection of Ammonia," Sensors, vol. 21, no. 4, p. 1443, Feb. 2021.

[4] J. Pan et al., "Lightweight Neural Network for Gas Identification Based on Semiconductor Sensor," IEEE Trans Instrum Meas, vol. 71, pp. 1–8, 2022.

[5] S. Rahman et al., "Wireless E-Nose Sensors to Detect Volatile Organic Gases through Multivariate Analysis," Micromachines (Basel), vol. 11, no. 6, p. 597, Jun. 2020.

[6] J. C. Santos-Ceballos, F. Salehnia, A. Romero, X. Vilanova, and E. Llobet, "Low Cost, Flexible, Room Temperature Gas Sensor: Polypyrrole-Modified Laser-Induced Graphene for Ammonia Detection," IEEE Sens J, vol. 24, no. 7, pp. 9366–9374, Apr. 2024.

[7] A. Santos-Betancourt et al., "ZnO Decorated Graphene-Based NFC Tag for Personal NO2 Exposure Monitoring during a Workday," Sensors, vol. 24, no. 5, p. 1431, Feb. 2024.

[8] È. Navarrete et al., "WO_3 nanowires loaded with cobalt oxide nanoparticles, deposited by a two-step AACVD for gas sensing applications," Sens Actuators B Chem, vol. 298, p. 126868, Nov. 2019.

Study of the Transport Mechanism in MoS_2 FETs, Using Modeling and Simulation of a Fabricated Device

Anisleidy Broche [a], Benjamín Iñiguez [b], Antonio Cerdeira [a], Magali Estrada [a]

[a] Center of Research and Advanced Studies at IPN, Mexico City (cinvestav@cinvestav.mx, anisleidy.broche.f@cinvestav.mx, cerdeira@cinvestav.mx, mecueto@yahoo.com)
[b] Department of Electronic and Electric Engineering and Automatic, University Rovira I Virgili, Tarragona, Spain, (a.mounir90@gmail.com, benjamin.iniguez@urv.cat)

Abstract

In the search for new semiconductor materials capable of mitigating short-channel effects, two-dimensional semiconductor field effect transistors (2D FETs) have emerged. This study analyzes the transport mechanism of a MoS_2 FET through modeling and simulation. The device was fabricated with a back gate structure on a Pt/TiN/p++-Si substrate. It was observed that the dependence of mobility on the gate voltage follows a potential law, suggesting that the predominant charge transport is the Variable Range Hopping (VRH) mechanism. Results show that the linear transfer curve, obtained by electrical simulation considering the presence of the localized states, reproduces the experimental behavior observed in the device. It is also shown a good coincidence obtained between the measured and modeled transfer curves, when the presence of localized states on device performance is considered.

1. Introduction

Searching for new semiconductor materials capable of mitigating short-channel effects, 2D FETs have emerged, where the layers of materials are held together by Van der Waals forces.[1] An example of these 2D semiconductors is molybdenum disulfide, which also has the property of a large bandgap [2].

In this work, we study the transport mechanism observed in fabricated devices, using modeling and simulation of a device that uses MoS_2 as a semiconductor.

Characteristics of the Measured Structure

To study the transport mechanisms in MoS_2 FET, one of the devices fabricated in [3] was used. This device consists of a back gate FET, using the structure Pt/TiN/p^{++}-Si as substrate. On this substrate, 50 nm of Al_2O_3 were deposited via atomic layer deposition (ALD), achieving an EOT of 22 nm. A MoS_2 monolayer layer was grown using MOCVD on a sapphire substrate and transferred to the Al_2O_3 layer using a PMMA-assisted wet transfer process. Electron beam lithography and dry plasma etching with SF_6 were used to define the channel area. Finally, a contact stack of 40 nm Ni and 30 nm Au was deposited by evaporation, as shown in **figure 1**.

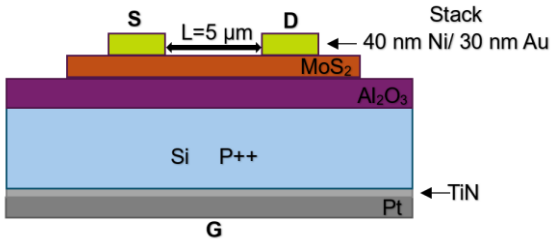

Fig. 1 Measured Estructure

2. Modeling

For the deposition method used, it can be assumed that MoS_2 layers are crystalline. However, structural disorder due to defects and grain boundaries have been observed in them[4]. which can give rise to a density of localized states in the bandgap, and consequently to a VRH transport mechanism. Modeling of the linear transfer curve was done using the Unified Model and Extraction Procedure (UMEM), which considers VRH [5]. **Figures 2** and **3** show the good coincidence between measured and modeled curves.

3. Simulation

Electrical simulation of the device was done in Silvaco's ATLAS simulator [6]. The characteristics of MoS_2 are shown in Table 1.

Parameter	MoS_2
Band Gap (eV)	1.84
Electron Affinity (eV)	4.2
Nc (cm^{-3})	$5*10^{18}$
Nv (cm^{-3})	$5*10^{18}$
Permittivity	2.6

Table1. Material parameters for MoS_2

Initially, various contact resistance values were tested to determine which generated a curve shape most similar to the experimental measurement. Subsequently, the effect of the parameter q_f was studied to find a value that adjusted the threshold voltage (Vt).
The simulation considered a structure with a continuous distribution of localized states, following the guidelines of [6]. Values were assigned only to the localized acceptor states, as the semiconductor is n-type. Several tests demonstrated that the transport mechanism depended more on tail states than on deep states. **Table 2** presents the values assigned to the parameters of the localized states:

Parameter	Value
Density of acceptor tail traps (cm^{-3}) g_{tao}	$7*10^{20}$
Characteristic energy of tails traps E_{at} (eV)	0.05

Table2. Parameters assigned to the DOS

No values were assigned to deep states, as they do not significantly contribute to the linear transfer curve. **Figures 2** and **3** show the agreement between measured and simulated curves.

4. Analysis

The device modeling shows that mobility potentially depends on Vg, corresponding to a VRH transport mechanism. Simulation of the linear transfer characteristic, considering the presence of continuous distribution of localized states in the semiconductor gap, confirms that the expected VRH transport mechanism is the predominant.
The slight differences observed between the simulated and experimental graphs may stem from certain material characteristic parameters that can vary within a certain range. For instance, the material permittivity of MoS_2, which depends on the deposition method, can range from 2.6 to 2.9. It should be noted that the accuracy of the simulated data may be influenced by the contact resistance, which has not been directly measured in the fabricated structure
In the simulation, a contact resistance value of 15 kΩ and a mobility of 27 $cm^2V^{-1}s^{-1}$ were used, which are close to the reported in [3].

5. Conclusions

The transport mechanism observed in MoS_2 2D FETs is primarily governed by VRH due to acceptor tail states present in the semiconductor gap. The small discrepancies between simulated and experimental transfer characteristics may be attributed to variations in material parameters such as MoS_2 contact resistance and permittivity, which depend on fabrication method and material physical properties.

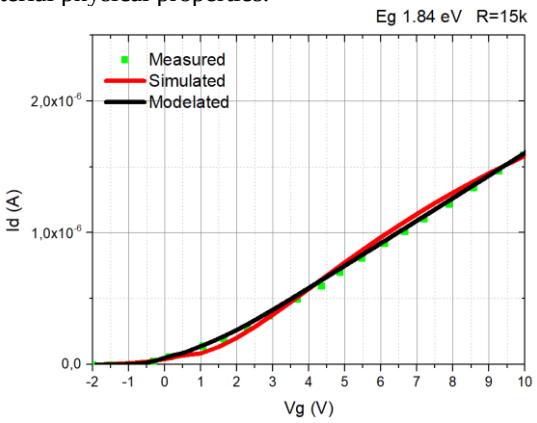

Fig.2. Linear Transfer Curve

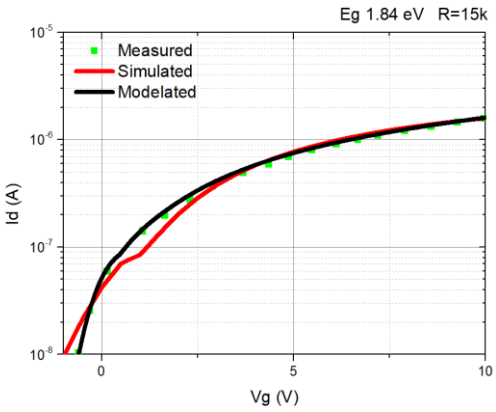

Fig.3. Semilog Transfer Curve

References

[1] S. B. Mitta *et al.*, "Electrical characterization of 2D materials-based field-effect transistors", *2D Mater.*, vol. 8, no.1, p. 012002, Jan. 2021, https://doi.org/10.1088/2053-1583/abc187

[2] R. Mathew and J. Ajayan, "Material processing, performance and reliability of MoS_2 field effect transistor (FET) technology- A critical review", *Mater. Sci. Semicond. Process.*, vol. 160, p. 107397, Jun. 2023, https://doi.org/10.1016/j.mssp.2023.107397

[3] A. Sebastian, R. Pendurthi, T. H. Choudhury, J. M. Redwing, and S. Das, "Benchmarking monolayer MoS_2 and WS_2 field-effect transistors", *Nat. Commun.*, vol. 12, no.1, p. 693, Jan. 2021, https://doi.org/10.1038/s41467-020-20732-w

[4] A. M. Van Der Zande *et al.*, "Grains and grain boundaries in highly crystalline monolayer molybdenum disulphide", *Nat. Mater.*, vol. 12, no. 6, pp. 554–561, Jun. 2013, https://doi.org/10.1038/nmat3633

[5] M. Estrada, I. Mejía, A. Cerdeira, J. Pallares, L. F. Marsal, and B. Iñiguez, "Mobility model for compact device modeling of OTFTs made with different materials", *Solid-State Electron.*, vol. 52, no. 5, pp. 787–794, May. 2008, https://doi.org/10.1016/j.sse.2007.11.007

[6] "Atlas User Manual Device Simulation Software". Jan. 2020, www.silvaco.com

Electrochemical Polyaniline Deposition on Laser-Induced Graphene Sensor for Ammonia Detection at Room Temperature

José Carlos Santos-Ceballos, Foad Salehnia, Alfonso Romero, Xavier Vilanova

Universitat Rovira i Virgili, Microsystems Nanotechnologies for Chemical Analysis (MINOS), Tarragona, Catalunya, Spain
josecarlos.santos@urv.cat

Abstract

This study explores the electrochemical modification of laser-induced graphene (LIG) with polyaniline (PANI), resulting in the creation of a flexible chemoresistive PANI@LIG gas sensor for detecting ammonia (NH_3) levels at room temperature. The results obtained demonstrate that the deposition of PANI on LIG improves the response to NH_3. This work presents the first-time utilization of PANI@LIG for gas sensing and introduces a simple, yet effective, approach for fabricating wearable gas sensors that exhibit promising characteristics, including high sensitivity and flexibility. The findings open new avenues for developing low-cost, efficient, and portable gas detection systems.

1. Introduction

Ammonia measurement is important in diverse applications from air quality monitoring to agricultural regulation and chemical industry safety. Due to the dangerous nature of NH_3, it is crucial to develop sensitive sensors for real-time monitoring [1]. In recent years, many NH_3 sensors have been developed, employing different technologies such as optical, electro-chemical, and chemoresistive with both metal oxides and graphene-based sensors [2]. Among these, graphene-based sensors have increased their interest due to their ability to work at room temperature, making them an ideal candidate for wearable gas sensor applications [3]. However, traditional graphene synthesis methods pose challenges in terms of cost and integration into flexible electronics.

In 2014, a breakthrough approach was introduced for producing porous graphene films from commercial polymer films using a CO_2 infrared laser, termed laser-induced graphene (LIG) [4]. LIG exhibits high porosity, excellent electrical conductivity, and good mechanical flexibility making it suitable for various applications including electronic devices, catalysis, water purification, and biosensors [4]. Also, it has been used in gas sensing applications. Despite its potential, the utilization of LIG in NH_3 sensing has been limited due to its low response to this gas. Previous works have demonstrated that loading graphene with polyaniline (PANI) improves its sensitivity to NH_3 [5]. Building upon this concept, the current research works to develop an electrochemical method for fabricating gas sensors utilizing PANI@LIG.

2. Materials and Methods

For the fabrication of the LIG gas sensor (Fig.1 (a)), a commercially available polyimide film (50 µm) was used as a flexible substrate. LIG was synthesized using a CO_2 laser operating at a max power of 25 W. The laser beam scanned over the surface at a speed of 200 mm/s, a frequency of 12 kHz and 12% of laser power. The sensor has been designed with a sensing area of 3 x 6 mm^2. To improve the connection of the sensor with the measurement system, Ag ink was drop-casted on the region of the electrodes.

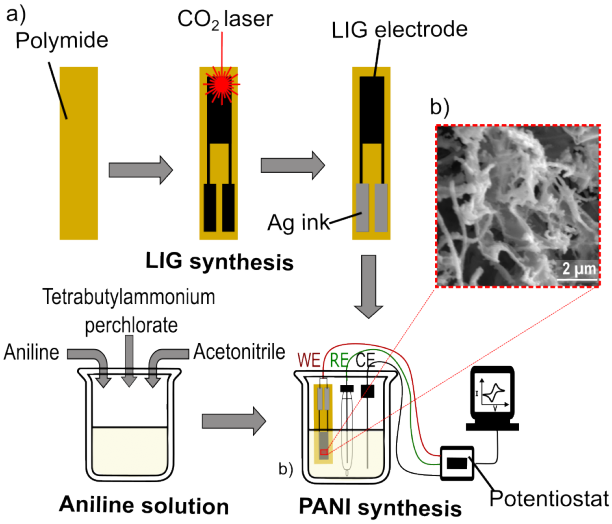

Fig.1. Schematic illustration showing (a) the fabrication process and (b) SEM images of the PANI@LIG gas sensor.

Electrochemical growth was carried out using a potentiostat. A 3-electrode system comprised of bare LIG as working electrode, platinum wire auxiliary electrode, and Ag/AgCl reference electrode was used for experiments. The nanocomposite was prepared by cyclic voltammetry method electrode cycled at 50 mV/s between -0.2 and 1.3 V for 20 cycles in polymerization solution (0.1 M aniline/0.5 mM tetrabutylammonium perchlorate as the electrolyte /acetonitrile)

3. Results and Discussion

The SEM images show the morphology of PANI@LIG (Fig. 1(b)). The Raman spectra (Fig. 2) revealed prominent peaks corresponding to the characteristic vibrational modes of graphene and polyaniline.

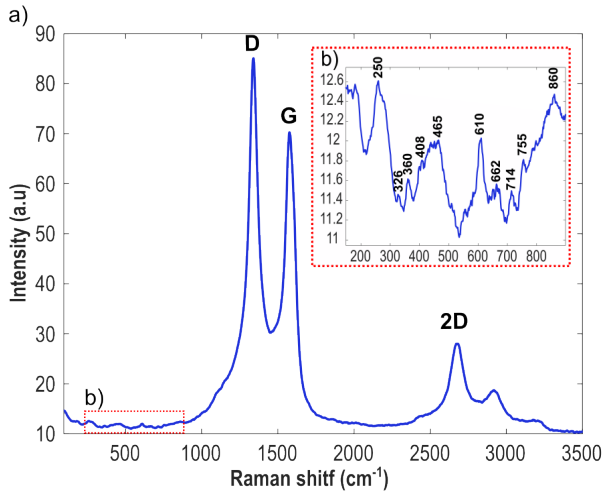

Fig.2. Raman spectra of (a) the PANI@LIG gas sensor and (b) peaks corresponding to polyaniline.

The sensing performance of the LIG gas sensors developed for NH_3 detection was assessed through repeated cycles of response and recovery to concentrations of 5, 10, 25, 50, and 100 ppm. Fig. 3 illustrates the typical dynamic responses observed for the bare LIG (blue dots) and the PANI@LIG (red dots) gas sensors. The sensor responses (electrical resistance change) increased upon exposure to the target gas. The raised electrical resistance results from the decreased hole density and electrical conductivity of the p-type LIG upon exposure to the reducing NH_3 (electron donating). Fig. 3 demonstrates that the doped sensor shows an improved response and signal-to-noise ratio compared to the bare sensor. The PANI@LIG sensor exhibits responses that are up to 1.5 times higher in terms of the intensity of resistance changes induced by exposure to ammonia, compared to bare LIG.

Based on the experimental results, it can be inferred that although the response of the PANI@LIG sensor is not significant compared to that obtained in other investigations, the combination of these two nanomaterials exhibits a synergistic sensing effect, in which LIG and PANI interact with the NH_3, resulting in superior chemical gas sensing performance.

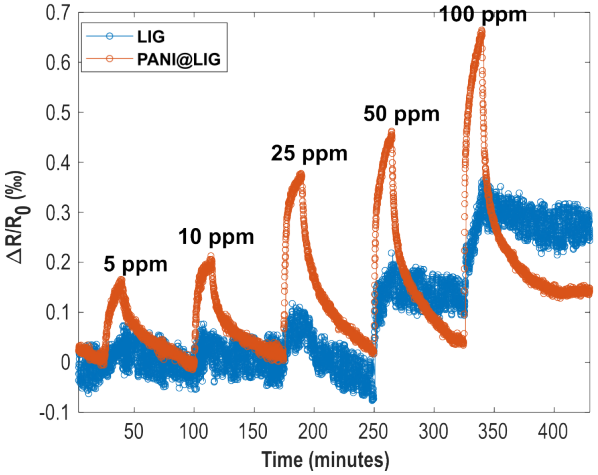

Fig.3. Sensing performance of bare LIG (blue dots) and PANI@LIG (red dots) gas sensors to different concentrations of NH_3 at room temperature.

4. Conclusions

The development of a flexible room temperature chemical resistive sensor opens possibilities for NH_3 monitoring systems, offering advantages like a simple interface circuit, cost-effectiveness, low power consumption, and high portability, ideal for wearable gas sensors. Further optimization of electrochemical deposition methods is needed to enhance NH_3 sensor response, alongside comprehensive studies on humidity effect, repeatability, stability, and selectivity for future improvements.

References

[1] S. Aarya, Y. Kumar, and R. K. Chahota, "Recent Advances in Materials, Parameters, Performance and Technology in Ammonia Sensors: A Review," *J Inorg Organomet Polym Mater*, vol. 30, no. 2, pp. 269–290, Feb. 2020.

[2] D. Kwak, Y. Lei, and R. Maric, "Ammonia gas sensors: A comprehensive review," *Talanta*, vol. 204, pp. 713–730, Nov. 2019.

[3] X. Tang, M. Debliquy, D. Lahem, Y. Yan, and J. P. Raskin, "A Review on Functionalized Graphene Sensors for Detection of Ammonia," *Sensors 2021, Vol. 21, Page 1443*, vol. 21, no. 4, p. 1443, Feb. 2021

[4] T. D. Le *et al.*, "Recent Advances in Laser-Induced Graphene: Mechanism, Fabrication, Properties, and Applications in Flexible Electronics," *Adv Funct Mater*, vol. 32, no. 48, p. 2205158, Nov. 2022.

[5] Y. Guo *et al.*, "Hierarchical graphene–polyaniline nanocomposite films for high-performance flexible electronic gas sensors," *Nanoscale*, vol. 8, no. 23, pp. 12073–12080, Jun. 2016

Discrete-Time Control of a Bidirectional AC-DC Buck-Boost Converter with Input Filter

Alexandra Blanch-Fortuna*(1), Enric Vidal-Idiarte(1), Francisco Javier Calvente-Calvo(1)

Department of Electronics, Electrics and Automatic Control Engineering, Rovira I Virgili University, 43007, Tarragona, Spain, Email: alexandra.blanch@urv.cat

Abstract

This study presents the design of a discrete control system for a bidirectional non-inverting buck-boost converter operating as a rectifier-inverter with **power factor correction** (PFC). The converter's operation in step-down mode is characterized by a pulsating input current, emphasizing the necessity for properly dimensioning an input filter for the AC-DC converter. Control requirements are addressed through the synthesis of the **loss-free resistor** (LFR) concept using **discrete-time sliding mode control** (DSMC).

1. Introduction

Electric vehicles (EVs), initially considered merely as energy consumers, have gained widespread popularity due to their use of clean energy and technological advancements in batteries. Governments, such as Spain with the MOVES III plan [1] and the European Union with the Green Deal [2], support decarbonization and an increase in EV presence on the electrical grid. This necessitates a robust power infrastructure for a future where EVs replace combustion vehicles and take on active roles, such as generators in smart charging modes (V2L, V2V, V2H, V2G) [3]-[4].

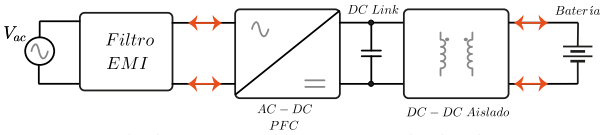

Fig.1. "Typical structure of a two-stage single-phase OBC."

To diversify the use of EV batteries, it is crucial that onboard chargers (OBCs) have the capability of both step-up and step-down converter topologies, enabling energy transfer in both directions. Two-stage OBCs, as depicted in Figure 1, typically comprise an AC-DC converter, usually a step-up converter, which is responsible for power factor correction and harmonic distortion correction. This stage usually incorporates an EMI filter to mitigate electromagnetic interference. The second stage consists of a galvanically isolated DC-DC converter. However, given the state of charge considerations for 400 V batteries, there is a growing trend towards investigating both step-up and step-down AC-DC topologies. These configurations would ensure that the galvanically isolated DC-DC converter operates at the nominal input/output ratio, thereby enabling variable voltage in the DC link capacitor and improving overall system efficiency.

In this context, the present study aims to explore the application of the widely used non-inverting buck-boost converter in DC-DC converters for charging 400 V OBCs architectures.

2. System Description and Operation

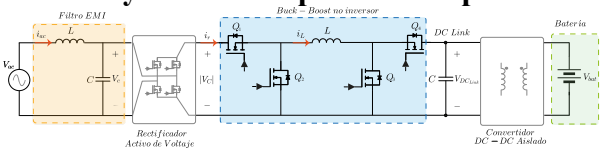

Fig.2. Two-stage bidirectional structure with non-inverting buck-boost converter for single-phase onboard charger.

The battery voltage, ranging from 200 to 450 V, determines whether the converter shown in Figure 2 operates in a step-up or step-down mode, relative to the instantaneous AC input voltage, as shown in Figure 3.

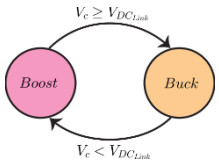

Fig.3. Operation modes.

In step-up operation, switches Q3 and Q4 switch at high frequency, while in step-down mode, switches Q1 and Q2 do so like depicted in Table 1.

	Step-Up		Step-Down	
	ON	OFF	ON	OFF
Q_1	1	1	1	0
Q_2	0	0	0	1
Q_3	1	0	0	0
Q_4	0	1	1	1

Table1. Switching Policy.

The inductor current does not coincide with the input port current in step-down mode, which can be translated into the necessity of adding an input filter to meet harmonic distortion standards and proper power factor correction. For this reason, a second-order passive filter with R-L damping is incorporated to mitigate this issue, optimizing the output impedance for stability following Middlebrook's criterion. A simplified model of the filter is presented for analysis around the equilibrium point.

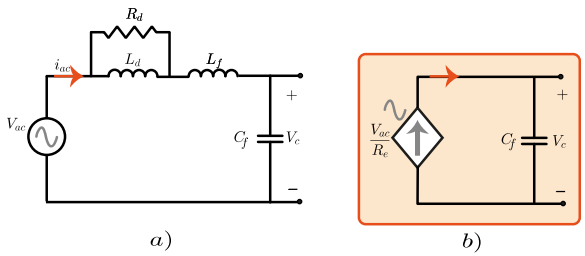

Fig.4. a) Second-order filter with damping L_d-R_d series. b) Simplified model at the equilibrium point.

3. System Control

A discrete control design is proposed for implementation in a single computing system, following the control diagram of Figure 5. The converter will act as a power factor corrector under a control law based on sliding mode dynamics (SMC), which forces the converter to behave as a loss-free resistor (LFR) in boost mode [5] and emulates that behavior in step-down mode following the current reference (equation 2) in the control law shown in equation 1. Specifically, a discrete sliding mode control (DSMC) is presented at a fixed switching frequency, which derived equivalent control can be seen in equation 3.

$$s(n) = I_{ref}(n) - i_L(n) \tag{1}$$

$$I_{ref}(n) = \begin{cases} \frac{|v_c(n)|}{R_e}, & step-up \\ \frac{|v_c(n)|^2}{R_e v_{bat}}, & step-down \end{cases} \tag{2}$$

$$d_{eq}(n) = \begin{cases} \frac{L\left(\frac{|v_c(n)|}{R_e} - i_L(n)\right)}{T_s v_{bat}} + \frac{v_{bat} - |v_c(n)|}{v_{bat}}, & step-up \\ \frac{L\left(\frac{|v_c(n)|^2}{R_e v_{bat}} - i_L(n)\right) + v_{bat} T_s}{T_s |v_c(n)|}, & step-down \end{cases} \tag{3}$$

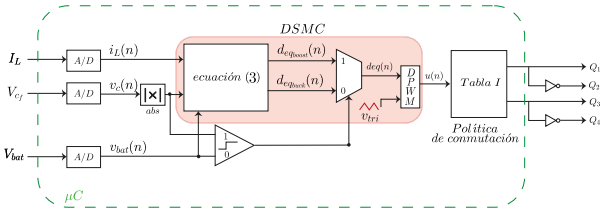

Fig 5. Control diagram.

4. Stability Analysis

In step-up operation, the reference current to be imposed depends on the square of the voltage across the input capacitor C_f. In this situation, simulations have shown that the capacitor design is a critical aspect of the proposal.

By using a small-signal model and applying the Jury criterion, the following constraint on the design of the input capacitor was obtained.

$$C_f \geq \frac{2LV_{ac}^2}{R_e^2 V_{bat}^2} \tag{4}$$

5. Simulation Results

Figures 6 and 7 show the waveforms of the input currents and the inductor current of the buck-boost converter when injecting current into the battery and vice versa at different input/output voltages.

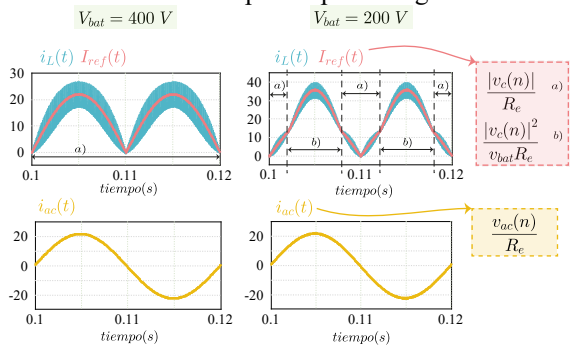

Fig.6. Vbat=450V and Vbat=200 V. Battery charging

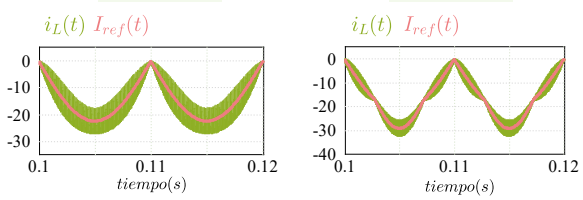

Fig.7. Vbat=450 V and Vbat=250 V. Grid injection.

6. Conclusions

In this study, a control strategy is proposed for a non-inverting buck-boost converter with an input filter aimed at power factor correction. The discrete control method, based on sliding mode control, effectively synthesizes a Loss-Free Resistor (LFR) behavior within the converter and input filter system. Specifically, in step-down mode, the modification of the inductor current reference establishes a proportional relationship between input voltage and current, thereby emulating LFR behavior and indirectly regulating input current.

Furthermore, a design condition has been established for the input filter capacitor, which voltage is a crucial state variable required for control, ensuring the stability of the system. The proposed control strategy is applicable for energy transfer in both directions, thus broadening the utility of the buck-boost converter for various applications, including power injection into the grid (V2G).

References

[1] ”MOVES III Plan”. Available Online: https://tinyurl.com/485mc4re

[2] ”Green Deal”. Available Online: https://tinyurl.com/2j57rxd6

[3] J. Yuan, L. Dorn-Gomba, A. D. Callegaro, J. Reimers and A. Emadi,”A Review of Bidirectional On-Board Chargers for Electric Vehicles,” in IEEE Access, vol. 9, pp. 51501-51518, 2021.

[4] H. Wouters and W. Martinez, ”Bidirectional Onboard Chargers for Electric Vehicles: State-of-the-Art and Future Trends,” in IEEE Transactions on Power Electronics, vol. 39, no. 1, pp. 693-716, Jan. 2024.

[5] A. Cid-Pastor, L. Martinez-Salamero, A. El Aroudi, R. Giral, J. Calvente, R. Leyva. Synthesis of loss-free resistors based on sliding-mode control and its applications in power processing, Control Engineering Practice, Volume 21, Issue 5, 2013,689-699.

PANI and Au-PANI dip coated films for electro-optical gas sensors

Z. Hamzei, S. Vallejos

Institute of Microelectronics of Barcelona (IMB-CNM, CSIC), Campus UAB, Barcelona

Abstract

PANI, known for its unique electrical and optical properties, was deposited on glass substrates using dip coating technique. Subsequently, Au NPs were synthesized via a chemical reduction method and then deposited on the PANI-coated glass substrates by dip coating the slides in the Au NP solution. UV-Vis confirmed the successful deposition of PANI nanoparticles and the formation of the PANI-Au NP composite by exhibiting characteristic peaks corresponding to PANI and Au NPs, as well as the combined absorption features of the PANI-Au NP composite. These results confirm the synthesis and deposition of the materials, laying the foundation for further investigations into its gas sensing performance for plant VOC detection.

1. Introduction

Polyaniline (PANI) is a conducting polymer that has attracted considerable interest because of its distinctive electrical and optical properties, including high conductivity, environmental stability, and ease of synthesis, making it suitable for various applications. Its conductivity and sensitivity can be finely adjusted through doping, and its ability to absorb and emit light across different wavelengths makes it ideal for optoelectronic devices [1]. Conversely, gold (Au) is renowned for its excellent electrical conductivity and optical properties, especially surface plasmon resonance (SPR), essential for applications needing precise detection and signal amplification [2]. Gold nanoparticles (NPs), in particular, have unique optical characteristics that, when combined with PANI, enhance the composite material's electrical and optical capabilities, making it highly effective for sensor applications. The combination of polyaniline (PANI) and Au NPs in gas sensors could offer a synergistic advantage by leveraging their distinct properties to enhance sensitivity and selectivity [3], particularly for detecting volatile organic compounds (VOCs) in agricultural settings. Various methods exist for synthesizing and depositing PANI and Au-PANI composites onto substrates, including chemical vapor deposition, electrochemical polymerization, and spin coating [4]. However, dip-coating emerges as a particularly advantageous technique due to its cost-effectiveness, scalability, and ability to produce uniform coatings. Dip-coating involves immersing a substrate into a solution of the desired material and then withdrawing it at a controlled speed, resulting in a uniform thin film [5] (Figure 1). In this context, the present work focuses on identifying the optimal conditions for integrating PANI and Au-PANI coatings on glass substrates as a first phase to subsequently evaluate their sensing properties upon exposure to representative VOCs from agriculture.

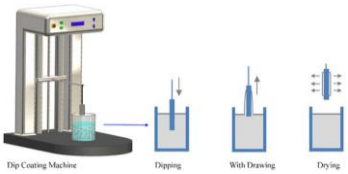

Figure 1. Scheme of the dip-coating method.

2. Experimental

The samples were coated on a glass substrate (1x1 cm) using a Dip Coater system. PANI was diluted in 1-Methyl-2-pyrrolidinone solvent and various concentrations were tested to optimize the coating process. UV-Vis spectroscopy was utilized to confirm the successful integration of PANI films and the formation of the Au-PANI composite. For this purpose, we used a UV-Vis spectrophotometer (AvaSpec) instrument. The spectra was acquired between 400 and 800 nm with a deuterium/halogen lamp. Au NPs were synthesized using $Na_3C_6H_5O_7.2H_2O$ and $HAuCl_4.3H_2O$. The formation of Au NPs was confirmed by UV-Vis spectroscopy. The absorption spectra displayed typical SPR peak at around 520 nm (Figure 2), consistent with the literature, which is result of the collective oscillation of conduction electrons within the Au NPs [10].

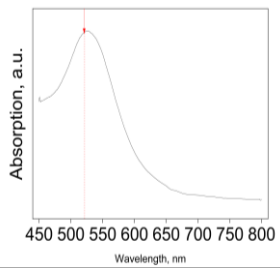

Figure 2. Absorption spectrum of the Au NPs synthesized by wet chemical method shows a SPR peak at 520 nm.

3.1. Dip coating of PANI and Au-PANI on glass substrates:

Several parameters, including the PANI solution concentration, withdrawal rate, and drying time, were optimized to obtain a well-adhered and homogeneous PANI coating. A concentration of 0.5 wt% in 1-methyl-2-Pyrrolidone was found to be optimal, as higher concentrations led to uneven coatings and lower concentrations resulted in incomplete coverage. The withdrawal speed of 2 mm/s was also identified as ideal, as slower speeds caused solvent evaporation and uneven coatings, while faster speeds led to incomplete wetting and poor adhesion [6]. The optimized dip-coating parameters for PANI deposition are shown in Table 1.

Table 1: Optimal conditions found for the dip coating of PANI on glass substrates.

Parameter	Optimal Value
PANI Solution Concentration	0.5 wt%
Withdrawal Speed	2 mm/s
Drying Time	5 minutes

The dip-coated PANI films showed uniform thickness and gray color across the glass substrates, as observed by both naked eye and optical microscopy. The homogeneity of the coating was further confirmed through optical microscopy at various magnifications, revealing no visible defects. Au NPs were deposited on the PANI films using a second dip-coating step with the same conditions used for PANI. After the this step the films displayed a homogeneous violet color.

3.2. UV-Vis Spectroscopy Analysis

Figure 3 shows the UV-Vis absorption spectra for each sample. The absorption spectrum of PANI in Figure 3(a) exhibits a broad absorption band at approximately 600 nm, attributed to the polaron-π* transition, which originates from the delocalized polaron states formed along the PANI chain. This absorption characteristic confirms that PANI was deposited on glass substrates. The absorption spectrum of the Au-PANI composite (Figure 3(b)) exhibits a combination of the absorption features from both PANI and Au NPs. The spectra shows PANI absorption bands at around 600 nm, while the Au SPR peak is observed between 500 and 550 nm [7,8]. The presence of these distinct absorption features indicates the incorporation of the Au NPs onto the PANI-coated glass substrates; further studies are under development to get better insight into the PANI and Au NPs interaction. Au-PANI composite is expected to enhance the material's conductivity and catalytic activity, potentially improving the sensitivity and selectivity of the gas sensor for plant VOCs. The Au NPs can act as electron storage reservoirs, facilitating charge transfer processes and improving the electrical conductivity of the composite material. Additionally, the catalytic properties of Au NPs can promote the adsorption and dissociation of analyte molecules, thereby enhancing the sensor's response and selectivity.

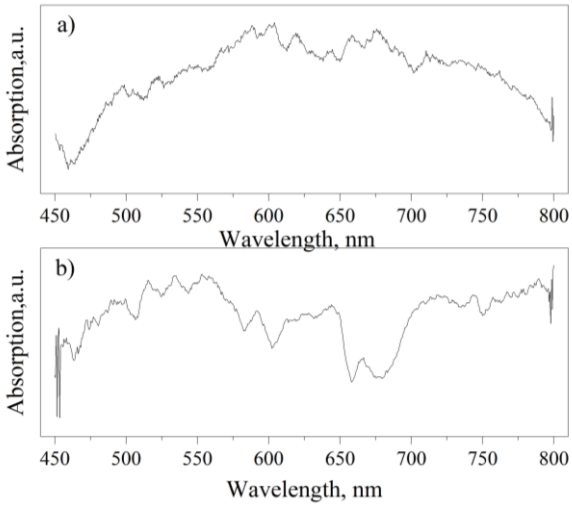

Figure 3: Absorption spectrum of PANI(a) and Au-PANI(b).

Conclusion

Uniform and continuous PANI and PANI-AuNPs were deposited on glass substrates using a dip coating technique. Au NPs were synthesized using a chemical reduction method, and their deposition on the PANI-coated glass substrates was confirmed through UV-Vis spectroscopy. The composite material's spectrum indicates characteristic absorption features of both PANI and Au-PANI, confirming the formation of the composite. Incorporating Au NPs into the PANI matrix is expected to enhance the material's conductivity and catalytic activity, potentially improving its sensitivity and selectivity towards plant VOCs, which is part of our future work.

Reference:

1. Beygisangchin, M., Abdul Rashid, S., Shafie, S., Sadrolhosseini, A. R., & Lim, H. N. (2021). Preparations, properties, and applications of polyaniline and polyaniline thin films—A review. Polymers, 13(12), 2003.

2. Janovák, L., & Dékány, I. (2010). Optical properties and electric conductivity of gold nanoparticle-containing, hydrogel-based thin layer composite films obtained by photopolymerization. Applied surface science, 256(9), 2809-2817

3. Venditti, I., Fratoddi, I., Russo, M. V., & Bearzotti, A. (2013). A nanostructured composite based on polyaniline and gold nanoparticles: synthesis and gas sensing properties. Nanotechnology, 24(15), 155503.

4. Yan, Y., Yang, G., Xu, J. L., Zhang, M., Kuo, C. C., & Wang, S. D. (2020). Conducting polymer-inorganic nanocomposite-based gas sensors: a review. Science and Technology of Advanced Materials, 21(1), 768-786.

5. Butt, M. A. (2022). Thin-film coating methods: A successful marriage of high-quality and cost-effectiveness—A brief exploration. Coatings, 12(8), 1115

6. Samat, S. F. A., Sarah, M. S. P., Idros, M., & Rusop, M. (2018, May). Optimizing the withdrawal speed using dip coating for optical sensor. In AIP Conference Proceedings (Vol. 1963, No. 1). AIP Publishing.

7. Rohom, A. B., Londhe, P. U., & Chaure, N. B. (2016). Enhancement of optical absorption by incorporation of plasmonic nanoparticles in PANI films. Nanosci Nanotechnol, 6, 83-87.

8. Anand, P. B., Hasna, K., Anilkumar, K. M., & Jayalekshmi, S. (2012). On the structural and optical properties of gold–polyaniline nanocomposite synthesized via a novel route. Polymer international, 61(12), 1733-17

Improved Physics-Based Model for Organic Thin Film Transistors:

Accurate Modelling and Parameter Extraction Method

Amer Zaibi, Benjamin Iñiguez

University of Rovira I Virgili Tarragona, Spain, DEEEA
amer.zaibi@urv.cat

Abstract

In this work, an improved physics-based model is utilized to replicate the behaviour of Organic Thin Film Transistors (OTFTs) using the Unified Modelling and Extraction Method (UMEM).

Hysteresis effects, current-voltage behaviour and transconductance are accurately captured, demonstrating strong agreement with experimental measurements.

Proficiency in simulating basic electronic systems like inverters is also demonstrated by our model. The model's advanced ability to capture hysteresis and transistor performance makes it valuable for circuit designers and researchers in organic electronics, with potential applications in complex electronic systems.

.

1. Introduction

Organic Thin Film Transistors (OTFTs) are gaining attention in organic electronics due to their potential applications in flexible displays, sensors, and low-cost electronics [1,2,3].

Compact models are essential for designing and simulating circuits using targeted technology. Organic-TFT models often include two independent equations for above-threshold and subthreshold regimes, while others use multiple empirical models to explain OTFT behaviour. However, these models may not fully capture underlying physics, leading to convergence problems in circuit simulation.

Our analysis and model are applied to two OTFTs in the low voltage regime with different dimensions (one long and one short channel lengths).

2. Methods

Description: Employed the UMEM [4,5] model to facilitate parameter extraction for implementation in both transfer and output characteristics of 2 OTFTs: L=5um (OTFT_1) and 200um (OTFT_2).

Implementation: Applied the UMEM to capture the hysteresis effects, current-voltage characteristics, and transconductance of OTFTs.

Validation: Compared the model's output against experimental data to verify its accuracy.

Inverter Simulation: Basic Electronic Systems: Demonstrated the model's proficiency by simulating basic electronic systems such as load resistive and capacitive inverter.

3. Results and Discussion

Figures 1 and 2 show the transfer characteristics of OTFT_1 and OTFT_2 respectively in the forward sweep from (0.5 V to -5V) and in backward sweep (-5V to 0.5 V). Good agreement is found between the model and experimental data for both devices.

Figure 3 shows the transconductance behavior with respect to Vgs. the model reproduces reasonably well the transconductance: a good transistor model to be used in circuit simulations must predict the transconductance correctly.

Figures 4 and 5 show our model accurately simulates the behaviour of an inverter.

Figures 6 and 7 show the output characteristics of OTFT_1 and OTFT_2. Good agreement is found between the model and experimental data for both devices.

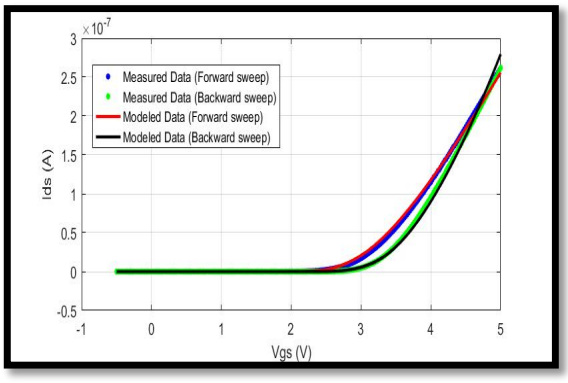

Fig.1. Transfer characteristics (forward and backward sweeps) OTFT, L=05um, W=1000um

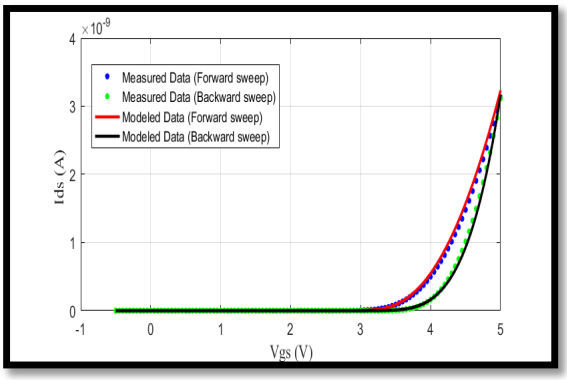

Fig.2. Transfer characteristics (forward and backward sweeps) OTFT, L=200um, W=1000um

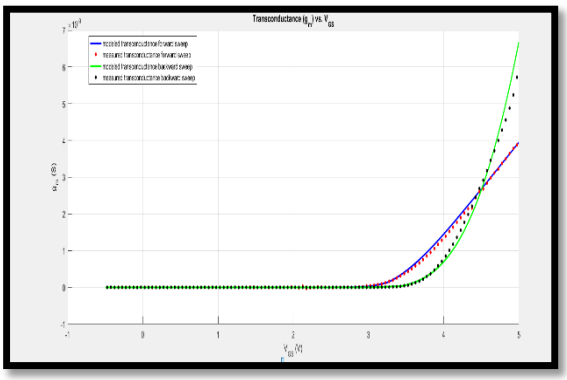

Fig.3. Dependence of the transconductance *gm* on the gate voltage (forward and backward sweeps OTFT 200um).

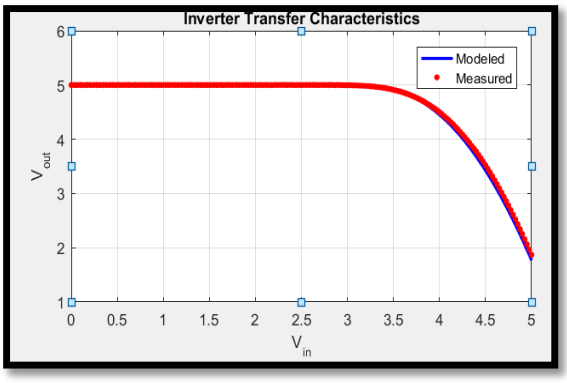

Fig.4. Inverter transfer characteristics using OTFT 200um.

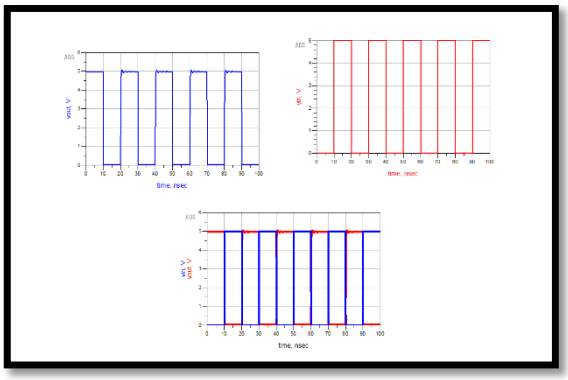

Fig.5. Transient response of the inverter

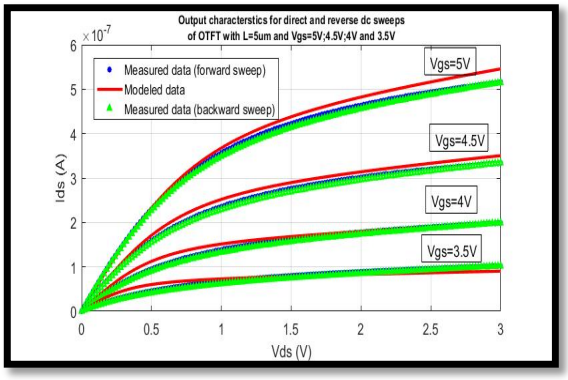

Fig.6. Output characteristics (forward and backward sweeps) OTFT 05um.

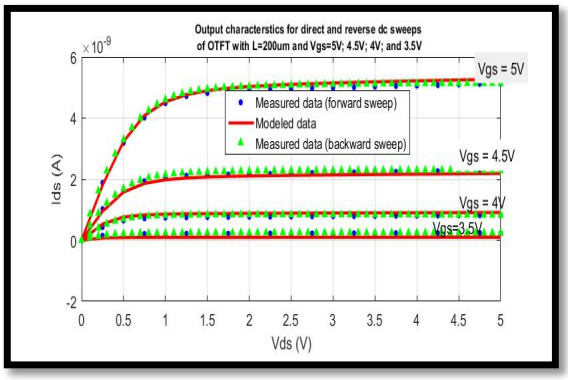

Fig.7. Output characteristics (forward and backward sweeps) OTFT 200um.

In both devices, we can notice that the Vthreshold shifts to more negative values between the forward and backward sweeps and the drain current Ids decreases during the backward sweep.

We found that only two parameters are significantly affected by hysteresis; the threshold voltage and the disorder parameter, which is related to the characteristic temperature of the DOS.

Following these analyses, the existence of the hysteresis effect can be confirmed. this type of hysteresis may result from one of two possible mechanisms or from

both.
Charge Trapping and Detrapping: Trapping/Detrapping times are different and can lead to Hysteresis.

Table1: Extracted parameters using UMEM for OTFT 200um.

UMEM Parameters	OTFT (Forward Sweep)	OTFT (Backward Sweep)
V_{T} [V]	-2.8	-2.95
γ_{a}	1.35	2.5
α_{Sat}	0.32	0.105
μ_{FET0} [cm2/V s]	9.6e-6	9.9e-6
S(V/dec)	0.24	0.24
m	2.7	2.7
$I_0(A)$	3e-13	3e-13

Mobile ions migration: The delayed response of ion migration relative to the sweep direction can lead to hysteresis.

4. Conclusions

The improved physics-based model using the Unified Modelling and Extraction Method (UMEM) successfully replicates the behaviour of Organic Thin Film Transistors (OTFTs) with high accuracy. By capturing hysteresis effects, current-voltage behaviour, and transconductance, the model shows strong agreement with experimental data.

This proficiency extends to simulating basic electronic systems like inverters, underscoring the model's advanced capability. The results highlight the model's significant value for circuit designers and researchers, facilitating the development of complex electronic systems in the field of organic electronics.

.

References

[1] Sharma, A., Madhu, C., & Singh, J. (2014). Performance evaluation of thin film transistors: history, technology development and comparison: a review. Int. J. Comput. Appl, 89(15), 36-40.

[2] Wang, Y., Cheng, S., Sun, C., & Wang, T. (2023). Organic Thin Film Transistor for Effective Biomarker Detection in Early Disease Diagnosis. Chemosensors, 11(3), 202.

[3] Jakher, S., & Yadav, R. (2024). Organic thin film transistor review based on their structures, materials, performance parameters, operating principle, and applications. Microelectronic Engineering, 112193.

[4] Iniguez, B., Nathan, A., Kloes, A., Bonnassieux, Y., Romanjek, K., Charbonneau, M., ... & Nejim, A. (2021). New compact modeling solutions for organic and amorphous oxide TFTs. IEEE Journal of the Electron Devices Society, 9, 911-932.

[5] Estrada, M., Cerdeira, A., Puigdollers, J., Reséndiz, L., Pallares, J., Marsal, L. F., ... & Iñiguez, B. (2005). Accurate modeling and parameter extraction method for organic TFTs. Solid-state electronics, 49(6), 1009-1016.

Algorithm for the Automatization of the Parameter Extraction Method by Mathematical Optimization

Dante Ángel Gómez Nápoles [a], Benjamin Iñiguez Nicolau [b], Antonio Cerdeira Altuzarra [a].
[a] Center of Research and Advanced Studies at IPN, Mexico City (dante.gomez.n@cinvestav.mx, cerdeira@cinvestav.mx)
[b] Department of Electronic and Electric Engineering and Automatic, University Rovira I Virgili, Tarragona, Spain, (a.mounir90@gmail.com, benjamin.iniguez@urv.cat)

Abstract

The implementation of a method for the extraction of modelling parameters, using mathematical optimization is implemented and analysed.
The objective of the work was to develop an algorithm which uses an iterative process to actualize input parameters, using the results of the previous optimization process, avoiding local minimums and improving the probability of finding a global minimum
A Graphic User Interface (GUI) was implemented in MATLAB, since it makes it easier the optimization process, by affording an intuitive surrounding, in addition to incorporate a great amount of programming and advanced optimization tools.
Results obtained confirm that the use of this algorithm guarantees that each iteration in the optimization process, uses the best-found solution, helping to reduce, progressively, the error and obtaining a more precise solution.

1. Introduction

In industry, as well as in research centres in the semiconductor field, obtaining a precise and detailed parameters that describe the device model is of great importance. This information is crucial for device fabrication installations, since it allows to realise circuit simulation using the Simulation Program with Integrated Circuit Emphasis (SPICE) language. This tool is widely used to design and analyse complex electronic circuits before they are fabricated. The precision obtained in these simulations depends directly on the degree of precision with which model parameters are obtained.
This procedure becomes especially important for developing advanced circuits and optimize their performance [1]. The evaluation of the viability of the circuit being designed before it is fabricated is crucial to identify and correct potential problems, as well as allowing producers to reduce repetition and variations in the fabrication processes.

This work is focused in obtaining model parameters that tend to a global minimum. The mathematical optimization is fundamental in this context.

In optimization methods the term “restarting” refers to the practice of starting the optimization process from different initial positions, to avoid falling in local minimums and to improve the possibility of finding the global minimum. The restarting method can be implemented using the result of the previous optimization iteration as the starting point for the next interaction. This technique is especially useful in not convex optimization problems, where the objective function can have multiple local minimums.

2. Description of the Graphic User Interface (GUI) in MATLAB.

The parameter optimization interface was design to simplify the optimization process of the specific mathematical model parameters. This tool provides an accessible form for adjusting the parameters and improving the precision of the model.
Introduce a .txt file with the measured data of the electrical characteristics to be modelled.
The interface includes control buttons and input fields that allow the user to introduce the initial values, execute optimization process as well as the use of manual extraction procedures in UMEM, which are described below.
Input vector: Our GUI contains initial values for the following input parameters: V_{t}, γ, $\mu_{1,}$ $_{R,}$ α_s, λ**,** which can be modified if desired by the user, before starting the optimization process**. [See Fig. 1]**.

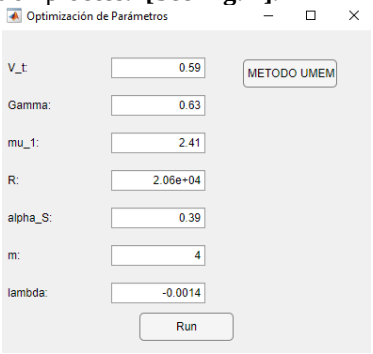

Fig.1. Principal Graphic User Interface (GUI) in MATLAB used for the automatization of the mathematical optimization method

To start the optimization process different approaches can be used.

I. Use of the "Pushed Button UMEM":

The optimization interface was designed to allow executing UMEM method using an additional GUI. This button allows the extraction of parameters V_t and γ. in a manual way.

In this case, a region where the integral function H1(n1) is valid, must be define, by setting values to V_{gsmax} and V_{gsmin} [2]. In this additional GUI, **[see Fig. 2]**, it is possible to visualize measured and interpolated characteristics as well as functions H1(n1) and HH1(n1), When button "Actualize and Close" is pressed, values V_t and γ are actualized at the GUI.

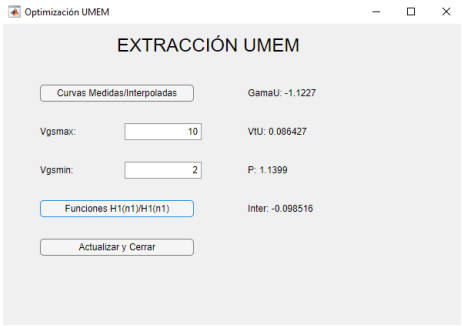

Fig.2. Secondary Graphic User Interface (GUI) in MATLAB for extraction process in UMEM

II. Use of the "Execution run Button":

When this button is pressed, the optimization process starts, using the values of parameters introduced in the input fields. A series of iterations are executed to adjust the values for the model parameters.

3. Execution of the optimization program.

Initialization of the optimization program:

Press button "Run" to store input vectors introduces at the GUI.

Configuration of the optimization conditions:

Function "lsqnonlin" is configured by the Levenberg-Marquardt algorithm. The convergence is the error allowed for the objective function, so an initial convergence value of tolerance, as well as a reduction factor of this value, must be set to adjust the precision of each iteration.

Automatic optimization iteration:

In each interaction, parameters are adjusted to minimize the convergence tolerance of the objective function, which is reduced progressively until a maximum number of iterations of after reaching a designed limit value.

If tolerance is not reached or the objective function does not converge, the program displays the parameters of the previous iteration.

Visualization of results:

During each iteration, optimization results are plotted automatically, this graphics compare measured with optimized data, showing the linear and saturation transfer curves, as well as the output characteristics.

4. Extraction procedure

To validate the developed algorithm and procedure, we applied it to model the electrical characteristics of a fabricated AOSTFT.

1) Execute the MATLAB program to obtain parameters V_t y γ **[Fig.2].**
2) Introduce in GUI the rest of required parameters **[Fig.1].**
3) Start executing interactions to obtain output parameters.

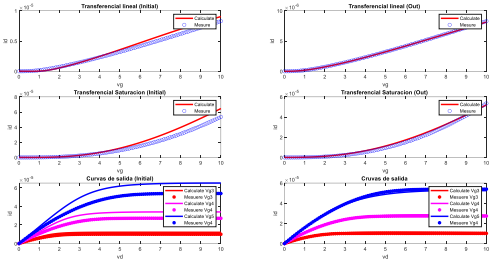

Fig.3. Comparison of modelled and measured characteristics

In this example the good coincidence is observed between measured and modelled characteristics, using an automated process for the extraction of the model parameters.

5. Conclusions.

The development of the optimization interface for parameter extraction through the implementation of iterative refreshing signifies that the extraction method can be performed automatically. This tool not only automates the parameter adjustment process but also ensures greater accuracy and efficiency in obtaining results. The capability of this method can be adapted to various applications in parameter optimization for different types of semiconductor devices because it focuses on increasing the probability of finding a global minimum by reducing the allowed error.

References

[1] Yiming Li and Yen-Yu Cho, "Parallel genetic algorithm for SPICE model parameter extraction," in *Proceedings 20th IEEE International Parallel & Distributed Processing Symposium*, Rhodes Island, Greece: IEEE, 2006, p. 8 pp. doi: 10.1109/IPDPS.2006.1639609.

[2] A. Cerdeira, M. Estrada, R. García, A. Ortiz-Conde, and F. J. García Sánchez, "New procedure for the extraction of basic a-Si:H TFT model parameters in the linear and saturation regions," *Solid-State Electron.*, vol. 45, no. 7, pp. 1077–1080, Jul. 2001, doi: 10.1016/S0038-1101(01)00143-5.

Enhanced Pseudocapacitive Behaviour of Porous Anodic Alumina Templated Ni-Nanorod Electrodes

Tabish Aftab, Josep Ferré i Borrull, Lluis F. Marsal*

Eng. Electrònica, Elèctrica i Automàtica, Universitat Rovira i Virgili, Paisos Catalans – 26, Tarragona–43007, Spain

tabish.aftab@urv.cat, josep.ferre@urv.cat, *lluis.marsal@urv.cat

Abstract

In this study, We present the fabrication of nickel nanorods using an electropulsed deposition method with nanoporous anodic alumina (NAA) templates, aiming to enhance low-cost, high-performance electrochemical energy storage. NAA membranes were prepared via a 2-step electrochemical anodization method using oxalic acid as electrolyte. Nickel deposition was achieved using pulsed current in a Watts Bath solution. SEM images confirmed the formation of nickel nanorods within the NAA pores (Ni@NAA). Cyclic voltammetry revealed promising pseudocapacitive behavior, with a specific capacity of 102 $F.cm^{-2}$ and retention of 82% after 1000 cycles.

1. Introduction

Nanostructured electrode materials with its unique structural features and increased electrochemical properties have the great potential for revolutionizing energy conversion and storage technologies. Nanostructures with distinct characteristics such as porosity, hierarchy and hollowness are extensively studied for their superior properties of providing high surface area, in many applications such as energy storage and conversion, water treatment, sensors, and catalysts [1,2]. Their exceptional qualities particularly in energy storage devices such as batteries and supercapacitors, are primarily attributed to their large surface area and empty spaces. Supercapacitors (SC's) possess several advantages over batteries, including a prolonged cycling life, a large capacity for providing power, and an environmentally friendly nature.

Pseudocapacitors are a kind of SC's that store charge through oxidation and reduction reactions occurring at the surface of the electrodes. Their pseudocapacitance is a result of the rapid faradaic redox reaction [3]. In contrast, conventional supercapacitors store charge through formation of electrical double layer at the surface. The electrode material plays an important role in energy storage applications and significantly influences the performance of the device. This work provides a comprehensive investigation of the synthesis, characterization, and electrical properties of nickel nanorod electrodes using nanoporous anodic alumina as templates for potential use in pseudocapacitor applications. The template-based synthesis approach allows for precise control over the morphology and structure, which is used to customize the electrochemical performance of the resultant electrodes.

2. Experimental description.

Nanoporous anodic alumina (NAA) was fabricated by using the well-known two-step anodization technique using 0.3 M oxalic acid solution at 40 V and at 5 ºC of electrolyte temperature. To electrochemically deposit nickel, it is necessary to remove the insulating barrier layer that remains between the pores and the base aluminum after the porous material production. This barrier layer hinders the flow of current during the electrodeposition process. The step-down voltage technique was used to reduce the thickness of the barrier layer, and the remaining barrier layer was dissolved by submerging the sample in a 5 wt% phosphoric acid solution. The pulsed electrodeposition technique was employed to deposit nickel into nanopores of alumina using watts bath solution consisting of 30 g of nickel sulphate, 4.5 g of nickel chloride, and 4.5 g of boric acid dissolved in 300 ml of deionised water [4]. The experimental setup involved utilizing the NAA as the anode and platinum as counter electrode. In this technique, the current was applied in the form of constant current pulses which allows the reduction of Ni-ions and their deposition at the bottom of the pores [5]. The nickel deposited sample was immersed once again in a 5 wt% phosphoric acid solution to partially etch the walls of the pores, hence increasing the active surface area for the reaction of electrolyte ions at the nickel nanorods.

3. Result and Discussion

The SEM characterization demonstrates the successful fabrication of nickel nanorods that are almost homogeneous in size and have well-defined dimensions and aspect ratios. Figure 1a shows the top-view of nickel deposited substrate and Fig.1b shows cross-sectional image which confirms the electrical path of Ni nanorods to the aluminium base. The estimated

dimensions of these nanorods are around 65-70 nm in diameter and 2 microns in length.

In addition, the electrochemical characteristics of the nanostructured nickel nanorod electrodes were thoroughly examined using cyclic voltammetry (CV) measurements. These measurements were conducted with respect to the Ag/AgCl reference electrode and platinum as counter electrode in an electrolytic solution of 1 M KOH. The potential range is set between 0-0.8 V, and the scan rate is 50 mV/s. The fabricated electrodes exhibit notable electrochemical performance due to their large surface area-to-volume ratio and effective charge transfer kinetics. CV of the Ni nanorods sample after 500th cycle is shown in Fig 2a. The curve shows well defined redox peaks that indicate better stability and reversibility. This highlights the enhanced electrochemical activity and durability of the nanostructured electrodes. These peaks correspond to the pseudocapacitance characteristics of the material and are distinct from the behavior of double layer capacitance. The formation of these peaks is a consequence of the oxidation and reduction reaction that occurs between the electrolyte and the active substance. The redox reaction occurring at the nanorods surfaces is:

$$Ni + 2OH\text{-} \leftrightarrow Ni(OH)_2 + e^{\text{-}}$$

The specific capacitance of the electrode was calculated to be approx. 102 F.cm^{-2}. Fig. 2b shows the plot of the specific capacitance as a function of the number of cycles. The plot shows the specific capacitance is reduced by only 18% after 1000 cycles., indicating a favorable retention capacity. It has also been noted that with increasing number of cycles the shape of the CV was not distorted, and it maintained the pseudocapacitive behaviour even after long number of cycles which is essential for long lifespan working of electrodes in energy storage devices applications.

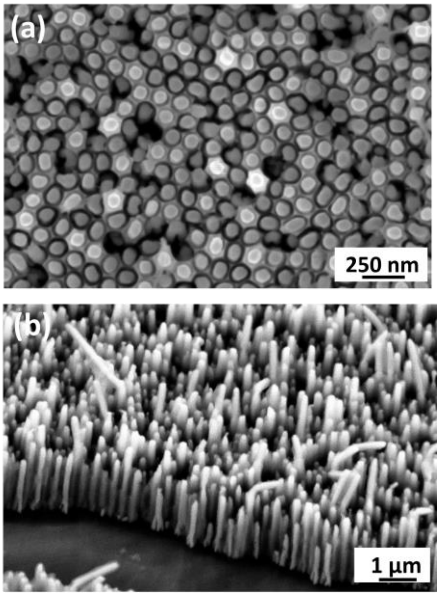

Figure 1. FESEM images (a) top view and (b) cross sectional view of nickel nanorods along with partially etched pore walls attached with the base aluminium.

7. Conclusions

In this study we have extensively investigated the impact of important factors such as effect of nanostructuring of metals, nanorod size, along with the electrochemical characteristics of Ni-nanorod electrode samples. The aim is to understand the fundamental mechanisms that control the performance of the nanostructured electrodes. The results highlight the importance of nanostructuring in improving the specific capacitance of the nickel-based electrodes for energy storage applications, indicating their potential for practical implementation in next-generation energy technologies.

References

[1] Sun Chang, Zhiyuan Han, Xia Wang, Bing Liu, Qiang Li, Hongsen Li, Jie Xu, Jun-Ming Cao, and Xing-Long Wu, Advanced Carbons Nanofibers-Based Electrodes for Flexible Energy Storage Devices. Advanced Functional Materials 33, no. 52 (2023): p. 2305606.

[2] Yu Zenan, Laurene Tetard, Lei Zhai, and Jayan Thomas, Supercapacitor electrode materials: nanostructures from 0 to 3 dimensions, Energy & Environmental Science 8, no. 3 (2015): p. 702-730.

[3] Chen Ri, Miao Yu, Rakesh P. Sahu, Ishwar K. Puri, Igor Zhitomirsky, The development of pseudocapacitor electrodes and devices with high active mass loading, Advanced Energy Materials 10, no. 20 (2020): p.1903848.

[4] Santos Abel, Lukas Vojkuvka, María Alba, Victor S. Balderrama, Josep Ferré-Borrull, Josep Pallares, and Lluís F. Marsal, Physica Status Solidi (a) 209, no. 10 (2012): p. 2045-2048.

[5] Nielsch Kornelius, Frank Müller, Li AP, and Ulrich Gösele, Advanced Materials 12, no. 8 (2000): p. 582-586.

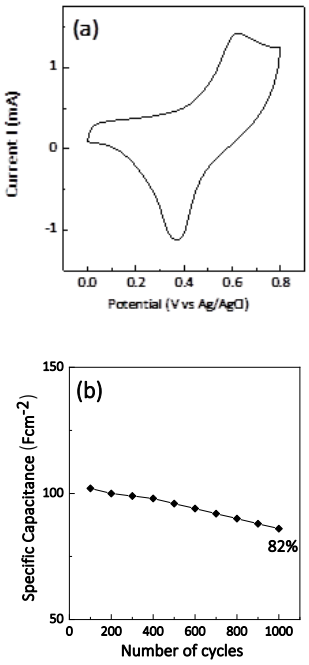

Figure 2. Cyclic voltammetry curves (a) CV at 500th cycle and (b) specific capacitance vs number of cycles graph stating the retention capacity, of Ni@AAO samples.

UV-light assisted hybrid InSe-Graphene gas sensor for the detection of NO_2

Jyayasi Sharma[1], Dalal Fadil[1*], Frank Güell[1,2], Eduard Llobet[1*]

[1]Universitat Rovira i Virgili, Microsystems Nanotechnologies for Chemical Analysis (MINOS), Tarragona, Catalunya, Spain
[2]Universitat de Barcelona, Catalan Photonics for Energy (ENFOCAT), Barcelona, Catalunya, Spain
*corresponding authors: dalal.fadil@urv.cat, eduard.llobet@urv.cat

Abstract

This work presents a novel light-modulated gas sensor based on hybrid InSe-Graphene synthesized via the liquid phase exfoliation (LPE) technique. We investigated the effects of temperature and UV-A light on the sensing layer. The morphology and electrical characteristics of the sensing surface are analysed using FESEM and AFM. The InSe-Graphene hybrid is exposed to three different light excitation wavelengths (375, 470, and 550 nm) as well as to dark conditions toward 1 ppm NO2 response. Results show that light excitation at room temperature and at an optimal temperature of 150℃ enhanced the sensor's responses.

Keywords— Liquid Phase Exfoliation (LPE); UV-A excitation; Gas sensor; hybrid InSe/Graphene

1. Introduction

Hazardous gases are constantly rising in the environment causing health and industrialization-related environmental damage [1]. Therefore, it is crucial to develop sensors for NO_2 detection. InSe has three polymorphs: ε, β, γ. When InSe is monolayer, its bandgap for the β polymorph increases significantly from about 1.28 eV to approximately 2.11 eV[2]. Graphene is another important 2D material that has sp2 hybridization. It possesses outstanding optical and electrical properties[3][4]. In this work, we present a hybrid InSe-Graphene gas sensor produced by LPE method[5] and characterized with FESEM and AFM techniques. Our sensor was tested at RT and optimal temperature in the dark and under three different light excitations.

2. Methodology

We utilized the LPE approach to create an InSe/Graphene hybrid sensor. We mixed 5 mg of InSe powder (99.995%, CAS#1312-42-1, Ossila) and 5 mg of Graphene nanoplatelets (CAS-1034343-98-0) in a solution of 2 propanol (IPA) (99.5%, Alfa Aesar) and DI water in a 3:7 ratio. The solution was then sonicated for 8 hours at 30℃ to exfoliate InSe/Graphene hybrid flakes. The exfoliated solution was subsequently centrifuged for 30 minutes at 1500 rpm to separate the exfoliated flakes from the precipitate and bulk, a process known as "Sedimentation-based Separation". The exfoliated flakes solution was then drop-casted onto commercially available alumina substrates with interdigitated electrodes on the front side with a 300-µm electrode gap and a platinum resistive meander on the back for temperature variation.

3. Results and Discussions

I. Surface Characterizations

The hybrid InSe-Graphene was prepared using the LPE approach, as described in the preparation process. FESEM analysis was performed to investigate the morphology of the bulk InSe and the hybrid InSe-Graphene sensor in its prepared state on an alumina substrate, as shown in Figure 1(a). The FESEM images revealed that the bulk InSe is properly stacked in multilayers, whereas the exfoliated hybrid InSe-graphene nanosheets are randomly dispersed on the electrode surface. The bulk material, with large sheets approximately in the micrometer range, has been transformed into nanometer-sized flakes. It is well known that exfoliated monolayers perform exceptionally well photoelectrically when layered randomly [6]. Figure 1(b) displays an AFM image of hybrid InSe-Graphene nanosheets on a silicon wafer, showing an average thickness of 1.79 ±1.1 µm. The image indicates the presence of multilayered stacks of exfoliated nanosheets. According to previous reports, InSe exhibits a direct bandgap structure when endowed with more than ~6-7 monolayers, which enhances light absorption and in turn increases the photoelectric response[7]

II. Sensing Results

We tested the hybrid InSe/Graphene sensor toward 1 ppm NO2 gas at RT (25℃) in the dark and under three different light excitation wavelengths (375 nm for UV-A excitation, 470 nm for blue excitation, and 550 nm for green excitation), as shown in figure 2(a). We observed a notable improvement in sensing response when exposed to UV-A light compared to dark conditions, blue and green lights. This enhancement can be attributed to UV-A radiation generating numerous electron-hole pairs under three different light excitations, with UV-A exposure showing the greatest

resistance drop. The photoexcited electrons may increase NO_2 adsorption, while the interaction of photoexcited holes with negatively charged NO_2 could facilitate desorption. This interaction may alter the material's electrical properties, rendering it more receptive to gas molecules[27]. Additionally, we assessed our sensor in the dark and during UV-A exposure at a moderate temperature of 150 ºC. Heating further enhanced the sensor's response, particularly when coupled with UV-A exposure. Thus, we investigated NO_2 at lower concentrations using UV-A excitation and temperature and the responses increased by almost 3 times for 1 ppm NO_2 gas, for the lower concentration of 100 ppb, the responses were nearly equivalent to the responses under dark conditions at RT. The temperature effect and UV-A excitation can be attributed to the increased rate of kinetic reaction on the sensor's surface.

CONCLUSION

A hybrid sensor based on InSe-Graphene has been developed. After testing the hybrid-based sensor at three different light excitation wavelengths, we found that the best response, 1.75% at RT, was obtained with UV-A excitation (375 nm), greater than the dark. We also investigated the 1 ppm NO2 response at an optimal temperature of 150℃ and with UV-A excitation. The responses nearly tripled, reaching 3.76% toward 1 ppm NO2. Therefore, it could be concluded that UV-A exposure enhances sensor responses and that the best responses occur when mild heating is combined with UV excitation.

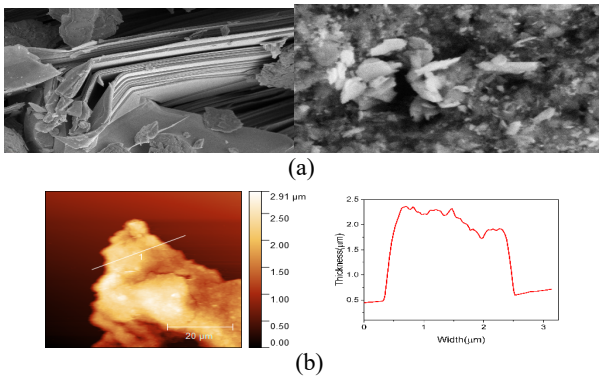

Fig. 1. (a) FESEM images of bulk InSe (left) and exfoliated hybrid InSe-Graphene (right) sensing layer (smaller flakes corresponding to Graphene and larger flakes corresponding to InSe) (b) AFM image of the sensing layer with associated height profile along the white line respectively.

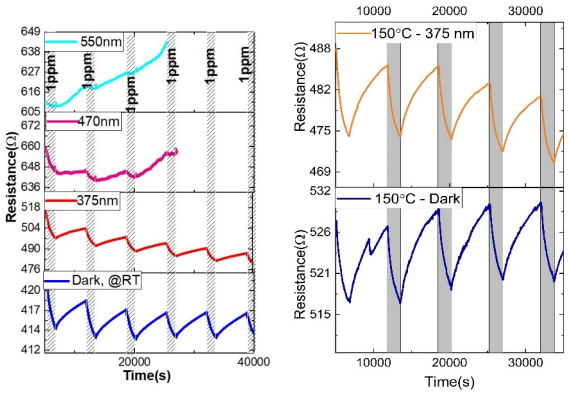

Fig. 2. Sensing results. (a) Comparison of sensor response towards 1 ppm NO_2 at RT in the dark and under three different excitations. (b). Dynamic resistance of InSe-Graphene hybrid at optimal temperature with and without UV-A light excitation for 1ppm NO_2

REFERENCES

1. R. M. Agus *et al.*, "Ambient air quality of SO2 and NO2 in settlements around industrial area of Makassar 2019," *Enferm. Clin.*, vol. 30, no. 2, pp. 328–332, 2020, doi: 10.1016/j.enfcli.2019.10.093.
2. N. Curreli *et al.*, "Liquid Phase Exfoliated Indium Selenide Based Highly Sensitive Photodetectors," *Adv. Funct. Mater.*, vol. 30, no. 13, 2020, doi: 10.1002/adfm.201908427.
3. S. V. Morozov *et al.*, "Giant intrinsic carrier mobilities in graphene and its bilayer," *Phys. Rev. Lett.*, vol. 100, no. 1, pp. 11–14, 2008, doi: 10.1103/PhysRevLett.100.016602.
4. J. Wang, J. Song, X. Mu, and M. Sun, "Optoelectronic and photoelectric properties and applications of graphene-based nanostructures," *Mater. Today, Phys.*, vol. 13, 2020, doi: 10.1016/j.mtphys.2020.100196.
5. D. Fadil, J. Sharma, M. I. Rizu, and E. Llobet, "Direct or Indirect Sonication in Ecofriendly MoS 2 Dispersion for NO 2 and NH 3 Gas-Sensing Applications," no. 2, 2024, doi: 10.1021/acsomega.4c03166.
6. Li *et al.*, "High-Performance Photo-Electrochemical Photodetector Based on Liquid-Exfoliated Few-Layered InSe Nanosheets with Enhanced Stability," *Adv. Funct. Mater.*, vol. 28, no. 16, pp. 1–7, 2018, doi: 10.1002/adfm.201705237.
7. M. J. Hamer *et al.*, "Indirect to direct gap crossover in two-dimensional InSe revealed by angle-resolved photoemission spectroscopy," *ACS Nano*, vol. 13, no. 2, pp. 2136–2142, 2019, doi: 10.1021/acsnano.8b08726.

Synthesis and study of a sulphur by selenium substitution in a high voltage photosensitizer for Dye-Sensitized Solar Cells.

Laia Marín Moncusí[a,b], Carlos E. Puerto Galvis[a], Eugenia Martínez-Ferrero[a] and Emilio Palomares[a,c]

[a]Institute of Chemical Research of Catalonia (ICIQ), The Barcelona Institute of Science and Technology (BIST), Avinguda dels Països Catalans, 16, 43007, Tarragona, Spain
[b]Departament d'Enginyeria Electrònica, Elèctrica i Automàtica, Universitat Rovira i Virgili, Avinguda dels Països Catalans, 26, Tarragona, Spain
[c]ICREA, Passeig Lluís Companys 23, E08010 Barcelona, Spain

Abstract

A novel molecular photosensitizer analogous to MS5 was successfully synthesized in 7 steps. The sulphur atom of benzothidiazole was exchanged by selenium, driving the absorption spectra towards the red and decreasing the HOMO-LUMO bandgap. By the study of its properties, we determine the new sensitizer to be a promising candidate for its application in Dye-Sensitized Solar Cells, with potential for showing efficient charge transfer and higher photocurrent than MS5.

Introduction

Dye Sensitized Solar Cells (DSSCs) are strong contenders for being the next generation of photovoltaics with a strong presence in the market. Thanks to their excellent properties such as non-toxicity, transparency, easy and low-cost fabrication and their outstanding efficiency in low light conditions they attention has risen over the last years.[1]

A rational and careful design of the photosensitizers is essential to achieve high efficiencies since they are responsible for the amount of light absorbed and the charge transfer ability of the cell. Over time several types of dyes, from metalated porphyrins to organic molecules with different structures, have been tested.[2]

Organic photosensitizers are based on a donor (D), π-spacer (π), acceptor (A) architecture and their corresponding combinations.[3] Several groups have been tested for this purpose, with benzoic acid and the Hagfeldt donor being the most popular acceptor and donor groups respectively.[4,5] As for π-spacer groups, heterocycles such as thiophenes, benzothidiazole or quinoxaline are a frequent choice since they contribute the molecule with extra stability and efficiently modulate its optoelectronic properties.[6]

In 2021, Grätzel and co-workers reported a new photosensitizer, MS5, based on a D-π-A structure that achieved a photovoltage of 1.24 V using a copper electrolyte (Figure 1).[7] MS5, is based on a benzothidiazole core acting as a spacer between the Hagfeld donor and the benzoic acid. Benzothidiazole is an heterocyclic ring formed by a benzene and a 5-membered ring with N and S atoms. In other structures, some authors have studied the effect of changing the sulphur atom by selenium, a bigger, electron richer and more polarizable atom. According to the literature, the introduction of selenium into the sensitizer structure can improve the molar extinction coefficient as well as shift the absorption maxima towards the red, resulting in a better efficiency in the photovoltaic device.[8-10]

In this regard, we synthesize a new selenadiazole photosensitizer, called MSe5, using the Hagfeldt donor and the benzoic acid as acceptor group (Figure 1), with the aim of comparing its properties and photovoltaic performance with the high voltage dye MS5.

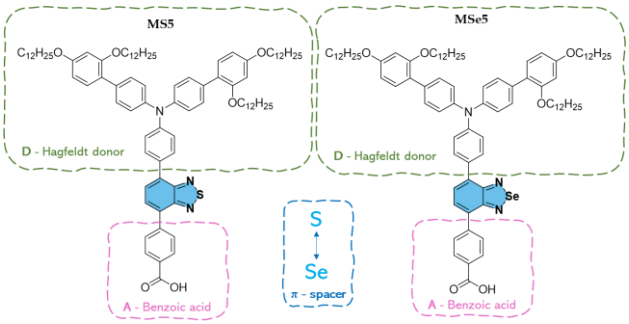

Figure 1. D-π-A structure of MS5 photosensitizer with its selenium analogue studied in this work, MSe5.

Results and discussion

For the synthesis of the molecule, a linear route of a total of 7 steps was designed (Figure 2). We envisaged the use of the Suzuki-Miyaura coupling to connect the donor and acceptor groups to the first synthesized selenadiazole core. The 4,7-dibromobenzothiadiazole **1**

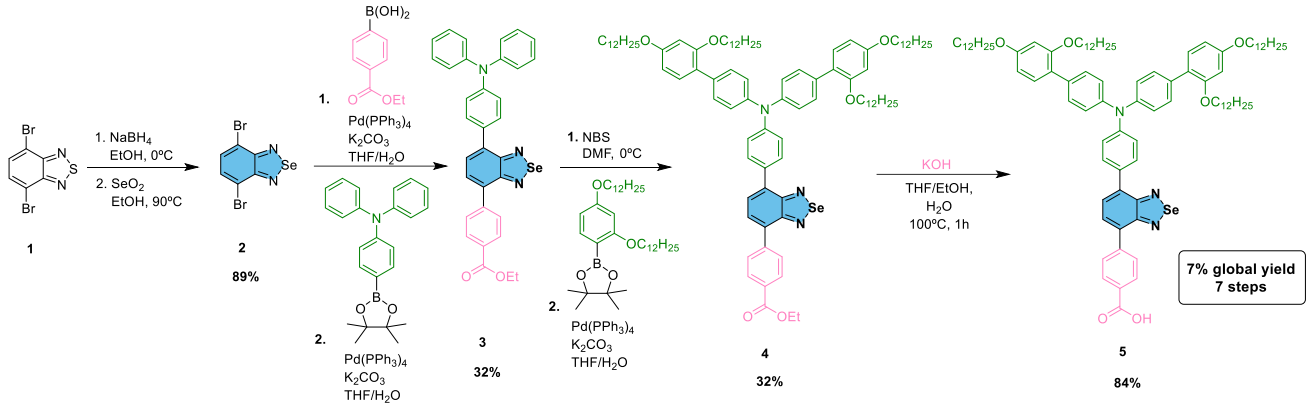

Figure 2. Synthetic route followed to obtain the target photosensitizer MSe5.

was selected as starting product to be reduced with $NaBH_4$ and obtain the doubly brominated cyclohexadiamine. Next, a cyclization with SeO_2 to obtain the selenadiazole ring was performed, obtaining **2** in 89% yield. The cores of the acceptor and donor groups into **2**, were introduced by two Suzuki-Miyaura couplings in the respective order achieving **3** in a total 32% yield. In the following step, the corresponding positions in the triphenylamine were brominated using an excess of NBS. Consequently, a new Suzuki-Miyaura coupling was done with the synthetic dioxaborolane thus completing the structure of the Hagfeldt donor and achieving **4**. Finally, a basic hydrolysis was done to obtain **5** with a 7% overall yield.

We then proceeded to the characterization of the sensitizer. Figure 3 shows the absorbance of MSe5 and MS5. As we expected, the absorption spectra of MSe5, is shifted to the red in comparison with MS5. Because of the larger atomic size of selenium, the energy band gap between molecular orbitals is decreased, shifting the maximum absorbance wavelength from 463 to 481 nm allowing a wider light absorption. We also performed cyclic voltammetry measurements of MSe5 adsorbed in TiO_2 to estimate the values of the HOMO-LUMO levels and determine if the dye could have an efficient charge transfer within the cell (Figure 3).

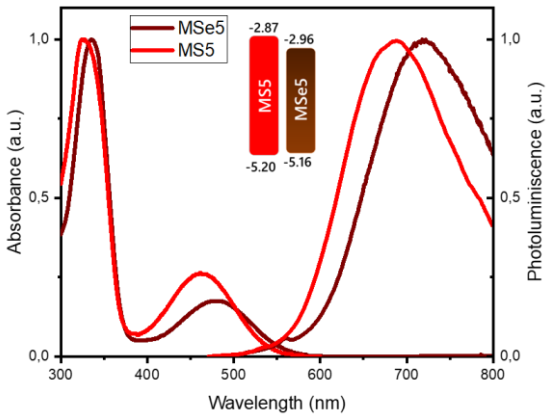

Figure 3. Normalized absorption and emission of MS5 and MSe5 and representation of HOMO-LUMO energy values.

The oxidation potential of MSe5, is more positive than the redox potential of the copper electrolyte, ensuring sufficient driving force for dye regeneration. On the second hand, the reduction potential is also more negative than the conduction band of the TiO_2, providing enough driving force for efficient electron injection.

Conclusions

We successfully synthesized a new molecular photosensitizer by following a linear route of 7 steps, relying on the Suzuki-Miyaura cross-coupling to connect the D and A moieties to the selenadiazole. Thanks to the introduction of the Se atom, we drove the absorption towards the red, making possible the light absorption of a wider range from the solar spectrum ideally resulting in higher photocurrent and efficiency in the future when DSSCs with this sensitizer are fabricated. On the second hand, the reduction of the HOMO-LUMO bandgap leaves room for the improvement in charge transfer in comparison to MS5, postulating the new photosensitizer as promising candidate for Dye-Sensitized Solar Cells.

References

[1] Kokkonen, M. et al; *J. Mater. Chem. A.*, **2021**, 9, 10527–10545.
[2] Ana Belén Muñoz-García et al., *Chem. Soc. Rev.*, **2021**, 50, 12450-12550.
[3] Jung-Min Ji et al., *J. Mater. Chem.* A, **2018**, 6, 14518–14545.
[4] Alexandra Baumann et al., *ChemSusChem*, **2020**, 13, 2503 – 2512.
[5] Lei Zhang and Jacqueline M. Cole; *ACS Appl. Mater. Interfaces* **2015**, 7, 3427−3455.
[6] Sumit Chaurasia and Jiann T. Lin; *Chem. Rec.*, **2016**, 16, 1311–1336.
[7] Zhang, D., et al., *Nat Commun*, **2021,** 12, 1777.
[8] Tamba, S.; Fujii, R.; Mori, A.; Hara, K.; Koumura, N.; *Chem. Lett.;* **2011**, 40, 922−924.
[9] Li, R.; Lv, X.; Shi, D.; Zhou, D.; Cheng, Y.; Zhang, G.; Wang, P.; *J. Phys. Chem. C;* **2009**, 113, 7469−7479.
[10] Palivela Siva Gangadhar et al; *ACS Appl. Energy Mater.*; **2024**, 7, 3309−3320.

Enhancing electrocatalytic CO_2 reduction through maximization of electroactive sites in a Cobalt phthalocyanine-based polymer

Joan Marc Bondia Pedra,[a,b] *Federico Franco,*[a]* *Emilio Palomares* [a,c]*

a Institute of Chemical Research of Catalonia (ICIQ), The Barcelona Institute of Science and Technology (BIST), Avinguda dels Països Catalans, 16, 43007, Tarragona, Spain
b Departament d'Enginyeria Electrònica, Elèctrica i Automàtica, Universitat Rovira i Virgili, Avinguda dels Països Catalans, 26, Tarragona, Spain
c ICREA, Passeig Lluís Companys 23, E08010 Barcelona, Spain

Abstract

The formation of metal-organic-based porous polymers has revealed to be an effective strategy to improve the overall electrocatalytic CO_2 reduction performances by preventing aggregation and maintaining accessibility of the active's sites. In this regard, here we synthetize a Cobalt (II)-phthalocyanine-based polymer by using the novel Cu(I)-catalyzed azide/alkyne cycloaddition reaction (CuAAC) strategy that ensures the formaton of pores and 1,2,3-triazole moieties. This system is able to enrich the microenvironment of the catalyst with CO_2 molecules and maximize the number of electroactive sites, thus improving the CO_2 reduction reaction.

1. Introduction

Polymeric frameworks composed of molecular complexes have been widely studied in catalysis due to their remarkable performance for the electrochemical reduction of CO_2, which includes high stability, selectivity and easy availability.[1] Yet, single-site metal-organic complexes, like Cobalt phthalocyanines (CoPc), are prone to aggregate leading to mass transfer limitations, thus reducing the number of actives sites and the overall performance in catalysis.[2] In this regard, phthalocyanine-based polymeric materials represent a promising approach towards maximizing electroactive sites since are effective and well-known substrates for the selective adsorption of CO_2 leading to abundant active sites due to their high surface area, porosity and chemical stability,[3-5] facilitating then the CO_2 reduction reaction (CO_2RR). One good example is the phthalocyanine polymer reported by Echegoyen et al. which is highly selective for CO_2 capture because of its porosity and affinity of CO_2 given by the nitrogen-rich functional groups (amine and triazole) inside the pores.[6] Another outstanding example is reported by Jiang et al. where a CoPc COFs, thanks to its 3D geometry, ensures about one-third of the total cobalt (II)-phthalocyanine subunits as electroactive sites, obtaining larger current densities.[7]

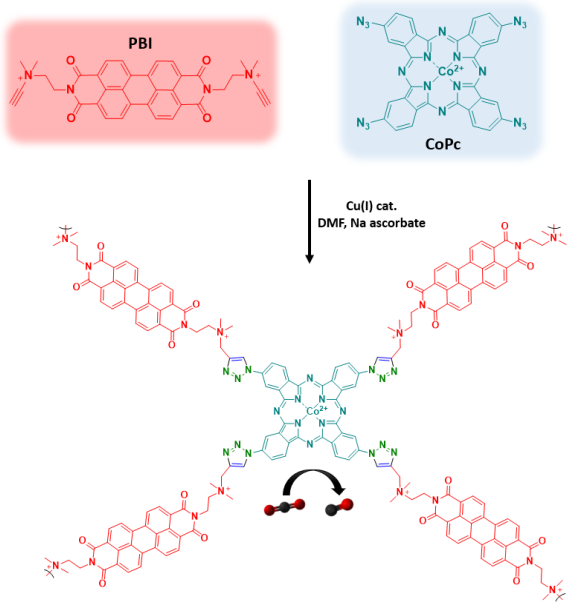

Scheme 1. Synthesis of CoPc-PBI

In this work, a porous Cobalt (II) phthalocyanine-based polymer is synthetized by following a Cu^I-catalyzed alkyne/azide cycloaddition (CuAAC) which has emerged as one of the most versatile synthetic transformations in organic chemistry, leading to the regioselective synthesis of several 1,4-disubstituted 1,2,3-triazoles.[8,9] This strategy permit to modulate the molecular environment of the system by introducing, for example, perylene bisimide (**PBI**) moieties that offer an improved ion transport,[10] that together with the formation of porous cavities with triazole moieties, the number of active sites could be maximized to improve the catalytic performance.

2. Results and discussion

The UV-Vis spectra (Figure 1a) in DMSO shows the

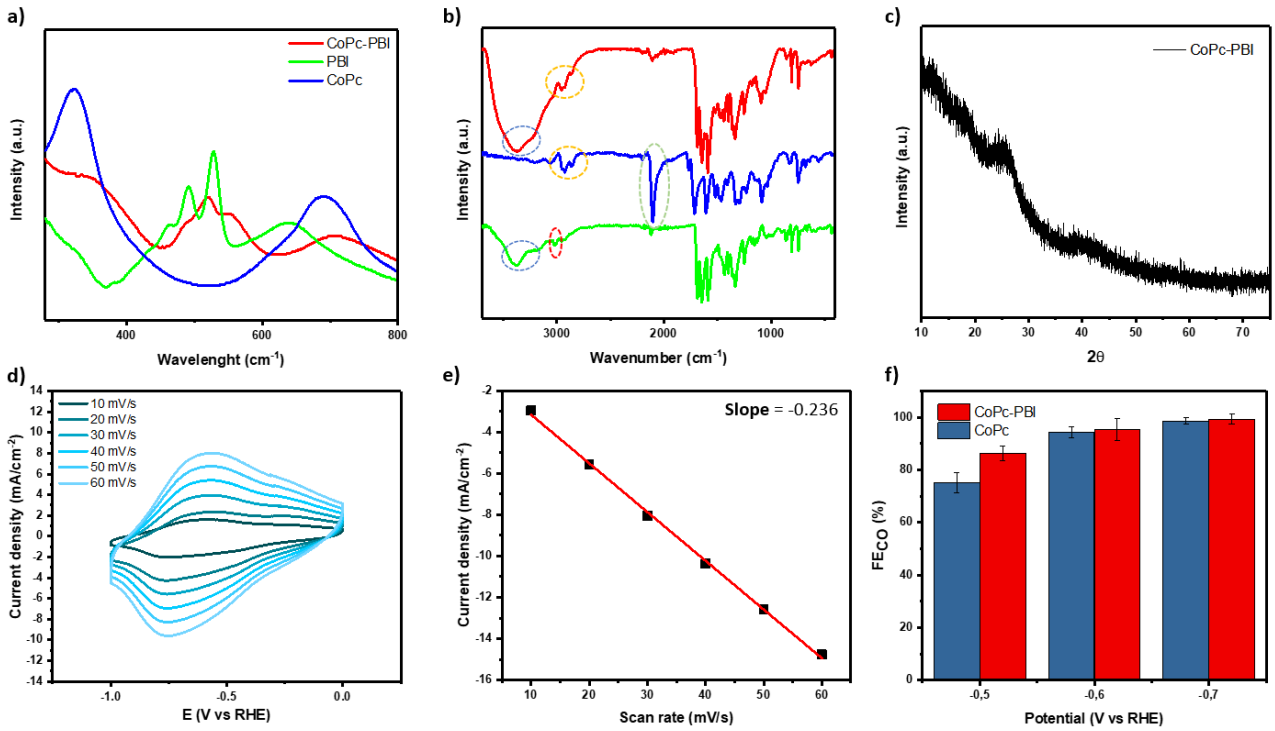

Figure 1. a) UV-Vis spectra of CoPc-PBI (red), PBI (green) and CoPc (blue). b) FTIR-ATR spectra of CoPc-PBI (red), PBI (green) and CoPc (blue). c) PXRD spectra of CoPc-PBI. d) Representative examples of cyclic voltammograms used to determine the slope of CoPc-PBI. e) Peak current of the cyclic voltammograms as a function of scan rate for CoPc-PBI. f) Gas phase FE comparison between CoPc-PBI (red) and bare CoPc (blue).

characteristic absorptions spanning at 300-400 nm and 650-750 nm wavelength range corresponding to the **CoPc** monomer (in blue). Furthermore, it also shows the sharped absorption band between 450-550 nm characteristic of perylene molecules corresponding to the **PBI** monomer (in green). The resulting polymer (**CoPc-PBI**, in red) presents the 3 absorption bands indicating the successful formation of the polymeric structure. The FTIR-ATR spectra manifest the absence of peaks at 2100 cm^{-1} and 3050 cm^{-1} for CoPc-PBI, that corresponds to terminal azide and alkyne groups, respectively, thus indicating the lack of residual monomer in the latter polymer. Furthermore, the broad band around 3300 cm^{-1} (in blue) and 2900 cm^{-1} indicates the presence of the bisimide and -C=CH- moieties, coming from **PBI** and **CoPc**, respectively. Finally, new stretches are observed at 1600 cm^{-1} for the -N=N- stretch, thus confirming the successful formation of the 1,2,3-triazole moieties. PXRD spectra confirms an amorphous character of the polymer, since no exogenous peaks are observed in the diffractogram (Figure 1c). To estimate the surface concentration of electroactive cobalt phthalocyanine units in CoPc-PBI, cyclic voltammetry tests of **CoPc-PBI** in Ar saturated 0.5M $KHCO_3$ on the scan rate between 10 to 60 mV/s were conducted (Figure 1d). The peak current shows a linear dependence on the scan rate (Figure 1e). Surprisingly, **CoPc-PBI** ensures the electrochemical surface concentration as high as 254 $nmol/cm^2$ on electrode acting as active centers.

The electrochemical measurements were carried out using a BioLogic potentiostat (SP-150) in a custom-made two-compartment H-type cell, in which the working and counter electrode were separated by an anion-exchange Selemion AMV membrane (AGC Engineering). The monomer (**CoPc**) used to synthetize the polymer (**CoPc-PBI**) was tested for the electrochemical reduction of CO_2 and compared with CoPc-PBI (Figure 1f). In both cases, at -0.7 V_{RHE}, the selectivity obtained is 100% towards the formation of CO. Nevertheless, at -0.5 V vs RHE, a small difference is observed, being 90% for **CoPc-PBI** and 71% for **CoPc**. This finding suggests that the onset potential for the reduction of CO_2 has shown a slight shift towards less negative potentials.

3. Conclusion

To sum up, porous polymeric Co-based phthalocyanine was synthetized through a Cu-catalyzed azide-alkyne cycloaddition (CuAAC) reaction ensuring the formation of 1,2,3-triazole moieties confirmed by UV-Vis and FTIR-ATR spectroscopy. The ECSA study reveals 254 $nmol/cm^2$ subunits of Co(II)-phthalocyanine as active electrocatalytic sites, resulting in a good CO_2RR performance obtaining almost a 100% FE_{CO} in a range of -0.7 to -0.9 V_{RHE}. We hypothesize that the increased affinity for CO_2 molecules given by triazole units, together with the easy accessibility to the metal centers through the pores, may be essential for preventing aggregation and maximizing the number of active sites.

References

[1] Jiang, D.; Bu, R.; Xia, W.; Hu, Y.; Zhou, M.; Gao, E.; Asahi, T.; Yamauchi, Y., Tang, J. *Materials Report: Energy*, **2023**, 100176.
[2] Chen, J.; Zhu, M.; Li, J.; Xu, J.; Han, Y-F. *J. Phys. Chem.*, **2020**, *124*, 16501-16507.
[3] Wang, H.; Wang, G.; Hu, L.; Ge, B.; Yu, X.; Deng, J. Materials, **2023**, *16*, 1630.
[4] Mukhtar, A.; Saqib, S.; Mellon, N.; Rafiq, S.; Babar, M.; Ullah, S.; Muhammad, N.; Laeeq, A.; Ayoub, M.; Ibrahim, M.; Maqsood, K.; Azami, M.; Al-Sehemi, A.; Klemes, J.J.; Asif, S.; Bokhari, A. *Journal of Cleaner Production*, **2020**, *277*, 123999.
[5] Bhanja, P.; Modak, A.; Bhaumik, A. *Chem. Cat. Chem.*, **2019**, *11*, 244-257.
[6] Pavan, V.; Wang, J.; Deng, S.; Echegoyen, L. *J. Mater. Chem.* A, **2015**, *3*, 10284.
[7] Han, B.; Jin, Y.; Chen, B.; Zhou, W.; Yu, B.; Wei, C.; Wang, H.; Wang, K.; Chen, Y.; Chen, B.; Jiang, J. *Angew. Chem. Int. Ed*. **2022**, *61*, e202114244
[8] Medal, M.; Tomoe, C.W. *Chem. Rev*. **2008**, *108*, 2952.
[9] Rostovtsec, V.V.; Green, L.G.; Fokin, V.V.; Sharpless, K.B. *Angew. Chemie. Int. Ed*., **2002**, *41*, 2596.
[10] Kim, C.; Bui, J.C.; Luo, X.; Cooper, J.K.; Kusoglu, A.; Weber, A.Z.; Bell, A.T. *Nature energy*, **2021**, *6*, 1026-1034.

TCAD modeling of Organic Electrochemical Transistors

Ermias T. Teka*[1], Yeohoon Yoon[2], Hans Kleemann[2], Ghader Darbandy[3], Benjamin Iniguez[1]

[1] Department of Electrical and Automatic Electronic Engineering, Universitat Rovira i Virgili, Tarragona, Spain
[2] Dresden Integrated Center for Applied Physics and Photonic Materials, TU Dresden, Dresden, Germany
[3] TH Mittelhessen University of Applied Sciences, 35390 Giessen, Germany
*(corresponding author ermiastelahun.teka@urv.cat)

Abstract

Organic Electronics have steadily been the focus of research for the past couple of decades, with the aim of replacing conventional inorganic electronics. An emerging field with many opportunities in bioelectronics applications, sensors and neuromorphic computing is the Organic Electrochemical Transistor (OECT). It is a 3-terminal device, with an organic mixed ionic-electronic conductor (OMIEC) as the channel and an electrolyte between the gate and the channel to regulate electron and ion transport. Appropriate Technology Computer Aided Design (TCAD) based models have yet been developed for OECTs. This work presents a TCAD model of an OECT developed using the software, Silvaco Atlas, with a good agreement to the experimental data of the steady-state transfer and output characteristics.

Keywords: Organic Electrochemical Transistor (OECT), Technology Computer Aided Design (TCAD), Organic mixed ionic-electronic conductor (OMIEC).

1. Introduction

Organic Electrochemical Transistors (OECTs) are organic transistors that have recently been proposed for many applications in the field of biosensors, neuromorphic computing, Lab-on-chip devices, logic circuits, smart textiles and electrochromic displays [1]. OECTS are a type of electrolyte-gated organic field effect transistors (EGOFET) with volumetric capacitance as doping changes occur over the entire channel volume rather than parallel plate capacitance, where doping occurs within a thin interfacial region at the semiconductor file/electrolyte interface [2]. A potential at the gate makes OECTs capable to simultaneously regulate electronic charge carriers (electrons and holes) and ionic ones (cations and anions) due to the ionic injection from the electrolyte into the channel and the proceeding dedoping-doping process [3]. Its reversibility, low energy requirement and high capacitance of the electrical double layer allows low voltage operations [4]. One of the most widely used OMIEC, PEDOT:PSS, a commercially available and stable p-type organic semiconductor, has been used for this work. The model developed in this work is using the TCAD software Silvaco ATLAS, a physically-based device simulator, that predicts the electrical characteristics that are associated with specified physical structures and bias conditions [5]. The modeled OECT was fabricated in TU Dresden with a channel length of 100µm, a channel width of 100µm, and an electrolyte thickness of 30µm. For the simulation, a gate thickness of 10um and a PEDOT:PSS thickness of 30µm was used.

2. Methods and models

To have a physically based TCAD model in Silvaco Atlas, the OECTs material and electrical properties were considered, the assumed doping, permittivity, bandgap, electron affinity, density of states of the electrolyte and other related properties. The capacitance of the electrical double layer can be modeled by adding a thin oxide layer (~1nm) at the interface of the electrolyte and the OMIEC (PEDOT: PSS), as shown in the figure below.

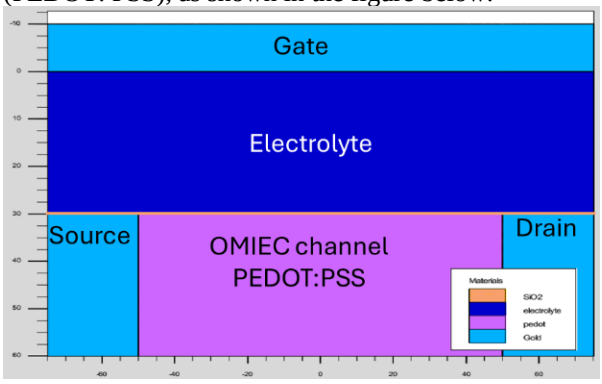

Fig.1: Structure of the simulated OECT (oxide layer not drawn to scale)

The Fermi-Dirac statistics and incomplete ionization models were also used for the ionic movement. Additional interface charges were also added on the oxide layer to model the effect of the electrical double layer and to change the value of the threshold voltage. For the PEDOT: PSS channel a gaussian Density of

states [5] was used as shown in the formula below.

$$g_c(E-E_C) = \frac{N_t}{\sqrt{2\pi}\sigma_{Gaus}} e^{\left(-\frac{(E-E_C)^2}{2\sigma_{Gaus}^2}\right)}$$

For the mobility of charge carriers in the channel, a square-root electric field dependent model, Poole-Frenkel mobility model [5] was used.

$$\mu_{pf}(E) = \mu_0 e^{\left(-\frac{\Delta_{pf}}{kT_{eff}} + \left(\frac{\beta_{pf}}{kT_{eff}} - \gamma_{pf}\right)\sqrt{|E|}\right)}$$

Organic defects models were also used from Silvaco library to model the tail-end exponential density of states (DOS) along with the gaussian. The parameters used are listed in the table below.

Parameter	Description	Value
N_C, N_V	DOS Electrolyte	~10^{32}cm^{-3}
ϵ_r	Electrolyte Relative Permittivity	80
$\mu_{0,\ elec}$	Ion Mobility	10^{-3}cm^2(Vs)$^{-1}$
$\mu_{0,\ OMIEC}$	OMIEC constant mobility	8cm^2(Vs)$^{-1}$
$\epsilon_{r,OMIEC}$	OMIEC Relative Permittivity	12
β	Poole-Frenkel coefficient	0.01
γ	Poole-Frenkel coefficient	0
Δ	Effective activation energy (Poole-Frenkel)	0.003
$N_{A,0}$	OMIEC p-doping density	10^{12}cm^{-3}
N_t	Number of hopping sites (for gaussian DOS)	10^{21}cm^{-3}
σ_{Gaus}	Width of the gaussian DOS	0.1665eV
E_C	Energy Center (for gaussian DOS)	0
$W_{F(S/D/G)}$	Source/Drain/Gate workfunction	4.85eV

Table1. Parameters used in the model.

3. Results

A static DC simulation was performed with the TCAD model and compared with the measured Transfer and Output Characteristics with relatively good agreements Both characteristic curves were measured to have hysteresis during the forward and backward sweeps.

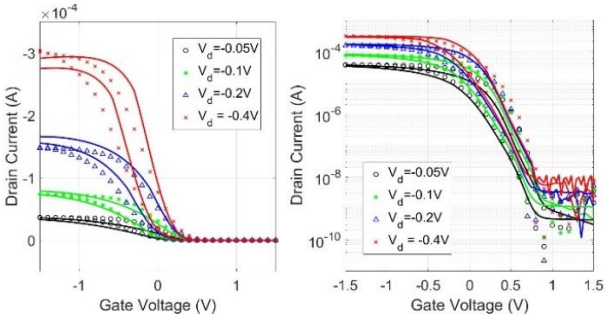

Fig.2: Comparison of transfer characteristics curves of measurements (symbol) and TCAD model simulation (solid lines) for linear and logarithmic scale

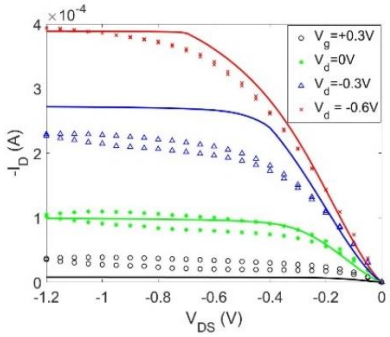

Fig.3: Comparison of output characteristics curves of measurements (symbol) and TCAD model simulation (solid lines) for linear scale

4. Conclusions

The model seems to have good agreement for the transfer characteristics than the output characteristics plots. This could be due to the hysteresis effect present in both measurements which prevents from having the same output current for the same bias conditions in the transfer and the output characteristics setup. This effect was difficult to model in TCAD. To simulate the hysteresis effect, different parameters were used implementing surface charge variations for the forward and the backward sweeps, i.e. having two different models for the forward and the reverse sweep separately. One way to avoid two different models is to have a singular model that runs in the transient simulation to depict the total effect of the hysteresis. Since TCAD doesn't have a model for a PEDOT:PSS device, a generic organic material was used and the electrochemical effect of the OECT also couldn't be fully shown. The thickness of the OMIEC also didn't have any effects on the simulation.

5. Acknowledgment

This work was funded by the European Union under contract 101099555 (BAYFLEX) and the Ministry of Science of Spain under contracts TED2021-130307B-I00 and PRX21/00726 with the support of the predoctoral program AGAUR-FI ajuts (2023 FI-1 01022) Joan Oro of the Secretariat of Universities and Research of the Department of Research and Universities of the Generalitat de Catalunya and the European Social Funds Plus.

References

The references below are written using Times 9 font. We suggest you do the same.

[1] J. Ajayan et. al, "Organic Electrochemical Transistors (OECTs): Advancements and Exciting Prospects for Future Biosensing Applications," IEEE Trans Electron Devices, vol. 70, no. 7, pp. 3401–3412, Jul. 2023,

[2] J. Tropp et. al, "Organic mixed conductors for electrochemical transistors," Matter, vol. 6, no. 10. Cell Press, pp. 3132–3164, Oct. 04, 2023.

[3] A. Marks et. al, "Organic Electrochemical Transistors: An Emerging Technology for Biosensing," Advanced Materials Interfaces, vol. 9, no. 6. John Wiley and Sons Inc, Feb. 01, 2022.

[4] A. Weissbach et. al, "Photopatternable solid electrolyte for integrable organic electrochemical transistors: Operation and hysteresis," J Mater Chem C Mater, vol. 10, no. 7, pp. 2656–2662, Feb. 2022

[5] "Atlas User Manual DEVICE SIMULATION SOFTWARE," 2022

Review of state of charge estimation methods for battery cells in electric vehicles

1st Miguel Antonio Pisani Orta; miguelantonio.pisani@urv.cat; Grup d'Automàtica i Electrònica Industrial, Universitat Rovira i Virgili
2nd Hugo Valderrama Blavi; hugo.valderrama@urv.cat; Grup d'Automàtica i Electrònica Industrial, Universitat Rovira i Virgili
3rd David García Elvira; david.garciae@urv.cat; Grup d'Automàtica i Electrònica Industrial, Universitat Rovira i Virgili

Abstract

Within the electric mobility framework, the accurate and continuous estimation of the state of charge (SoC) is fundamental to achieve high reliability and performance. In our work we analyzed and summarized the SoC estimation techniques employed nowadays in the electric vehicle technologies. Simple strategies like coulomb counting and lookup tables were revised initially. After that more complex algorithms were considered. Such algorithms encompass mathematical and data-driven models. Within the data driven models we dedicated special attention to neural networks and support vector machines. Finally, we concluded providing advantages and disadvantages of each method and explaining the future line of investigation to address the SoC estimation problem.

1. Introduction

The rapid advancements in the electric vehicle technologies have greatly influenced the investigation to be focused in the development of precise and reliable methods to estimate the state of charge (SoC) in electrochemical cells.

Electric vehicles constantly need to receive updates of the remaining energy in the battery pack, and the available power to not exceed the safety limits imposed by the manufacturer.

The energy and power are two variables that cannot be measured directly due to the fact there is no sensor capable of performing such task. Therefore, these two quantities should be estimated using voltage $v(t)$, current $i(t)$, and temperature $T(t)$, and the state of charge (SoC) $z(t)$.

The SoC represents the ampere-hours that can be extracted from the cell (Q_{rem}) as a percentage of the maximum available capacity (Q_{max}). Mathematically, $SoC = (Q_{rem}/Q_{max}) \cdot 100\%$.

Accurate SoC estimates not only provide information in real time of the power and energy available in the cell, but also provide benefits such as extending the useful lifetime of the battery cell. The lifetime is increased by avoiding overcharging and overdischarging scenarios that can cause degradation and permanent damage to the battery.

2. State of charge estimation methods

In this section we describe briefly the SoC estimation methods we investigated. Fig. 1 illustrates all the methods we have considered.

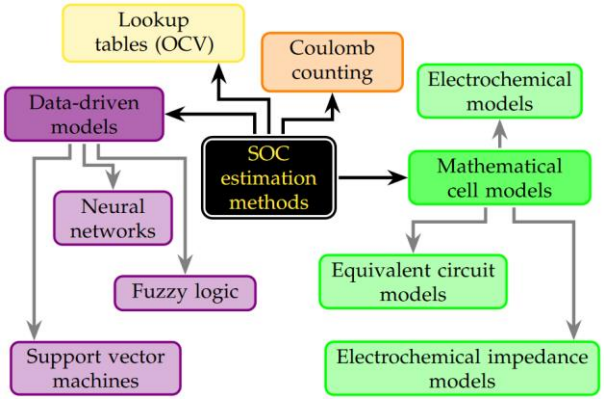

Fig.1. **Classification of the SoC estimation methods.**

2.1. Lookup table methods

In this kind of methods is implemented a direct relationship between the SoC and different static characteristics of the battery cell, for example, the open circuit voltage (OCV).

This SoC estimation method is very simple and easy to implement. However, it presents some disadvantages. First, the battery must be in equilibrium and the applied current should be very low (not common scenarios in automotive applications). Second, this method does not consider the hysteresis voltage in some cell chemistries. And third, the SoC is very sensitive to the OCV in the SoC range *20% - 90%*.

2.2. Coulomb counting

The coulomb counting is one of the simplest methods used to estimate the SoC. To estimate the SoC we only need to know the initial SoC, the cell capacity, and the current experienced by the cell. The first problem with this method is that we will never know the exact initial

SoC of the cell, nor the exact cell capacity, leading to obtain biased estimates. Furthermore, the cell current that is measured contains the true current experienced by the cell, but also contains random measurement noise and nonlinear errors associated to the measurement circuit.
The combination of all sources of error will have a negative impact on the SoC estimate. As the time passes the error will accumulate and the reliability of the estimate will decrease.

2.3. Electrochemical models

The electrochemical models (EMs) have the potential to accurately predict the behavior of a cell and provide detailed information about the internal states of the battery (lithium concentration, electrochemical and diffusion kinetic processes, etc.).
Nevertheless, the EMs are sustained on partial differential equations (PDEs) to characterize the cell internal processes. This reduces the applicability of such models in real-time applications because the methods to solve PDEs are extremely computational demanding.

2.4. Equivalent circuit models

The equivalent circuit models (ECMs) use electronic components like resistors, capacitors and voltage sources to build a circuital network capable of describing the terminal voltage of the cell.
After deriving the equations of the circuital network, different estimators like Kalman filters or particle filters can be applied to estimate the SoC.
Summarizing, the ECMs group a series of ordinary differential equations (ODEs) that can be easily implemented in BMS microcontrollers. On the other hand, estimate the SoC via ECMs could lead to errors due to the uncertainty of the cell capacity, the uncertainty of the initial SoC, modelling errors, and errors in the current and voltage measurements. Moreover, the resulting model should not be applied in scenarios very different from those from which the data was originally collected to parametrize the model.

2.5. Electrochemical impedance models

The impedance spectroscopy technique is aimed to determine a series of parameters (SoC dependent) that characterize the battery cell in a wide range of frequencies.
This method represents a very useful tool to describe the dynamic behavior of electrochemical cells, allowing to obtain the frequency response of the battery cell at any operational point.
The main limitation of this method is that the necessary equipment to perform the impedance spectroscopy is very expensive, thus, making this estimation approach not suitable for onboard electric vehicle applications.

2.6. Artificial neural networks

Neural networks (NNs) are very popular data driven techniques within the field of Machine Learning. NNs can effectively optimize the parameters of the network. Therefore, these networks have the ability to learn complex patterns with accentuated nonlinearities.
Conversely, the greatest disadvantages of the NNs are: 1) the requirement of large volumes of data in the training stage to avoid overfitting, 2) the selection of the wrong training algorithm may result in the optimization process not converging, and 3) the large amount of time and computational resources that are needed to train the neural network.

2.7. Support vector machines

The support vector machine (SVM) algorithm shares many similarities with the NNs. The main difference between these two algorithms is that the ε-SVM method does not utilize the commonly used mean squared error (MSE) as the loss function in the optimization process. Instead, ε-SVM tries to find a function that captures the underlying patterns in the data and at the same time allows a controlled level of deviation ε, increasing robustness against noise.
The estimation method based on SVMs provides the following advantages: 1) less tendency to overfitting and, 2) the SVM training involves a convex optimization problem ensuring that it converges to the global minimum, avoiding the local minima problem characteristic of neural networks.

2.8. Fuzzy logic method

Fuzzy logic is a computational approach that offers flexibility and facilitates the concept of partial truth or multi-valued logic.
This method excels in the representation and processing of uncertainty, making it robust to inaccurate or noisy data. However, this technique can present difficulties when precise modelling is crucial.

2.9. Future work

Future investigations will be centered on building neural network models to estimate the SoC in both, charging and discharging scenarios. These models will be fed with current, voltage, and temperature measurements --- data that will be obtained by cycling battery cells with different driving profiles.
Within this framework, we have already achieved progress by considering charging scenarios. We trained a feedforward NN with a single hidden layer and *100* neurons obtaining SoC estimation errors lower than *5%*. Furthermore, recurrent neural network (RNN) architectures will be implemented to integrate the temporal dependence of the SoC to the network.

Reflectometric interferometry biosensor based on nanoporous anodic alumina for hGH detection

Josep Maria Cantons, Laura K. Acosta, Pilar Formentín, J. Ferré-Borrull, Akash Bachhuka, Lluis F. Marsal*

Departament d'Enginyeria Electrònica, Elèctrica I Automàtica, Universitat Rovira i Virgili, Avinguda Països Catalans 26, 43007 Tarragona, Spain; Phone: 977 55 85 24
*Email: akash.bachhuka@urv.cat, lluis.marsal@urv.cat

Abstract

In this study, nanoporous anodic alumina (NAA) is used in order to design and fabricate a fluidic optical nanobiosensor based on reflectometric interferometry Fourier transform spectroscopy (RIFTS) to perform real-time biosensing. The optical biosensors based on NAA is fabricated throughout an electrochemical reaction on a two-step anodization. A nanoporous structure is obtained and working as our sensing platform for the detection of biomolecules. For this purpose, different concentrations of human growth hormone are used in order to test the sensing platform.

1. Introduction

Nanoporous anodic alumina has been previously used in many sensing and photonic applications due to its low-cost fabrication and optical properties [1]. NAA consists of a network of self-arranged pores perpendicular to the surface in an aluminum oxide matrix [2]. One of the most important properties of NAA is that the pore geometry (i.e., cylindrical geometry) can be exquisitely controlled by means of the anodization parameters (i.e., acid electrolyte, anodization voltage, and anodization time) [3]. This allows us to change the effective medium by designing the pore geometry and, thus, to control the specular reflection. When the nanoporous structure is exposed to visible light, it shows a reflectometric response called Fabry-Pérot interferences, this behavior is used as a sensing variable to study changes in the effective media of the NAA substrates.

In this work, we design and fabricate monolayers of NAA as a sensing platform in order to detect biomolecules. The main pur-pose is to analyse and study the changes in the effective optical thickness (EOT) by changing the refractive index of the effec-tive media. For doing that, different concentrations of human growth hormone (hGH) was used as our main target.

2. Materials and Methods

Materials

High-purity aluminium substrates (99.999%) with a thickness of 0.5 mm were purchased from Goodfellow Cambridge Ltd. (UK). Ethanol (C2H6O), acetone (C3H6O), oxalic acid (C2H2O4), perchloric acid (HClO4), chromic acid (H2CrO4), Hydrogen peroxide (H2O2), 3-Aminopropyltriethoxysilane (C9H23NO3Si), Human Serum Albumin (HSA), and IgG were provided by Sigma Aldrich. Recombinant human growth hormone (hGH) and Recombinant Anti-human growth hormone antibody (anti-hGH) were supplied by Abcam. Glutaraldehyde was provided by ANAME. Double de-ionized (DI) water (18.6 MΩ, Milli-Q®) was used for all the solutions unless otherwise specified.

Fabrication

Nanoporous alumina samples were fabricated by anodizing aluminium using a two-step anodization method. In this whole procedure, 0.3 M oxalic acid at 5 ºC was utilized [4] [5]. This method consists of first anodization that takes 20 hours at 40 V, where the pores start growing. The next step is to remove all the alumina from the surface by etching with chromic acid at 70 ºC for 3 hours [6]. The objective of this step is to obtain the aluminium surface with tiny holes from which the pores will grow in an ordered way. After that, the samples are exposed to second anodization, which utilizes the same acid and voltage conditions as the first anodization. Additionally, sample thickness is controlled by varying the charge. In our case, we wanted 6 µm of pore length, so we applied a total of 95 C for four samples anodized simultaneously. Additionally, we employed an extra step called pore widening, using phosphoric acid 5 % at 35 ºC. In this temperature condition, the growth of the pores is expected to be 1-1.5 nm/s, so we apply a pore widening reaction for 20 minutes to obtain pores up to 65 nm. After that, gold was sputtered onto the surface in order to amplify the interferences.

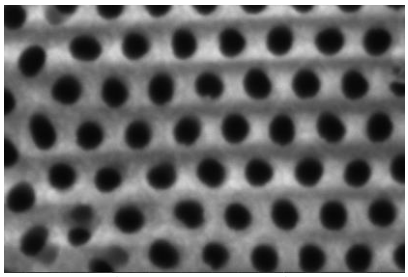

Fig.1. FESEM image of a NAA sample after the whole fabrication procedure.

APTES functionalization

The surface of the NAA was functionalized by APTES, which consists of the binding of amino groups on the alumina surface. This functionalization generates amino groups facilitating the immobilization of different biomolecules making the sensor selective. The first step in APTES functionalization is the hydroxylation of the surface. After the hydroxylation, the samples are stored for 1h at 60 ºC in the oven to ensure that the hydroxyl groups have attached to the NAA surface. Finally, the samples are exposed to 9 mL of toluene and 1 mL of 10% APTES. This last step aims to attach silane and amine groups to the hydroxylated alumina surface. Once the step is done, we keep the samples overnight at 100 ºC to promote the silane cross-linking.

Glutaraldehyde functionalization and antibody incubation

After the APTES functionalization, the silanized samples are functionalized using glutaraldehyde (GA) 10% v/v in ethanol during 1 h forming an amide bond. In these circumstances, the aldehyde groups of the GA will react with the monoclonal antibody of the growth hormone. After the GA functionalization 10 µg/mL of anti-hGH diluted in phosphate buffered saline (PBS) have been incubated in our samples overnight at 37 ºC.

Fig.2. Anti-hGH incubated on NAA samples.

3. Results

The NAA substrates were evaluated with real-time spectroscopy measurements using a flow cell and a fibre mini spectrometer. The system was tested by adding different concentrations of human growth hormone (from 40 – 75 µg/mL). PBS buffer was injected into the flow cell in order to get a stable baseline before injecting the hGH concentration. Then, the different concentration solutions were injected into the flow cell at a constant rate of 20 µL/min. Figure 3 shows the real-time monitoring of three different concentrations of hGH (75 µg/mL and 50 µg/mL and 40 µg/mL respectively) showing a change in the effective optical thickness as we are changing the effective media, and in consequence the refractive index

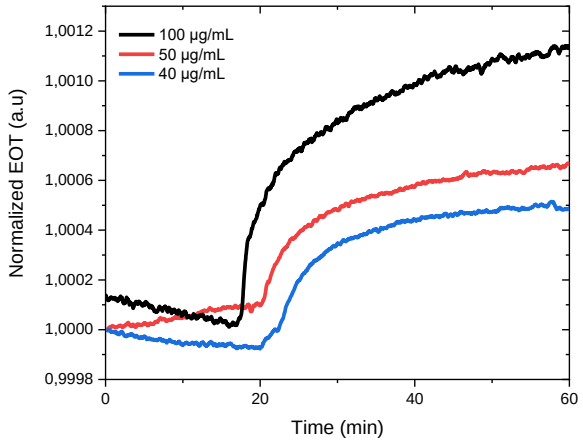

Fig.3. Normalised response of the sensor at different concentrations of hGH.

4. Conclusions

In this work we demonstrate the possibility to fabricate a nanoporous anodic alumina structure to perform a real-time sensing of biomolecules. The preliminary results showed the possibility to detect the human growth hormone. The sensor has to be further optimized in order to test different concentrations of hGH, other than the tested ones and closer to clinical values below 50 µg/mL.

Acknowledgments

This work was supported by the Spanish Ministerio de Ciencia e Innovación (MICINN/FEDER) PDI2021-128342OB-I00, by the Agency for Management of University and Research Grants (AGAUR) ref. 2021-SGR-00739, Juan de la Cierva incorporation fellowship (IJC-2019-042374-1), Beatriu de Pinos Grant (2021 BP 00105) and by the Catalan Institution for Research and Advanced Studies (ICREA) under the ICREA Academia Award.

References

[1]. M.M. Rahman, L.F. Marsal, J. Pallarès, J. Ferré-Borrull, ACS Appl. Mat. Interfaces, 2013, 5, 13375-13381.

[2]. J. Ferré-Borrull, J. Pallarès, G. Macias, L.F. Marsal, Materials, 2014, 7, 5225-5253.

[3]. A. Santos, V.S Balderrama, M. Alba, P. Formentín, J. Ferré-Borrull, J. Pallarès, L.F Marsal, Nanoscale, 2012, 7(1).

[4]. A. Santos, C Suwen Law, T. Pereira, D. Losic, Nanoscale, 2016, 8, 8091-8100.

[5]. A. Santos, J. Ferré-Borrull, J. Pallarès, L.F. Marsal, physica status solidi, 2011, 208(3), 668-674.

[6]. A. Santos, L. Vojkuvka, M. Alba, V.S Balderrama, J. Ferré-Borrull, J. Pallarès, L.F Marsal, physica status solidi, 2012, 209(10), 2045-2048.

Carbon dots as photoactive platforms for the photocatalytic reduction of CO_2

Beatriu Domingo Tafalla[a,*], Beatrice Bartolomei[b], Maurizio Prato[b,c], Emilio Palomares[a,*,♦,†]

Carbon dots possess optical properties that make them suitable metal-free light absorbers for the development of hybrid systems for the photocatalytic conversion of CO_2. The surface of carbon dots can be used to anchor molecular catalysts which will ensure high activity and product selectivity. On this basis, we developed a model hybrid system in which nitrogen-doped carbon dots function at the same time as an anchoring scaffold and a photosensitizer of an iron porphyrin for the photoreduction of CO_2 to CO.

Introduction

The capture and conversion of CO_2 into value-added products are under investigation in order to counteract the increasing emissions of CO_2. A viable approach is to convert CO_2 using solar light (photocatalysis). In this regard, the most studied materials for the photoreduction of CO_2 are metal oxides, particularly, TiO_2, MgO, Ga_2O_3, Bi_2MoO_6, In_2O_3, and Ta_2O_5 [1]. However, product selectivity of heterogeneous catalysts is an issue.

As an alternative, the use of hybrid systems that combine a photoabsorber and a molecular catalyst selective for a specific product has gained attention. Carbon dots (CDs), with easy large-scale production, high chemical stability and excellent photo/electro properties are promising candidates for the design of this kind of hybrid systems [2]. Their highly functionalized surface can serve as a platform for covalent anchoring of molecular catalysts.

In this work, we anchor an iron porphyrin to the surface of nitrogen-doped CDs (N-CDs), easily produced by microwave synthesis, via amide bond. The hybrid showed the best performance under photoelectrocatalytic CO_2 reduction conditions, with CO as the main product.

Methodology

Synthesis of PyrCA@FePor hybrid

Hydrophobic PyrCA N-CDs where synthesized as early reported by Prato et al. (Scheme 1) [3].

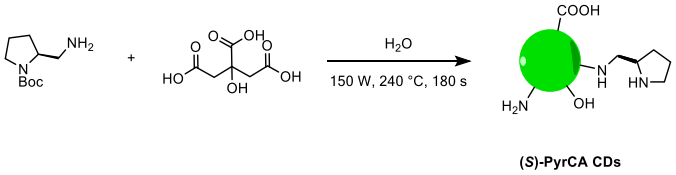

Scheme 1. Microwave synthesis of PyrCA N-CDs.

In order to obtain the hybrid, 8.4 mg of FePor-COOH (0.01125 mmol) and 2 eq. of EDC/NHS were dissolved in 4 mL of dry DMF and left under agitation for 20 minutes to achieve the activation of the carboxylic acid of the FePor-COOH. Then, 25 mg of PyrCA N-CDs were added and the reaction mixture was agitated under Ar for 48 h. Afterwards, the solvent was removed by rotatory evaporation and the resulting solid was re-dissolved in the minimum amount of DCM. It was precipitated in diethyl ether and collected though centrifugation (6000 rpm, 10 min). The process was repeated two more times by using THF:diethyl ether 1:3 as the precipitation solvent. After drying, the final material was obtained as a pink powder (21 mg) (Scheme 2).

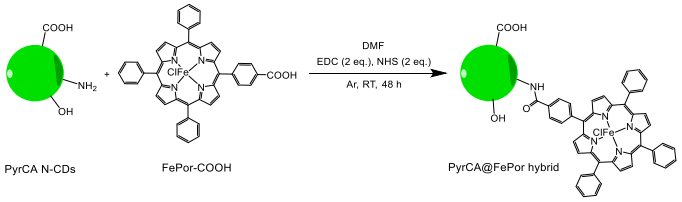

Scheme 2. Covalent functionalization of PyrCA N-CDs with FePor-COOH.

Photo-, eletro- and phtooelectrocatalytic characterization

Electro- and photoelectrocatalytic CO_2 reduction experiments were performed in DMF/0.1 M $TBAF_6P$ electrolyte with a glassy carbon plate as the working electrode, Ag/AgCl as de reference electrode and a Pt wire as the counter electrode. Photocatalytic CO_2 reduction experiments were performed in DMF:water 19:1 0.1 M triethylamine solvent. For measurements under light, a 365 nm LED was employed. For all the experiments a concentration of 0.2 mg/mL PyrCA N-CDs or PyrCA@FePor hybrid were used. Besides, FePor-COOH alone (20 µM) and FePor-COOH (20 µM) in combination with PyrCA N-CDs (0.2 mg/mL) were assessed under the same conditions.

Results

Characterization of PyrCA@FePor hybrid

Fourier transform infrared spectroscopy (FT-IR) verifies the presence of carboxylic acid (sharp peak at 1705 cm^{-1}) functional groups and amine bonds (doublet at 1500-1690 cm^{-1}) on the surface of PyrCA N-CDs (Fig. 1A). FT-IR

[a]Institute of Chemical Research of Catalonia (ICIQ), Tarragona, Spain, e-mail: bdomingo@iciq.es

[b]Department of Chemical and Pharmaceutical Sciences, INSTM, UdR Trieste, University of Trieste, Trieste, Italy.

[c]Center for Cooperative Research in Biomaterials (CIC Bioma-GUNE), Basque Research and Technology Alliance (BRTA), Donostia San Sebastián, Spain

*Universitat Rovira i Virgili (URV), Tarragona, Spain

♦Catalan Institution for Research and Advanced Studies (ICREA), Barcelona, Spain.

†Universidad de Pau y Pays de l'Adour (UPPA), Pau, Francia.

spectra of the PyrCA@FePor hybrid presents the Fe-N stretching vibration (1002 cm^{-1}) and C-H bending vibration (730-860 cm^{-1}) of the phenyl ring of the FePor-COOH. UV-Vis absorbance spectroscopy of the ºPyrCA@FePor hybrid shows bands of both the PyrCA N-CDs (large absorbance at <290 mn and broad band at 300-450 nm) and FePor-COOH (Soret band at 415 nm) (Fig. 1B). Finally, the cyclic voltammogram presents the reversible redox signals Fe^{III}/Fe^{II}, Fe^{II}/Fe^{I} and Fe^{I}/Fe^{0} of the FePor-COOH in the hybrid with a 20 mV shift in comparison to the free FePor-COOH, indicating the electronic interaction of both components.

Catalytic CO_2 reduction characterization

The catalytic activity of the PyrCA@FePor hybrid was compared to the activity of the FePor-COOH alone and to the mixture of PyrCA N-CDs with FePor-COOH. As seen in Figure 2A, the faradaic efficiency for CO production (FE_{CO}) of FePor-COOH is not enhanced by the combination with PyrCA N-CDs (with or without covalent attachment of the catalyst). In fact, the FE_{CO} of the hybrid is lower than that of the FePor-COOH alone, even under light irradiation. To low diffusion of the hybrid in solution could explain such behaviour. On the other hand, as seen in Figure 2B, the presence of PyrCA N-CDs induces the production of H_2 from the FePor-COOH catalyst, and slightly enhances the production of CO with respect to the FePor-COOH alone. Thus, PyrCA N-CDs can work as a photosensitizer but favour the hydrogen evolution reaction (HER) over CO_2R in FePor-COOH molecular catalyst.

Conclusions

An hybrid system composed of N-CDs functionalized via covalent attachment with an iron porphyrin has been prepared. The hybrid has been tested under electro-, photo- and photoelectrocatalytic CO_2R conditions, and the effect of the N-CDs has been proven detrimental for the performance of the molecular catalyst.

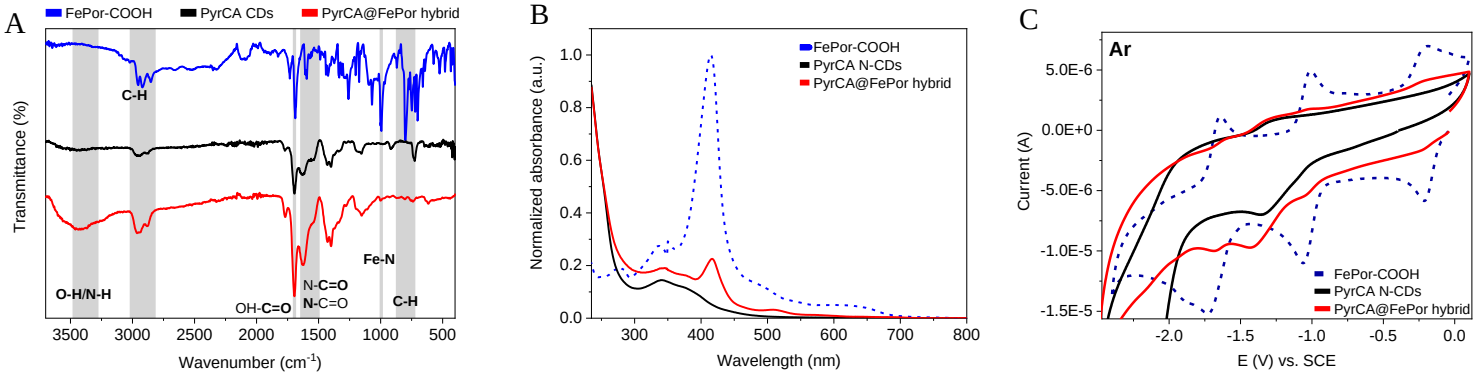

Figure 1. FT-IR (A), UV-Vis absorbance spectrum of DCM solutions (B) and cyclic voltammogram in DMF electrolyte (C).

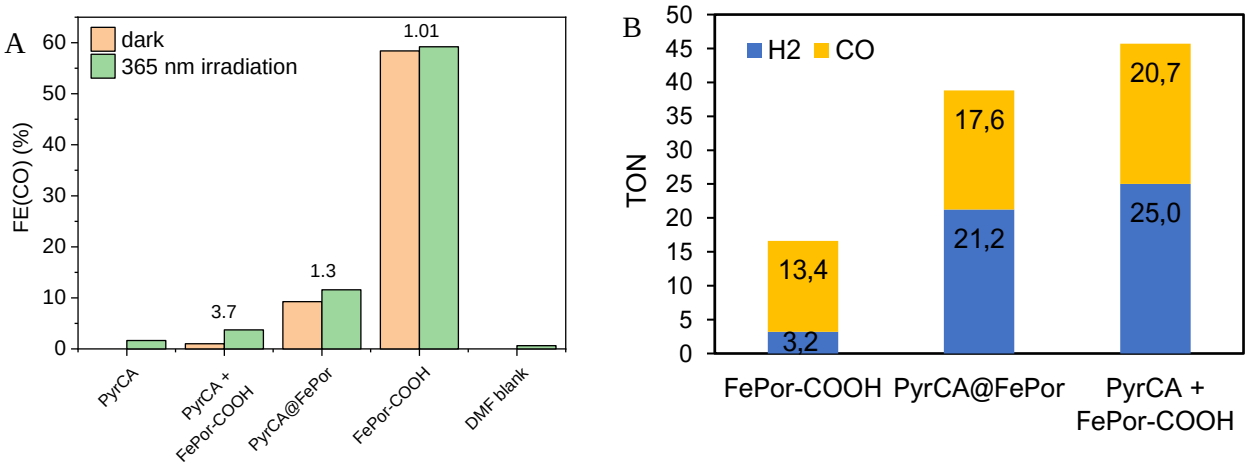

Figure 2. (Photo)electrocatalytic (A) and photocatalytic (B) performance of the measured systems.

Bibliography

[1] A. Call *et al.*, "Improved electro-and photocatalytic water reduction by confined cobalt catalysts in streptavidin," *ACS Catal.*, vol. 9, no. 7, pp. 5837–5846, 2019.

[2] L. Đorđević, F. Arcudi, and M. Prato, "Preparation, functionalization and characterization of engineered carbon nanodots," *Nat. Protoc.*, vol. 14, no. 10, pp. 2931–2953, 2019.

[3] B. Bartolomei, V. Corti, and M. Prato, "Chiral Carbon Nanodots Can Act as Molecular Catalysts in Chemical and Photochemical Reactions," *Angew. Chemie - Int. Ed.*, vol. 62, no. 32, 2023, doi: 10.1002/anie.202305460.

Perovskite Nanocrystals for the Fabrication of Light Emitting Diodes

Georgios Papathanidis [a, b], Eugenia Martinez [a], Emilio Palomares-Gil [a, b]

[a] *Institute of Chemical Research of Catalonia (ICIQ), The Barcelona Institute of Science and Technology, Tarragona 43007, Spain*
[b] *Departament d'Enginyeria Electrònica, Elèctrica i Automàtica, Universitat Rovira i Virgili, Avinguda dels Països Catalans, 26, Tarragona, Spain*

Abstract

Metal halide perovskite materials, such as $CsPbBr_3$, are new upcoming optoelectronic materials that have attracted the attention in the field of optoelectronics, as solution based deposited absorbing layers in light emitting diodes, and solar cells. Here we present a new way for halide perovskites by designing colloidal perovskite-based high-luminescent nanocrystals. We have synthesized monodispersed colloidal nanocrystals of fully inorganic lead halide perovskites using inexpensive commercial precursors. The final aim of this work is to fabricate Light Emitting Diodes with high luminescence, using the $CsPbBr_3$ nanocrystals.

1. Introduction

Perovskite quantum crystals have proven to be promising materials for a wide range of applications in optoelectronics[1]. These applications include light-emitting diodes, photodetectors, photovoltaics, lasers, and sensors. This is related to their advantages such as their narrow emission spectra, tunable colors and high color purity, high quantum yields (PLQYs), low cost and substantial optical gain coefficients[2,3]. In addition, perovskite quantum crystals are ideal for the study of light-diester interactions, due to the strong confinement of the excitation energy within the nanocrystals. While the PLQYs of perovskite nanocrystals in solution are extremely high, their performance as solid-state thin films lags far behind that of solutions[3]. Consequently, this has resulted in the demand for new ways and strategies to improve and achieve high PLQYs in perovskite solid-state thin films (Figure 1).

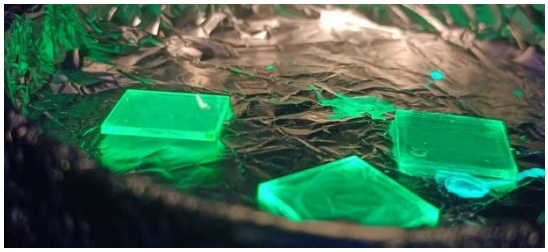

Figure 1. Perovskite solid-state thin films

2. Synthesis of $CsPbBr_3$ Nanocrystals

The synthesis of the $CsPbBr_3$ nanocrystals followed the hot injection method. Initially, 0.407 g of Cs_2CO_3 placed in a three-necked flask with 1.25 ml of Oleic Acid (OA) and 20 ml of Octadecene (ODE) under stirring and heated at 130 ^oC under for 1 h in Vacuum. 0.345 Lead Bromide ($PbBr_2$) placed in a new three-neck flask with 2.5 ml of Oleic Acid (OA), 2.5 ml of Oleylamine (OLEA) and 25 ml of Octadecene (ODE) under stirring and heated at 130 ^oC under for 1 h in Vacuum. After 1 h, both flasks filled with nitrogen and in the flask with the precursor solution the temperature increased at 170 ^oC until the complete dissolution of the cesium carbonate. In the flask with the Lead Bromide the temperature increased at 180 ^oC until a clear solution was obtained. Then, 2 ml of the precursor solution was swiftly injected after and after 5 sec, the flask immersed into water ice bath to stop the reaction. Additionally, the crude transferred to a falcon and centrifuged at 4500 rpm for 20 min. The supernatant was discarded, and the precipitate was dispersed in 5 ml of hexane. 5 ml of MeOAc was added to the dispersion and a second centrifugation was carried out at 4500 rpm for 20 min. In addition, the supernatant was discarded and the solid was redispersed in 2 ml of hexane, and a third centrifugation was carried out in the same conditions. The precipitate was stored in Eppendorf vial at (-18 ^oC) overnight and carefully decanted to remove the solid sediment deposited at the bottom. Finally, the dispersion was transferred to a glass vial, dried with gentle nitrogen flow and introduced in vacuum for 15 min to obtain the $CsPbBr_3$ nanocrystals as a solid (90-100 mg).

3. Fabrication of Quantum Crystal LEDs

The LEDs was fabricated according to the typical p-i-n architecture as shown in the (Figure 2). For the fabrication of the LEDs, PEDOT: PSS and Poly-TPD was used as a hole transporting layer, $CsPbBr_3$ nanocrystals as the emission layer, TPBi and Ca as an

electron transporting layer and Al as a top and a bottom electrode of the devices. ITO conductive glass slides were cleaned in isopropanol (IPA) and sonicated for 1 h. After the sonication, the ITO glasses were placed in the UV-O_3 for 30 min. The PEDOT: PSS was spin coated at 3000 rpm for 45 sec and placed on a hot plate to dry at 120 ºC. The second layer of the Poly-TPD followed the same procedure. The $CsPbBr_3$ nanocrystals dispersed in 2 ml of Hexane, spin coated at 1000 rpm for 35 sec and placed on a hot plate at 70 ºC for 20 min. Additionally, the TPBi and Ca was evaporated using a square mask, until it is achieved a thickness of 40 nm and 1 nm respectively. Finally, the Al electrodes was deposited via chemical evaporation using a square mask to separate the top and the bottom conducts.

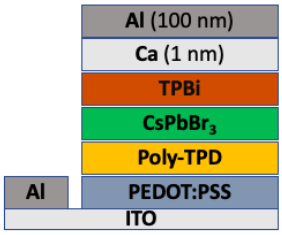

Figure 2. LEDs Stracture

4. Results and Discussion

The $CsPbBr_3$ nanocrystals were characterized with UV-Vis spectroscopy, and photoluminescence spectroscopy (PL), to confirm the excitonic absorption peak and the emission of the nanocrystals. Additionally, the quantum yield (QY) of the perovskite nanocrystals was calculated using curamine 153 for reference, as well as the absorption and the emission of the nanocrystals. (Figure 3a), shows the Uv-Vis spectrum of the comparison between the P. Nanocrystals (GP_003) and the curamine C-153. The C-153 has an absorption peak at 421 nm. The GP_003 has an abs peak at 504 nm and a smaller peak at 407 nm.

(Figure 3b), shows the PL spectrum of the P. Nanocrystals (GP_003) in comparison with the C-153. The excitation wavelength was 424 nm. The C-153 has an emission peak at 526 nm. The sample GP_003 has an emission peak at 512 nm. P. Nanocrystals have one emission peak at the PL spectrum which indicates that there is only one population of quantum dots.

Transmission electron microscopy (TEM) was used to identify and confirm and shape and the size of the nanocrystals as shown in (Figure 4).

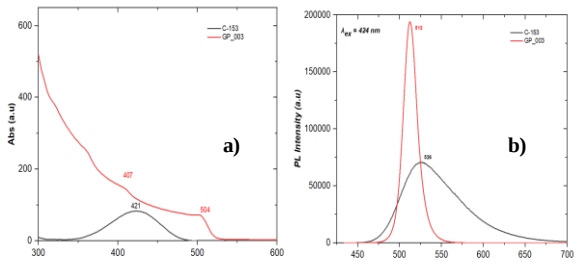

Figure 3. UV-Vis and PL spectrum of Curamin-153 and $CsPbBr_3$ Nanocrystals

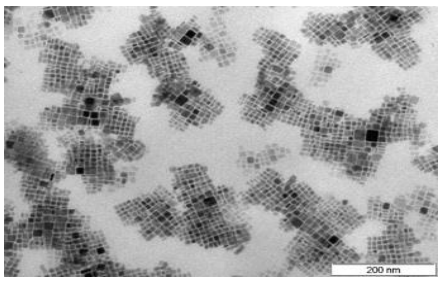

Figure 4. TEM images of CsPbBr3 Nanocrystals.

The characterization of the LEDs was carried out, using a camera (as a detector) and a Keithley source. The samples were placed in a holder and a potential with a range of 0 - 12 V was applied. (Figure 4a, b), shows the Luminance and the Current density of the LEDs. According to these measurements, the Luminance is 340 cd/m^2 and the emission of the devices starts after 6 V, which indicates that the devices have a high resistance (Figure 5).

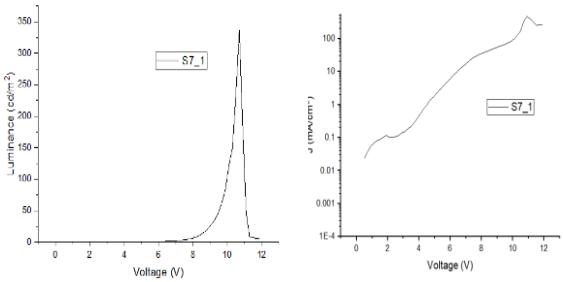

Figure 2. LEDs Measurement of Luminance and Current Density

5. Conclusions

The synthesis of the $CsPbBr_3$ Nanocrystals was successful with a QY at 69 %. The devices have a luminance of about 340 cd/m^2, but they have quite high resistance and so their performance is reduced. Regarding the performance of the devices because of the high resistance, the main problem is the thickness of the deposited layers.

References

[1] Sánchez, Rafael S., et al. "Radiative Recombination Processes in Halide Perovskites Observed by Light Emission Voltage Modulated Spectroscopy." *Advanced Materials* 35.11 (2023): 2207993.

[2] Protesescu, Loredana, et al. "Nanocrystals of cesium lead halide perovskites (CsPbX3, X= Cl, Br, and I): novel optoelectronic materials showing bright emission with wide color gamut." *Nano letters* 15.6 (2015): 3692-3696.

[3] Kumar, Gautham, et al. "Enhancing photoluminescence performance of perovskite quantum dots with plasmonic nanoparticles: insights into mechanisms and light-emitting applications." *Nanoscale Advances* 6.3 (2024): 782-791

Two-Phase *LLC* Converter with Common *LC* Branch for Inherent Current-Sharing and Phase-Shedding Ability

Ubaid Ahmad
Departament d'Enginyeria Elèctrica, Electrònica i Automàtica.
Universitat Rovira i Virgili.
Tarragona, Spain.
ubaid.ahmad@urv.cat

Roberto Giral
Departament d'Enginyeria Elèctrica, Electrònica i Automàtica.
Universitat Rovira i Virgili.
Tarragona, Spain.
roberto.giral@urv.cat

Carlos Olalla
Departament d'Enginyeria Elèctrica, Electrònica i Automàtica.
Universitat Rovira i Virgili.
Tarragona, Spain.
carlos.olalla@urv.cat

Abstract

This paper presents a two-phase input-parallel output-parallel *LLC* resonant converter with a common inductor capacitor branch, such that current-sharing and phase-shedding capabilities are achieved. Thanks to the common *LC* branch, current-sharing is inherent, and phase-shedding can be performed with no influence in the operating point. With few passive components in the tank circuit and with a simple connection between the two-phases, it exhibits low-cost, high-power density, and high light-load efficiency, with respect to the existing converters. A detailed analysis of the primary and the secondary side current-sharing is presented, which confirms improvements when compared to previous approaches. Simulation and experimental results of the proposed converter validate the analysis and illustrate the effectiveness of the current-sharing and phase-shedding capacities with a power rating of 800 W.

1. Introduction

The *LLC* resonant converter is a promising solution in data centers, communications supplies, and electric vehicle battery chargers, among others, due to its zero-voltage and zero-current switching capability, which can achieve high efficiency and power density [1]-[3]. However, in high-power or high output current applications, the current stress on the secondary side and its bulky filter capacitor limits the use of the *LLC* converter. To alleviate the current stress and reduce the filter size, the *LLC* converter can be adapted to the input-parallel output-parallel (IPOP) configuration [1]-[3]. However, small differences in the gain of the resonant tanks in the IPOP circuits result in uneven current distribution. This experimental discrepancy in gains of the resonant tanks is unavoidable, and it is caused by tolerances in the resonant capacitors, inductors, and magnetizing inductances. Other mismatches are avoidable and/or minor compared to these, e.g., differences in the ON-resistance of the switches, mismatches in the gate signals, and other uneven path resistances and parasitics. Therefore, the current-sharing is an important issue in IPOP connected *LLC* resonant converters, which needs to be addressed.

To tackle this issue, many different techniques have been proposed so far, including: control-based current-sharing (CS), including variable frequency and phase-shift control, active CS using switch-inductor and switch-capacitor techniques or passive CS including magnetics-based [1]-[3] and capacitive-based techniques, Other passive CS approaches include grouping secondary windings of the transformers, an improved version of that method, and CS based on virtual voltage sources. Also, the output filter has been used for balanced current-sharing, and a common *CL* and/or *CLC* filter-based method is presented. Finally, it is also possible to achieve CS with passive impedance matching, with a common inductor (*CI*), a common capacitor (*CC*), or with a unified common inductor and common capacitor (*UCICC*).

2. Proposed Converter

The circuit diagram of the proposed two-phase *LLC* resonant converter is depicted in Fig. 1. The circuit consists of half-bridges on the primary sides (four active switches), a common *LC* branch (Lr, Cr) with a single point of common connection (lc), two high-frequency center-tapped transformers with turns ratio (n), and a full-wave rectifier for each phase of the converter, requiring a total of four diodes.

The proposed converter, depicted in Fig. 1, exhibits the following desirable features:

1) The resonant tanks in the proposed two-phase *LLC* converter require only two passive components (one capacitor and one inductor).
2) Compared to the *CI* and *CC* methods, the resonance frequency of the proposed converter does not change when one of the phases is turned-OFF. Hence, the gain and the high efficiency operating point of the converter remain unchanged.
3) Compared to the *UCICC* method, the points of connection in the resonant tank elements are reduced from three to one, which reduces system complexity.
4) The proposed converter can achieve phase-shedding ability, in contrast with the *CI*, *CC*, and *UCICC* methods.
5) Since the proposed method utilizes the single *LC* branch for two-phases, the mismatches in the resonant tanks are eliminated. This ensures natural current sharing.

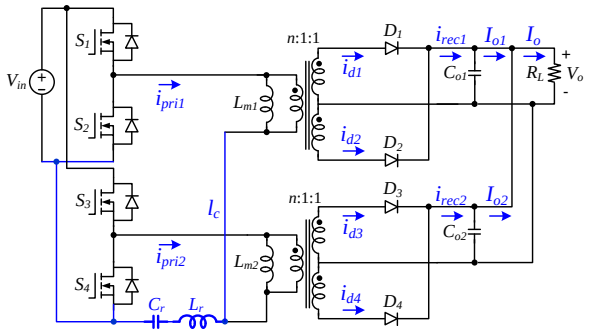

Fig. 1 Proposed two-phase *LLC* resonant converter.

3. Experimental Results

A hardware prototype of 800 W has been designed and built to show the effectiveness of the proposed method. The *LLC* converter in phase #1 is utilized as a reference.

To show the imbalance in the currents in the conventional two-phase *LLC* converter, a second module is designed and fabricated with a mismatch in tank circuit parameters of 10% compared to module #1. Since it can be expected that the power is to be delivered only by module #1, the tests have been limited to a power rating of 400 W, the maximum power capability of a single *LLC* module. It can be seen from the waveforms in Fig. 2 that the diode rectifier currents in module #2 is zero, as id4=0 A, while id1 (module #1) is responsible for delivering all the power to the load.

The experimental results of the proposed converter with full-load condition are depicted in Fig. 3, which shows the transformer primary currents and the rectifier diode currents of the two modules. It can be seen that with the proposed technique the currents are equally shared between the two modules, which makes the parallel connected two-phase *LLC* converter more reliable. Although, the currents seem to be very well shared, we present the mean values of the rectifier diode currents and the rms values of the transformer primary currents. The values have been measured using a Tektronix MDO3014 oscilloscope. It can be seen that, at the full-load condition, the current sharing error in the primary side of the converter is 2.48 %. On the secondary side, it is 1.58 % in diodes 1 and 4.

The efficiency of the proposed two-phase *LLC* converter is captured at different power levels, as shown in Fig. 4. The peak efficiency of the proposed converter was 94.1 %. Since the proposed converter can achieve phase-shedding by turning-OFF one of module at or below 50 % load condition, hence, it can improve the light-load efficiency. At 50 % load condition, a 3.6 % increase in efficiency is observed while at 25 % load condition the efficiency increase of 6.82 % is observed. The efficiency with phase-shedding is plotted in red colour in Fig. 4. The dotted green colour shows the combine efficiency plot of the proposed converter in Fig. 4.

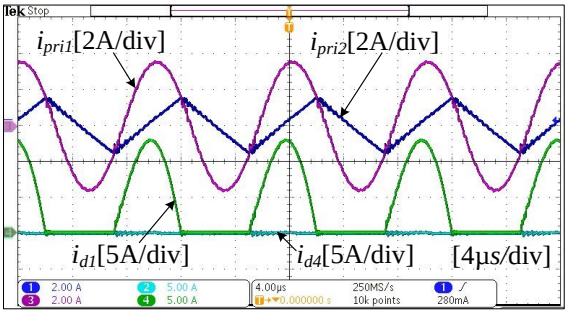

Fig. 2 Experimental results of conventional two-phase *LLC* converter, transformer primary currents (ipri1, ipri2) and diode rectifier currents (id1, id4),

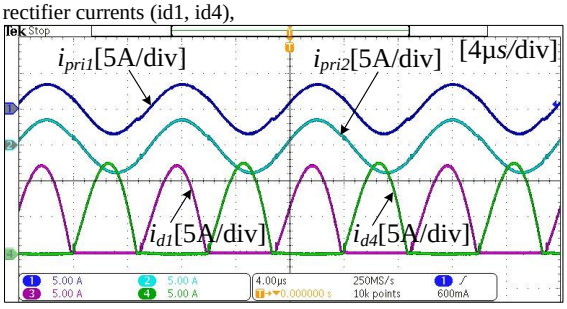

Fig. 3 Experimental results of the porposed two-phase *LLC* converter, transformer primary currents (ipri1, ipri2) and diode rectifier currents (id1, id4),

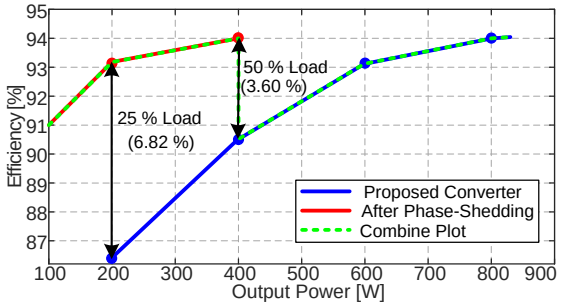

Fig. 4 Efficiency plot of the proposed converter.

7. Conclusion

This paper presents a two-phase parallel-connected *LLC* resonant converter with a shared inductor-capacitor branch. An excellent performance in current-sharing and phase-shedding are achieved without introducing complex control techniques, and without adding active or passive additional components. By sharing the inductor-capacitor resonance branch between two phases, the power density of the two phases is improved. Besides, with phase-shedding the light load efficiency is greatly improved. The proposed converter is ideal for high step-down applications, achieving excellent current sharing in high current rectifiers, transformers, and primary switching devices.

References

[1] U. Ahmad, H. Cha, "Integrated current balancing transformer-based input-parallel output-parallel *LLC* resonant converter modules," *IEEE Trans. Power Elect.*, vol. 36, no. 5, pp. 5278–5289, May 2021.

[2] U. Ahmad, Cha, H., Ro, J.-S, "Integrated current balancing cells based IPOP bidirectional *CLLC* resonant converter modules for high-power applications. *IET Power Electron.* 15,1687–1698, 2022.

[3] U. Ahmad, *et. al.*, "Integrated current balancing transformer-based input-parallel output-parallel *LLC* resonant converter modules" *10th Int. Conf. on Power Electron., ECCE Asia, S. Korea*, pp. 1133–1140, 2019.

Synthesis of SnS2 nanosheets via CVD methods for ppb-level NO2 detection

Aladine Fdhila[1,2], Fatima Ezahra Annanouch[1], Zouhair Haddi[2], Eduard Llobet[1]

1. Departament d'Enginyeria Electronica, Universitat Rovira i Virgili, Països Catalans 26, 43007 Tarragona, Spain
2. NVISION Systems and Technologies, Avenida de Barcelona 105, 08700 Igualada, Barcelona, Spain

Corresponding Author: eduard.llobet@urv.cat

Abstract

Aerosol assisted and atmospheric pressure chemical vapor deposition methods (AACVD and APCVD) were combined to successfully synthesize tin disulfide (SnS_2) nanosheets. Analysis of morphology and composition revealed that this new method is appropriate for generating TMDs nanomaterials of superior quality. Three distinct sensors based on SnS_2 nanosheets were created and tested toward NO_2 by varying the sulfurization time (i.e., 30, 60, and 90 minutes). The findings demonstrated that all of the sensors could identify NO_2 at low operating temperatures, with the sensor that had sulfurization for 90 minutes recording the largest response.

1. Introduction

Two-dimensional (2D) materials, particularly transition metal dichalcogenides (TMDs), have attracted considerable interest due to their tun-able bandgaps and exceptional electrical and optical characteristics. They offer a promising solution to common shortcomings (i.e., high operating temperature lack of selectivity) seen before in materials like carbon nanotubes, met-al oxides, and graphene. Among TMDs, SnS_2 nanostructures exhibit ideal characteristics for gas sensing applications, including large sur-face area, rich in active reaction sites, high sensitivity to various gases, selectivity, stability, and reliability over prolonged use. However, SnS_2 synthesis faces some challenges. Various methods that have been used, such as hydro-thermal synthesis and exfoliation techniques, have drawbacks like long reaction times, low yields, discontinuous films, environmentally unfriendly precursors and solvents etc. Herein, we introduce a novel way to successfully synthesize SnS_2 via the combination of AACVD and APCVD techniques. This approach allows us to directly deposit the TMDs on the sensor transducer, without the need of further transfer steps, improves the film quality and its long-term stability and resulted in highly sensitive and stable gas sensors.

2. Experimental details

The sensing films were directly grown on to alumina substrate, with Pt interdigitated electrodes in the front side and a Pt resistive heater in the back side.

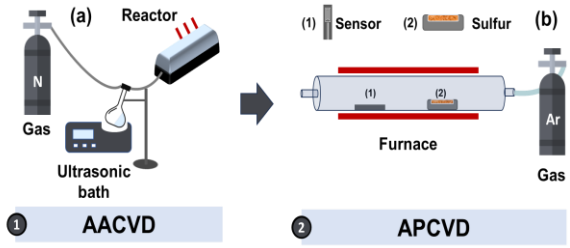

Fig.1. (a) AACVD synthesis of SnO_2 nanostructures, and (b) APCVD synthesis of SnS_2 nanosheets.

Two steps of deposition were used to synthesize SnS_2: the first one (Fig.1 a), involved the direct growth of tin dioxide (SnO_2) nanostructures from the AACVD of 30 mg of tin(IV) chloride pentahydrate dissolved in 15 ml of acetone at temperature of 450ºC. Herein, 0.5 L/ min of nitrogen, was used as a carrier gas. In the second step, the obtained SnO_2 nanostructures were subjected to an APCVD sulfurization process with argon serving as a carrier gas and sulfur powder (Fig.1 b). This process allowed the sensitive layer to grow directly at the alumina sensor transducer.

3. Results and discussions

First, we investigated the morphology of the SnO_2 nanostructures, displayed in Fig.2a, then the morphology of the produced SnS_2 nanosheets which is shown in Fig.2b. As we can see, SnS_2 nanosheets were successfully grown with a perfect hexagonal shape, on top of the alumina substrate, using a straightforward combination of AACVD and APCVD techniques.

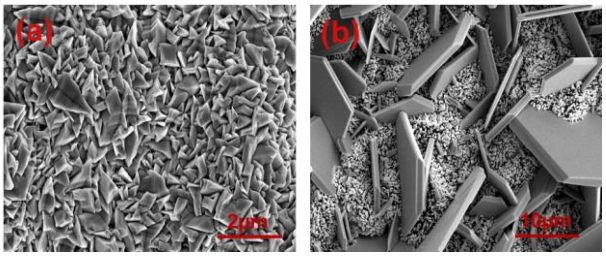

Fig.2. FESEM images of (a) SnO2, (b) SnS2.

We examined our sample using Raman spectroscopy in order to verify the composition and structure of SnO_2 and SnS_2. The Raman spectrum of SnO_2 (Fig.3a) is characterized by the classical vibrational band (A_{1g}) observed at 631 cm−1 assigned to SnO_2 rutile structure. We also observed other peaks of 251 and 353 cm−1 which can be assigned to optical phonon modes of SnO_2 (E_u (LO) and E_u (TO)) [1]. Regarding the SnS_2 spectrum (Fig.3b), we can see a sharp peak at 314 cm−1 and a small one at 204 cm−1 which are assigned to the vibrational modes (A_{1g}) and (E_g) of SnS_2 respectively [2]. All the finding confirmed the ability of our novel technique to produce SnS_2 from the direct sulfurization of SnO_2 nanostructures.

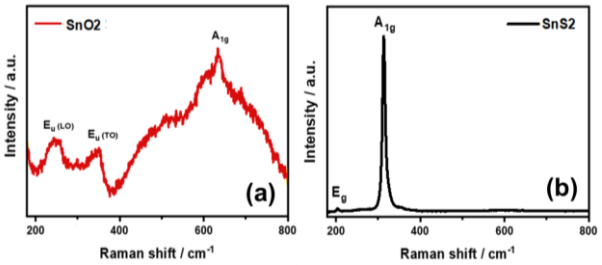

Fig.3. Raman spectra of (a) SnO_2, (b) SnS_2 nanostructures.

For gas sensing measurement, we fabricated three sensors with different sulfurization times (Sensor (A) 30 min; Sensor (B) 60 min; and Sensor (C) 90 min). The sensors were tested towards 500 ppb of NO_2, at different operating temperatures (RT, 50, 100, and 150ºC), in order to study its effect on the sensor responses. From Fig.4, we can observe that the optimal working temperature, for all the sensors, was 150ºC, while the highest sensitivity was shown by sensors with 90 min of sulfurization. Be-sides, at room temperature, sensors (C) were able to detect the target gas at ppb-level, with enough sensitivity. Fig.5 gives an example of the real sensor response as a function of time toward 500 ppb of NO_2 at 150ºC. All sensors exhibited a p-type semiconductor behavior, decreasing resistance upon exposure to oxidizing gas and increasing it upon exposure to dry air.

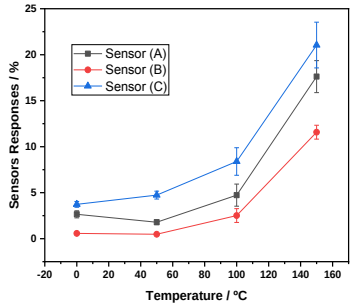

Fig.4. Sensor responses toward 500 ppb of NO_2 as a function of temperature.

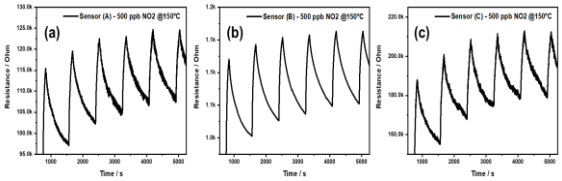

Fig.5. Responses of SnS_2 gas sensors sulfurized for (a) 30min, (b) 60min, and (c) 90min, @150ºC toward 500 ppb of NO_2.

Fig.6 depicts the sensors responses as a function of NO_2 concentration. From the graph, the sensors responses increased by increasing the gas concentration, showing a linear behavior, which is very important parameter for real gas sensing application.

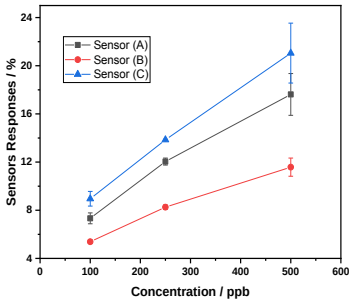

Fig.6. Sensor responses toward NO_2 @ 150 ºC as a function of concentration.

4. Conclusions

This work reported a facile and scalable technique, to synthesize highly sensitive 2D hexagonal SnS_2 nanosheets, directly onto the sensor transducer, for the detection of ppb-level of NO_2 at low operating temperature. Details on humidity cross-reactivity will be shown at the conference.

References

[1] T. Ahmad, M. Z. Ansari, Enhancement of infrared shielding property of SnO2 using Sb as a dopant, Materials Research Ex-press 10, 105902, 2022.

[2] Y. Ren, Q. Shi, G. Zhang, Lithium Storage Properties of TiC-Modified SnS2 Nanosheets, ChemElectroChem 6, e202101567, 2022.

Simulation of Bimodally Distributed Stochastic Weight in Pulse-Programmed Memristive Crossbar Arrays

Nadine Dersch[1,2], Eduardo Perez[3,4], Christian Wenger[3,4], Christian Roemer[1,2], Mike Schwarz[1], Benjamin Iniguez[2], Alexander Kloes[1]

[1]NanoP, THM University of Applied Sciences, Giessen, Germany, [2]DEEEA, Universitat Rovira i Virgili, Tarragona, Spain, [3]IHP-Leibniz-Institut für innovative Mikroelektronik, Frankfurt (Oder), Germany, [4]BTU Cottbus-Senftenberg, Cottbus, Germany

***Abstract*—In this paper, we present a method of implementing memristive crossbar array with bimodally distributed weights. The bimodal distribution is a result of pulse-based programming. The memristive devices are used for the weights and can only have an ON (logical "1") or an OFF (logical "0") state. The state of the memristive device after programming is determined by the bimodal distribution. The highly efficient noise-based variability approach is used to simulate this stochasticity. The memristive crossbar array is used to classify the MNIST data set and comprises more than 15,000 weights. The interpretation of these weights is investigated. In addition, the influence of the stochasticity of the weights and the accuracy of the weights on the classification results is considered.**

Keywords- artificial neural networks, memristive crossbar array, bimodal distribution, noise-based simulation, pulse-programming, variability

I. Introduction

Memristive devices (MDs) are non-volatile memories and are considered promising candidates for the development of hardware-based artificial neural networks (ANNs) [1][2]. The MDs can be in one of the two: states low-resistive-state (LRS) and high-resistive-state (HRS) [3]. During the SET process, the MD is switched to LRS, which corresponds to a logical "1". The RESET process switches the MD to HRS, which corresponds to a logical "0". The MDs exhibit stochastic fluctuations which result in device-to-device and cycle-to-cycle variability [4]. This stochasticity variability can be simulated using the Noise Based Variability Approach (NOVA) [5]. ANNs can be implemented as a memristive crossbar array, whereby a single cell, consisting of two MDs, functions as a weight with possible values from -1 to +1 [6].

II. Setup of the Memristive Crossbar Array and Programming Scheme

To classify the MNIST data set (images consisting of 28x28 pixels), the memristive crossbar array consists of 784 inputs, 10 outputs and 15,680 memristive cells (as in [5]). In the simulation, the MDs are considered as simple fluctuating resistors for simplicity. Two memristive cells are required to design a weight W between -1 and +1: one G^+ and one G^- cell (see Eq. 1 for calculation).

$$W = G^+ - G^- \qquad \text{Eq.1}$$

The required weight values come from the software training. The memristive cells are programmed by applying pulses, which can be changed in terms of amplitude, pulse width and number of pulses [7]. The starting point is that the weights are set via "probabilities". The MDs can only become the logical values "0" and "1" and their state changes with a certain "probability" depending on the pulses applied. Accordingly, their conductivity follows a bimodal distribution. For each applied pulse, the state of the memristive cell can be represented via a bimodal distribution (how many devices are statistically in the HRS and in the LRS) [8]. In [9] it is shown that the statistical variation resulting from a superposition of many bimodal distribution functions can be represented by the superposition of Gaussian distribution functions. This allows the replacement of the bimodal distributions with Gaussian distributions for the usage of NOVA to simulate the fluctuations of the MDs as in [5]. The simulations are carried out with the Spectre simulator Cadence Virtuoso. After the simulation, the winner is determined according to the winner-takes-all principle as in [10].

III. Interpretation of the Weight Definition from Pulse Programming

A pulse with a pulse width of 1 µs and an amplitude of 0.8V is defined for programming the devices. This pulse is sent 100 times to 128 different cells that are in the HRS before the first pulse. A MD can therefore be in the HRS state or in one of the 100 programming states depending on the number of applied pulses (measurement data from [7]). To be able to use NOVA, an average value and a standard deviation are calculated for each programming state using the 128 measured curves. According to Eq. 1, two MDs are required for a weight W, whereby a weight W can be composed according to figure 1 (a).

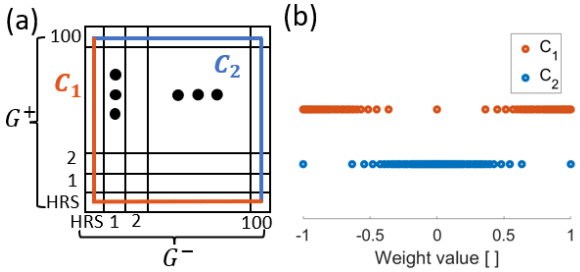

Figure 1 (a) Representation of the 10,201 possible weights within the -1 to +1 range in the 101x101 matrix via paths. (b) Possible discrete weight values within the -1 to +1 range depending on the selected path.

Paths (e.g. C_1 and C_2) can be formed within this matrix, which must be set for the range from -1 to +1 for G^+ and G^-. However, it is noticeable that the values of G^+/G^- do not increase continuously from HRS to the 100th pulse, which means that the values from -1 to +1 can also be set with different accuracy. This is illustrated in figure 1 (b). Here the path C_1 covers weight values in the range from -1 to -0.5 and +0.5 to +1 with high accuracy, whereby C_2 provides a higher resolution in the range from -0.5 to +0.5.

Figure 2 shows the standard deviation of each possible weight W. Here it can be seen that path C_1 has lowest standard deviations and C_2 has the highest standard deviations.

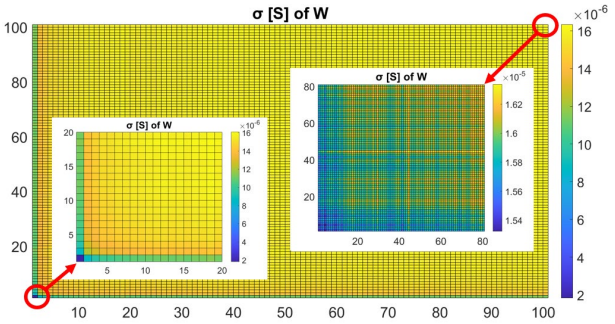

Figure **2** Visualization of the resulting standard deviation for each possible weight to be set.

IV. Simulation Results of the Memristive Crossbar Array

The memristive crossbar array is tested with the same images of a "7" and a "4" as from [5] (programming of weights by conductance level), as well as the image of a "1". For all cases, the weights are trained with a resolution of 0.1 weight stepping. The paths C_1 and C_2 are compared by adjusting the target weight to the closest possible value (see figure 1(b)). The results are shown in Table 1, as percentage of classifying the given number as a winner.

Table 1 Classification results of the images of a "7", "4" and "1" with path C_1 and C_2. The expected result is marked in green and the result with the highest probability is marked in blue.

Results	"7", C1	"4", C1	"1", C1	"7", C2	"4", C2	"1", C2
0	4.65%	23.94%	2.81%	7.73%	9.36%	4.45%
1	1.35%	6.94%	76.74%	6.28%	8.64%	15.48%
2	0.44%	0.36%	0.08%	11.17%	10.79%	9.13%
3	2.57%	1.10%	4.34%	12.11%	7.67%	11.00%
4	1.13%	8.52%	4.60%	8.14%	11.69%	8.57%
5	0.24%	0.88%	0.21%	9.73%	9.62%	9.39%
6	0.84%	16.15%	4.35%	6.00%	10.30%	10.60%
7	87.84%	32.58%	6.23%	20.68%	11.20%	12.00%
8	0.92%	9.39%	0.34%	9.74%	12.30%	10.26%
9	0.02%	0.14%	0.30%	8.42%	8.43%	9.12%

Table 1 shows that path C_2 delivers significantly worse classification results than path C_1. The reason for this is that the variability in the weights is very large for path C_2, which means that no precise classification is possible. The three digits are all classified with a similar probability. In contrast, in path C_1 the "7" is classified correctly with 87.84% (in [5] in the worst case 99.4% and best case 100%) and the "1" with 76.74%. The "4" is misclassified in most cases and is most frequently identified as a 7. In [5], this "4" is correctly classified in the best case with 50.44%.

Two factors play a role in the result of the programming: 1) The possible fluctuation of the desired weight value and 2) the number of adjustable weights or the accuracy of how finely resolved they should be set.

Path C_1 was selected for testing the "1" image, with weights set to increments of 0.1, 0.05 and 0.025 and noise levels of 100% (referred to the statistical variations as observed in the measurements), 85%, 67%, 25% and 0%. The results are shown in figure 3.

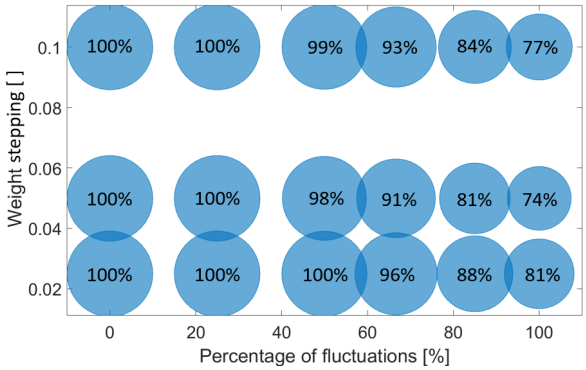

Figure **3** Illustration of the effect of different increments of the weights and a reduction in the variability of the weights. The percentage for the correct classification of "1" is given.

Figure 3 shows that the classification with a step of 0.025 is better than with 0.1, but the result only improves slightly. However, the 0.05 step is worse than with 0.1, as the finer discretization leads to weight combinations with an increased σ. It is noticeable that a reduction of the variability provides significantly better classification results. Even with a reduction of 1/3, the results are in the 90% range for all step sizes.

V. Conclusion

The programming via pulses shows strong variability in the weight values. As a result, the classification accuracy of the MNIST dataset is influenced by the variability depending on the G^+/G^- settings. In addition, regarding a high probability for a correct classification, it is more important that the weights fluctuate less than whether they can be set precisely. A reduction of the fluctuations observed in measurements by 33% already shows significant improvements. However, even without fluctuations a precise setting of conductance states is important to achieve the correct classification results.

References

[1] C. Zambelli et al., International Memory Workshop, pp. 1-4, 2014.
[2] P. Huang et al., IEEE Trans. Electron Devices, vol. 64, no. 2, 2017.
[3] Z. Jiang et al., IEEE TED., vol. 63, no. 5, pp. 1884–1892, 2016.
[4] A. Kloes et al., Solid-State Electronics, vol. 201, p. 108606, 2022.
[5] N. Dersch et al., Solid-State Electronics, vol. 209, p. 108760, 2023.
[6] C. Zambelli et al., ICMTS, pp. 27-31, 2014.
[7] E. Perez et al., JJAP, vol. 61, no. SM, 2022.
[8] C. Wenger et al., IEEE EDL, vol. 40, no 4, 2019.
[9] N. Dersch et al., IEEE LAEDC, pp. 1-4, 2024.
[10] N. Bogun et al., MIXDES, pp. 83-88, 2022

Modeling and Control of a Three-Phase Interleaved Buck Converter as a Battery Charger

El Nouha Mammeri, Oswaldo Lopez-Santos, Abdelali El Aroudi, and Luis Martinez-Salamero
elnouha.mammeri@urv.cat, oswaldo.lopez@urv.cat, abdelali.elaroudi@urv.cat, luis.martinez@urv.cat

Abstract

This paper presents the dynamic modeling of a three-phase interleaved buck converter, and the design of a multiple loop controller in cascade configuration, to implement the constant-current constant-voltage (CC-CV) protocol for the ultrafast charging of an electric vehicle (EV) battery of 100 V from a 380V DC input. The designed controller is validated by PSIM simulations and is tested to put in evidence its robust performance in terms of input and load variations, and uncertainties in the converter parameters. Afterward, a scaled down prototype is implemented in the laboratory to validate experimental work.

1. Introduction

The transport system's electrification is crucial for a clean energy network and reducing carbon emissions. Ultrafast charging infrastructures are needed to spread transport electrification and electric vehicles (EVs) worldwide. In that sense, a charging time of less than 10 minutes and power levels around 350 kW are acceptable in Ultrafast charging. Moreover, non-isolated converter can be used as the interface between the DC bus and EV battery. In addition, considering the high-power levels that needs to be handled, the interleaved buck converter can be used to distribute the output current between the phases and reduce the peak-to-peak output ripple

2. System Description

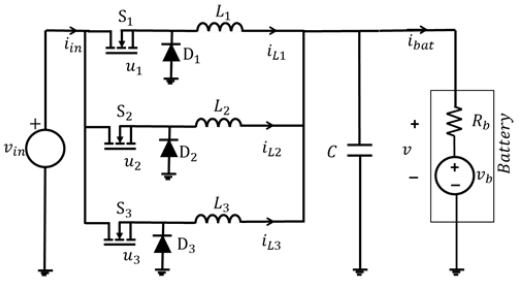

Fig.1. Parallel connection of three buck converters sharing the same input source and output network.

The proposed circuit is presented in Figure 1. It consists of three buck converters connected in parallel, sharing the same DC input voltage v_{in} and the output connection to a battery. Moreover, in order to enforce symmetric interleaving operation, a phase-shift of 120° is introduced between the gate signals of the controlled switches which are obtained using pulse-width-modulation (PWM).

3. Converter Modeling

In order to simplify the analytical development, three assumptions are considered. First, the passive components and semiconductors of the circuit are all considered ideal. The second assumption is related to the inductances of the circuit, where an identical value is assumed for the three phases ($L_1 = L_2 = L_3 = L$). Finally, the battery load is modeled as a constant voltage source V_b in series with a resistor R_b.

The average model is obtained by considering equal inductances and replacing in (1) the control variables u_1, u_2 and u_3 by their average value representing the duty cycle d.

$$\frac{di_L}{dt} = \frac{v_{in}}{L}d - \frac{v}{L} \qquad (2)$$

$$\frac{dv}{dt} = \frac{3i_L}{C} - \frac{v}{R_bC} + \frac{v_b}{R_bC} \qquad (3)$$

By introducing perturbation in the variables in equations (2) and (3), linearizing and applying the Laplace transform, the small signal model of the system is given by equations (4) and (5).

$$\tilde{V}(s) = \tilde{d}(s)\frac{V_{in}\frac{3}{LC}}{d_n} + \tilde{V}_{in}(s)\frac{D\frac{3}{LC}}{d_n} + \tilde{V}_b(s)\frac{\frac{1}{R_bC}s}{d_n} \qquad (4)$$

$$\tilde{I}_L(s) = \tilde{d}(s)\frac{\frac{V_{in}}{L}(s+\frac{1}{R_bC})}{d_n} + \tilde{V}_{in}(s)\frac{\frac{D}{L}(s+\frac{1}{R_bC})}{d_n} - \tilde{V}_b(s)\frac{\frac{1}{LR_bC}}{d_n} \qquad (5)$$

where $d_n = s^2 + \frac{1}{R_bC}s + \frac{3}{LC}$

In order to synthesize the controller, it is necessary to obtain the transfer functions related to the three-phase interleaved buck converter. To do that, we consider null dynamics for $\tilde{V}_{in}(s)$ and $\tilde{V}_b(s)$ in equations (4) and (5), obtaining the transfer function from control to output voltage $G_{dv}(s) = \tilde{V}(s)/\tilde{d}(s)$, and the transfer function from control to inductor current $G_{di}(s) = \tilde{I}_L(s)/\tilde{d}(s)$.

$$G_{dv}(s) = \frac{\tilde{V}(s)}{\tilde{d}(s)} = \frac{\frac{3V_{in}}{LC}}{s^2+\frac{1}{R_bC}s+\frac{3}{LC}} \qquad (6)$$

$$G_{di}(s) = \frac{\tilde{I}_L(s)}{\tilde{d}(s)} = \frac{\frac{V_{in}}{L}\left(s+\frac{1}{R_bC}\right)}{s^2+\frac{1}{R_bC}s+\frac{3}{LC}} \qquad (7)$$

4. Controller Design

The control scheme for the battery charger based on the three-phase interleaved buck converter is presented in Figure 2.

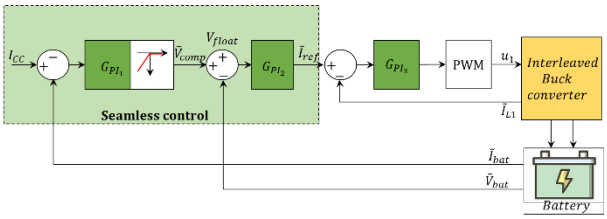

Fig.2. Complete control scheme for the battery charger.

The control strategy consists of three loops in cascade configuration, where each loop has its dedicated proportional integral (PI) controller. The controller of the inner loop is dedicated to regulate the inductor current and generates the duty cycle. As we are assuming equal inductances and no parasitic resistances, the three phases are identical. As a consequence, the inductor current of each phase is regulated by an identical PI controller $G_{PI_3}(s)$. The following control loop contains the secondary controller with transfer function $G_{PI_2}(s)$. This loop regulates the battery voltage and has as reference, the summation of the desired CV voltage V_{float} and the contribution of the outer loop V_{com} as illustrated in Fig. 2. Moreover, this loop provides the reference $\tilde{I}_{ref}(s)$ to the inner loops, establishing democratic current sharing. The most outer loop regulates the battery current at the reference I_{CC} during the CC phase, by means of the PI controller $G_{PI_1}(s)$. This loop imposes initially the CC mode and is deactivated when the output voltage reaches the desired constant voltage. This is achieved because the output of the outer loop is saturated at zero, which means that the negative value of V_{com} reduces the battery voltage during the CC phase.

In another hand, the three PI controllers are designed using the root locus method. The specifications for design of control parameters, namely, proportional controller gain K_p, integral gain K_i and integral time τ_i, are maximum overshoot and maximum settling time.

5. Simulation Results

The battery charger based on the interleaved buck converter depicted in Fig. 2 has been simulated by means of PSIM for the system parameters of table 1.

Table 1. System parameters

PARAMETER	VALUE	UNITIES
Input Voltage	380	V
Switching Frequency	100	kHz
Inductance	27	µH
Output Capacitance	30	µF
Battery Voltage Range	80-125	V
Battery Charging Current	300	A
Battery Resistance	33	mΩ
Battery Capacity	75	Ah

Fig. 3 presents the steady state waveforms of inductor current in each of the three phases of the interleaved buck converter. It can be seen that the current is equally distributed between the three phases.

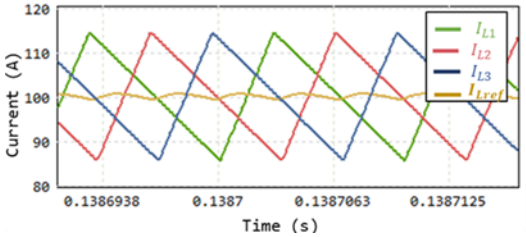

Fig.3. Inductor currents waveforms in steady state.

In order to verify the performance of the designed controller in terms of CC-CV charging protocol, a PSIM simulation of the same system is performed, using the model of battery illustrated in Fig. 4, where the open–circuit voltage Voc is constantly updated according to a lookup table (LUT) according to the state of charge (SoC) of the battery.

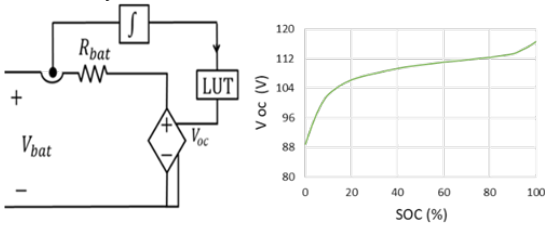

Fig. 4.Lithium-ion battery model. a) circuit model. b) open-circuit voltage dependence on the battery SoC.

Fig. 5 shows both battery current and battery voltage during CC and CV modes. It can be seen that in the constant current phase CC, the battery current remains constant at a desired value I_{CC}=300 A. When the battery voltage reaches the desired reference of $V_{float} = 116$ V, the current start decreasing exponentially and the constant voltage phase begins.

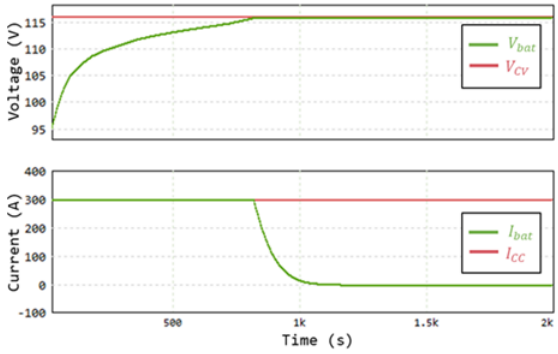

Fig.5. Battery current and battery voltage during a complete CC-CV charging cycle.

7. Conclusions

The modeling and control of a three-phase interleaved buck converter as a battery charger has been analyzed in this paper. The dynamic model has been studied and the transfer functions required to synthesize the controller have been obtained. A three-loop cascade controller has been designed where the most inner loop is dedicated to the democratic sharing of inductor current for equal distribution between the three phases, while the two outer loops constitute a seamless controller in which a CC-CV charging protocol has been implemented. Simulation

results have shown that the designed controllers can maintain a desired response with good stability, fast dynamic response and robustness.

Exploring multi-omics interactions: microbiota, metabolites, and host responses in a lifestyle intervention model

Jordi Rofes[1], Joan Miró[1,2], Christian Heyer[3], Pau Gama4, Pablo Miguel Garcia-Rovés[4], Matthias Schlesner[3], Óscar Yanes[1,2]

1. Universitat Rovira i Virgili, Department of Electronic Engineering, IISPV, Tarragona, Spain 2. CIBER de Diabetes y Enfermedades Metabólicas Asociadas (CIBERDEM), Instituto de Salud Carlos III, Madrid, Spain. 3. University of Augsburg, Faculty of Applied Computer Sciences, Biomedical Informatics, Data Mining and Data Analytics, Augsburg, Germany. 4. Department of Physiological Sciences, School of Medicine and Health Sciences, University of Barcelona, and Bellvitge Biomedical Research Institute (IDIBELL), L'Hospitalet del Llobregat, Barcelona, Spain

Abstract

The microbiota has gained an increased interest in recent years. Studies have linked the microbiota with disease, but mechanisms are still unknown. Microbiota metabolites could change interact with the host through epigenetics mechanisms and changes in diet could alter the microbiota composition and their interactions with the host. To study these interactions a lifestyle intervention C57BL/6J mice model was generated with three groups (each n = 10): fed a standard diet, an ad-libitum high fat diet, and a high fat diet followed by a lifestyle intervention. We acquired liver gene expression (RNA-Sequencing), epigenetics (Whole genome bisulphite sequencing and histone proteomics, WGB-Seq) and metabolites (targeted epigenetically relevant and untargeted); cecum and colon microbiome data (16S sequencing, shotgun sequencing and functional data), metabolites (targeted) and metals; and serum metabolites. Results were integrated in a multi-omics factor analysis and the trends were summarized by two factors: the first represented features that were restored by the lifestyle intervention and the second represented features that were still altered. Enrichment of factor 1 showed immune system and sugar metabolic pathways; factor 2 fatty acid, short chain fatty acid (SCFA) and aminoacid metabolism; and carbon metabolism in both.

1. Introduction

The microbiota plays a vital role in the organism by aiding the development of the immune system, producing key metabolites, such as vitamins and amino acids and maintaining gut structure[1]. Alterations of the microbiota have been associated with obesity[2] and its restoration has been effective in restoring the phenotype[3,] but the mechanisms remain unclear. The microbiota produces metabolites that can change the epigenome such as short chain fatty acids (SCFA), vitamins, and folate[4,5] and we hypothesized that these metabolites affect gene expression from the host and that changes in the diet and lifestyle can alter these interactions.

To study this, we applied a multi-omic approach to a lifestyle intervention C57BL/6J mice model with three groups (each n = 10): fed a standard diet (CNT), a high fat diet (HFD), and a high fat diet followed by a lifestyle intervention with a healthier diet and exercise (INT) (Figure 1). Then, we acquired liver gene expression (RNA-Seq), epigenetics (sequencing and histones) and metabolites (targeted and untargeted); cecum and colon microbiome data (16S sequencing and shotgun sequencing), targeted metabolites and metals; and serum metabolites.

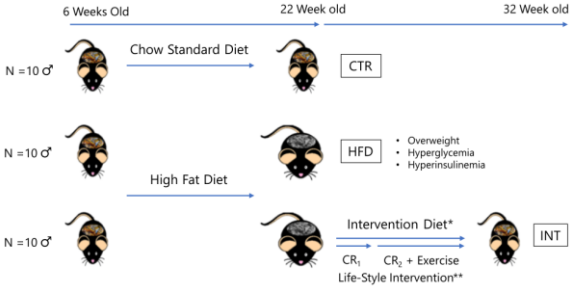

Figure 1. Life-style intervention model overview. From top to bottom: CTR group fed standard diet, HFD group a high fat diet and INT group a high fat diet and a following life-style intervention changes.

*Flaxseed and olive oil instead of lard and soybean oil; corn starch instead of sucrose

**CR1 80% of caloric intake from CTR mice. CR2 100% of caloric intake from CTR mice. Exercise 1h/day, 5days/week.

2. Methods

Each omic layer was processed and analyzed independently, statistically tested, and filtered to keep variables statistically significant in at least one

comparison. A multi-omics factor analysis (MOFA2) model was trained with 2 factors, a percentage of belonging was calculated as the weight of a variable in a factor divided by the sum of the weights in all the factors and a threshold of >0.8 was selected. Spearman cross-correlations were calculated for each factor selected features, tested for statistical significance; and filtered by p<0.05 after FDR and >0.8 correlation strength in absolute value. A KEGG partial joint pathway enrichment analysis was performed of the RNA-Sequencing genes, genes closer to the differentially methylated regions and mummichog-annotated untargeted metabolomics features.

3. Results

The MOFA factors capture two main trends of the HFD alterations (Figure 2.A):

1) Alterations that are restored with the intervention
2) Alterations that are resistant to the intervention

Factor 1 explains the variability from the epigenetic layers and liver metallomics, while factor 2 the cecum metallomics and is evenly distributed between all the other omics represented in the factor (Figure 2.B).

Correlation analysis of the variables that belong to each factor shows an increase percentage of correlations with the epigenetic layers in factor 1 and an increased correlation with the microbiota and their functionalities in factor 2, specifically stronger in the colon compared to the cecum (Figure 3). KEGG pathway enrichment of the correlated features shows pathways related to sugar hormones such as insulin and glucagon in factor 1; and fatty acid metabolism and degradation, peroxisome, aminoacid degradation and short chain fatty acids related propanoate and butanoate metabolisms in factor 2 (Figure 4)

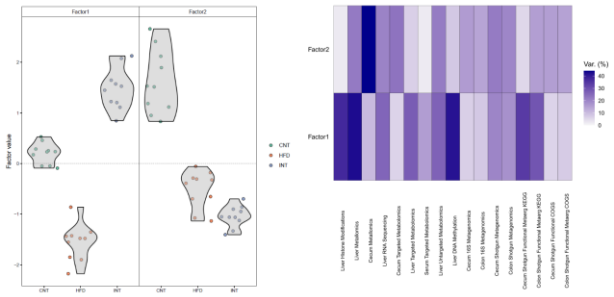

Figure 2. A.Violin plot of the two first factors from the multi omics factor analysis (MOFA) model. B. Percentage of explained variance of each omic layer on the two first MOFA factors.

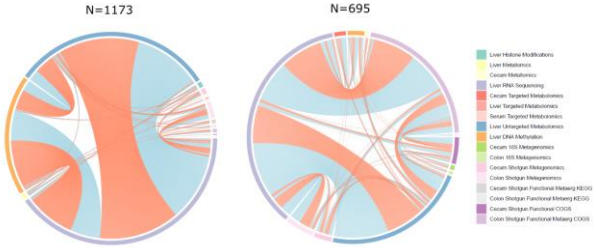

Figure 3. Circos plot of the features with significant Spearman correlations >0.8 in absolute value between features with highest belonging in each factor. Left, factor 1 (N = 1173 features) and right, factor 2 (N = 695). Link color represents the positive (red) and negative (blue) correlations.

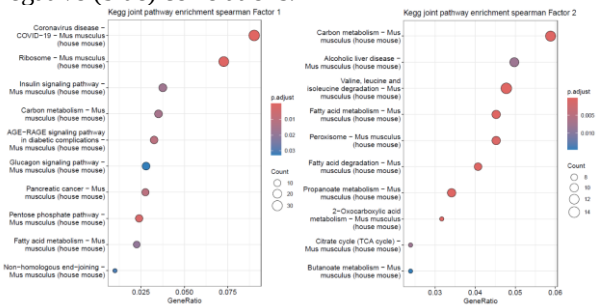

Figure 4. Top 10 enriched KEGG pathways from the partial enrichment analysis of genes, metabolites, and genes closer to the differentially methylated regions (DMRs) for factor 1 (left) and factor 2 (right).

4. Conclusions

The results show that the life-style intervention can restore 22.5% of liver epigenetic, expression and metabolic changes caused by the high fat diet. However, 12.5% of features remain altered and they strongly correlate with the cecum and colon microbiota and their functionalities, indicating a possible relationship that is not driven by the DNA methylation.

KEGG enrichment of factor 2 indicates that changes that remain altered are related to the SCFA metabolism and could be associated to microbiota composition and fatty acid metabolism, while factor 1 indicates that hormonal changes and sugar metabolism are restored or even over-compensated with the intervention.

References

1. Adak, A. & Khan, M. R. An insight into gut microbiota and its functionalities. Cellular and Molecular Life Sciences 76, 473–493 (2019).
2. Bäckhed, F. et al. The gut microbiota as an environmental factor that regulates fat storage. Proc Natl Acad Sci U S A 101, 15718–15723 (2004).
3. Ridaura, V. K. et al. Cultured gut microbiota from twins discordant for obesity modulate adiposity and metabolic phenotypes in mice. Science (1979) 341, 1–22 (2014).
4. Sun, D., Chen, Y. & Fang, J. Y. Influence of the microbiota on epigenetics in colorectal cancer. Natl Sci Rev 6, 1138–1148 (2019).
5. Greenblum, S., Turnbaugh, P. J. & Borenstein, E. Metagenomic systems biology of the human gut microbiome reveals topological shifts associated with obesity and inflammatory bowel disease. Proc Natl Acad Sci U S A 109, 594–599 (2012).

Spectral Annotation Robustness in Metabolomics: Addressing Variations in Acquisition Conditions

J.M. Badia[1,2,3], J. Capellades[1,2], R. Giné[1], O. Yanes[1,2], M. Vinaixa[1,2]

1. Universitat Rovira i Virgili, Department of Electronic Engineering & IISPV, Tarragona, Spain.
2. CIBER de Diabetes y Enfermedades Metabólicas Asociadas (CIBERDEM), Instituto de Salud Carlos III, Madrid.
[3] Email: josepmaria.badia@urv.cat

Abstract

Tandem mass spectrometry (MS/MS) is pivotal in metabolomics for identifying and quantifying metabolites, relying on spectral annotation to match acquired spectra against databases. This study evaluates the impact of acquisition condition mismatches on annotation reliability, a significant challenge due to the acquisition conditions variability inherent to spectral libraries. We explored three annotation methods — conventional, hybrid, and merged — across different datasets.

Our analysis shows that conventional annotation, which compares single collision energy (CE) spectra, consistently underperforms due to its sensitivity to CE discrepancies, resulting in high false discovery rates. The merged method using the Tversky metric with high-energy collisional dissociation (HCD) spectra proved most effective, achieving 87% of true positives at a 13% false discovery rate under matched conditions. However, under mismatched conditions, the hybrid method was superior, adapting more effectively to variations in acquisition conditions.

This research underscores the critical role of matching acquisition conditions in spectral annotation and highlights the merged and hybrid methods as robust strategies for improving annotation accuracy.

1. Introduction

Tandem mass spectrometry (MS/MS) is widely used in metabolomics to identify metabolites. Nowadays, automation of the different MS/MS spectra acquisition modes requires the development of high-throughput analytical strategies to process the vast amount of data generated by MS/MS experiments. The first step to convert raw spectral MS/MS data to identified metabolites is the so-called spectral annotation consisting of the numeric comparison between empirical MS/MS spectra and tabulated spectral data in libraries together with the computation of similarity metrics. This spectral comparison is critically impacted by mismatch between the acquisition conditions of acquired spectra and those established on the spectral databases, often vendor libraries such as Nist 2020 [1]. The use of open-source libraries, such as MonaEU [2], can magnify even more the variability of acquisition workflows, instrumentation and settings, resulting in a low reliable and heterogeneus spectral library.

The collision energy (CE) used for spectral fragmentation plays a crucial role in determining the fragmentation patterns observed in MS/MS spectra. Different collision energies in CID dissociation of the same precursor ion produce spectra with different precursor / product intensity ratios and fragment heterogeneity [3], resulting in poor metric scores. A standard practice in MS/MS data acquisition is the use of stepped collision energy spectra, where the precursor ion is fragmented at multiple collision energies and compared to conventional databases of single CE spectra. This approach, referred in the present paper as hybrid annotation, poses a challenge for accurate annotation of stepped spectra.

This study introduces a novel annotation method and evaluates different annotation methods to assess their performance when the acquisition conditions of acquired spectra differ from those used to build the spectral database.

2. Methods

This study employed three distinct MS/MS datasets, all acquired in positive ionization mode using electrospray ionization and M+H adducts.

HCDNist: Dataset from the NIST Tandem Mass Spectral Library. It contains 266,347 high-energy collisional dissociation (HCD) spectra acquired from 22,123 unique compounds using Orbitrap instruments.

CIDNist: Nist dataset of 24,586 collision-induced dissociation (CID) spectra from 2,430 compounds. The spectra were acquired using an Agilent QTOF 6530 instrument.

CIDMetlin: Dataset from the Metlin Tandem Mass Spectral Library with 48,634 CID spectra acquired using a Bruker Impact II Q-TOF mass spectrometer from 12,159 unique compounds.

We evaluated three annotation methods:

Conventional: This approach directly compares each single CE query spectrum to all reference spectra in the database.

Hybrid: This method first merges collision energy representative spectra from each precursor ion to generate a merged query spectrum. This merged query spectrum is then compared to single CE reference spectra from the database.

Merged: This method compares merged query spectra (generated as in the hybrid method) to merged reference spectra. These merged reference spectra are dynamically generated for each comparison, using the minimum number of spectra from the database required to represent all fragments in the query spectrum.

We employed three different metrics to assess the similarity between spectra:

Cosine Similarity: This metric calculates the cosine of the angle between the two spectra considering the intensities of their fragment ions.

Binary Cosine: It computes the cosine similarity on a binarized basis by categorizing fragment ion intensities as either 0 (absent) or 1 (present).

Tversky95: Asymmetric binary metric that assigns a greater penalty to the non-common fragments present in the query spectrum ($\alpha = 0.95$, $\beta = 1$).

3. Results

This study examines the impact of three different annotation methods when spectra is acquired under different conditions. Conventional annotation method offered poor results across all all studied scenarios. ROC and true positive / false discovery rate (TPR/FDR) curves (Figures 1 to 6, C_cosine and C_cosineBin) show high FDR and poor general performance (Area Under the Curve or AUC). Only for a limited number of positive annotations and similar CE (Figure 2, C_cosine, TPR < 0.05) the comparison of fragments intensities using the cosine metric resulted in a strongly reduction of the FDR. Finally, figure 1 and 2 also reveals high dependency of the method on the CE similarity between the spectra being compared: CE differences between query and reference exceeding 10 units (C10_cosine, C10_cosineBin) severely degraded the conventional annotation performance.

The merged annotation with the Tversky metric was found to be the most reliable method, specifically when we annotate HCD spectra (Figures 1 and 2). E.g. a 0.9 threshold captured a 87% of the positive annotations at 13% FDR. Conversely, when scenarios where the acquisition conditions of the spectra differed, the hybrid approach was the method that delivered the most optimal annotations (Figures 3 to the last).

4. Conclusions

The similarity between acquisition conditions plays a crucial role in the quality of the annotations and greatly determines the optimal annotation method. When HCD spectra from NIST database are annotated with each other, the merged approach with the Tversky metric is the method showed most realiable. The high similarity between spectra of the same compound results in fewer reference spectra being merged and consequently a limited number of non-common fragments in the query spectrum. This reduces their penalty weight of the highly asymmetric Tversky metric, and thus results in a significant increase in the score when spectra of the same compound are compared.

On the other hand, when spectra acquired under mismatched conditions are compared, differences between spectra of the same compound become more pronounced. This diminishes the efficiency of the merge method to the extent that the hybrid approach becomes the most effective annotation option.

Finally, the conventional annotation method, where spectra are compared directly without merging, consistently shows poor performance across all scenarios. Additionally, since only single CE fragmentation profiles are compared, its effectiveness heavily relies on the similarity between the CE values of the compared spectra.

References

[1] NIST Mass Spectrometry Data Center, National Institute of Standards and Technology, 2020. Tandem Mass Spectral Library. Available online: https://chemdata.nist.gov/.

[2] Horai, H., Arita, M., Kanaya, S., Nihei, Y., Ikeda, T., Suwa, K., Ojima, Y., Tanaka, K., Tanaka, S., Aoshima, K., Oda, Y., Kakazu, Y., Kusano, M., Tohge, T., Matsuda, F., Sawada, Y., Hirai, M. Y., Nakanishi, H., Ikeda, K., . . . Nishioka, T. (2010). MassBank: a public repository for sharing mass spectral data for life sciences. Journal of Mass Spectrometry, 45(7), 703–714. https://doi.org/10.1002/jms.1777

[3] Vékey, K. (1996). Internal energy effects in mass spectrometry. *Journal of Mass Spectrometry*, *31*(5), 445–463. https://doi.org/10.1002/(sici)1096-9888(199605)31:5

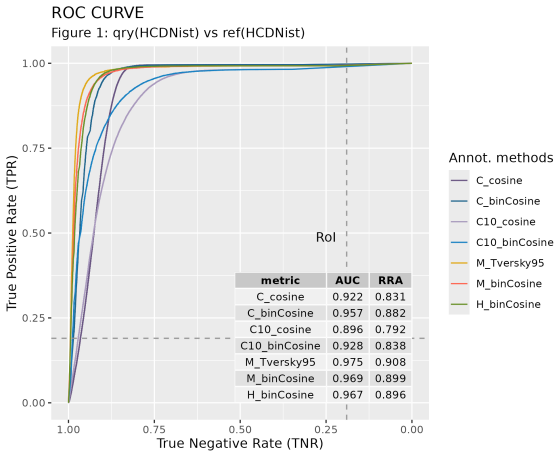

Fig.1. ROC curves for cases where both the query and reference were HCD NIST spectra.

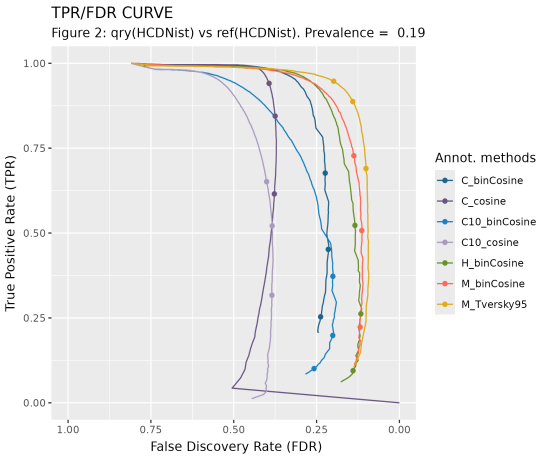

Fig.2. TPR/FDR curves when both the query and reference were HCD NIST spectra.

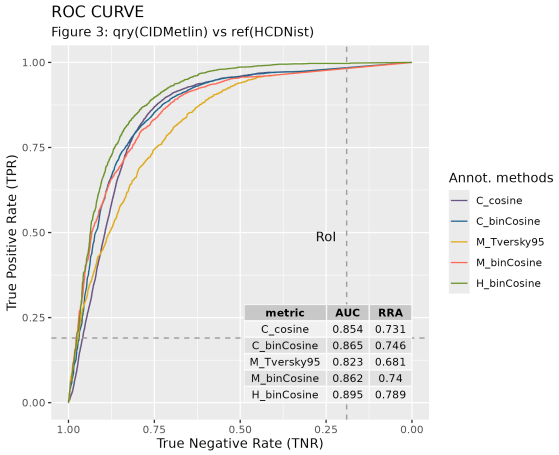

Fig.3. ROC curves when CID Metlin query spectra were annotated against the HCD NIST spectral library.

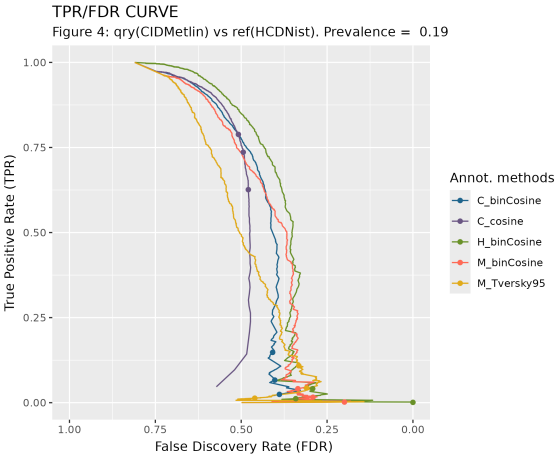

Fig.4. TPR/FDR curves when CID Metlin query spectra were annotated against the HCD NIST spectral library.

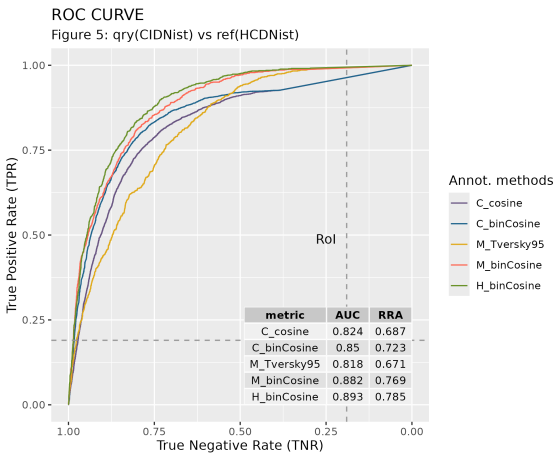

Fig.5. ROC curves when CID NIST query spectra were annotated against the HCD NIST spectral library.

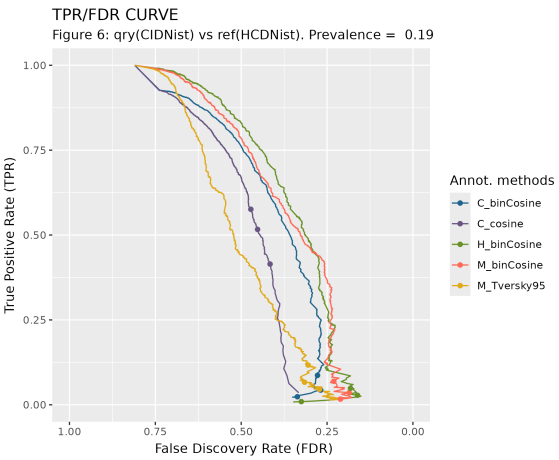

Fig.6. TPR/FDR curves when CID NIST query spectra were annotated against the HCD NIST spectral library.